

electronics COOLING

FEATURED IN THIS EDITION

16 THE FUTURE OF DATA CENTER COOLING: PASSIVE TWO-PHASE COOLING

22 DESIGN CONSIDERATIONS WHEN USING HEAT PIPES

28 HEADSET COMFORT ASSESSMENT THROUGH THERMAL ANALYSIS AND IR IMAGING

34 RESEARCH SPOTLIGHT: INCREASED SYSTEM PERFORMANCE IN MOBILE ELECTRONICS USING HIGH PERFORMANCE INSULATION-GRAPHITE COMPOSITES

4 **CALCULATION CORNER**
APPLICATION OF TRANSIENT THERMAL METHODS TO MOISTURE DIFFUSION CALCULATIONS, PART 2

10 **STATISTICS CORNER**
NORMAL DISTRIBUTION

12 **TECH BRIEF**
EFFECTIVE HEAT SPREADING ANGLE

42 **ADVERTORIAL:**
DUOCEL® METAL FOAM HEAT EXCHANGERS

Alpha's Online Heat Sink Customization

Quickly and Easily Create a Custom Heat Sink

ALPHA | Your partner for thermal solutions
CUSTOM HEAT SINK BASED ON LPD45

1. Specify customization 2. Review customization 3. Input contact information 4. Submit Request

Customization Menu: Change Height, Change Base, Add Through Hole, Add Tapped Hole, Add Flange Pin and Hole, Add TIM, Change Surface Finish, Add Paste

Reference drawing: Length(L) 45.00, Width(W) 45.00, 12.00, 3.00

Note: Legend: Hole Tap Removal Area Pin Area C-bore Fin Product

| Quantity | | Unit price (US\$) |
|----------|--------|-------------------|
| 1 | 122.73 | |
| 5 | 29.29 | |
| 10 | 10.01 | |
| 50 | 5.56 | |
| 100 | 4.31 | |
| 200 | RFO | |

Complete Input

| Add Hole [Edit/Delete] | | | | | | | | | |
|------------------------|----------|------------------------|---------------------|----------------------|--------|-----------------------|-------|-----------------|-------|
| ID | Diameter | Effective Length/ THRU | Fin Removal Area | Location from Center | | C-bore Component side | | C-bore Fin side | |
| | | | | X-axis | Y-axis | Diameter | Depth | Diameter | Depth |
| 1 | 4.5 | Through | Minimum fin removal | 15 | 15 | - | - | - | - |
| 2 | 4.5 | Through | Minimum fin removal | -15 | -15 | - | - | - | - |
| 3 | 4.5 | Through | Minimum fin removal | -15 | -15 | - | - | - | - |
| 4 | 4.5 | Through | Minimum fin removal | 15 | 15 | - | - | - | - |

ALPHA | Your partner for thermal solutions
CUSTOM HEAT SINK BASED ON N13070

1. Specify customization 2. Review customization 3. Input contact information 4. Submit Request

Customization Menu: Change Height, Change Base, Add Through Hole, Add Tapped Hole, Add Flange Pin and Hole, Add TIM, Change Surface Finish, Add Paste

Reference drawing: Width(W) 115.00, Length(L) 67.00, 24.00, 6.00

Note: Legend: Hole Tap Removal Area Pin Area C-bore Fin Product

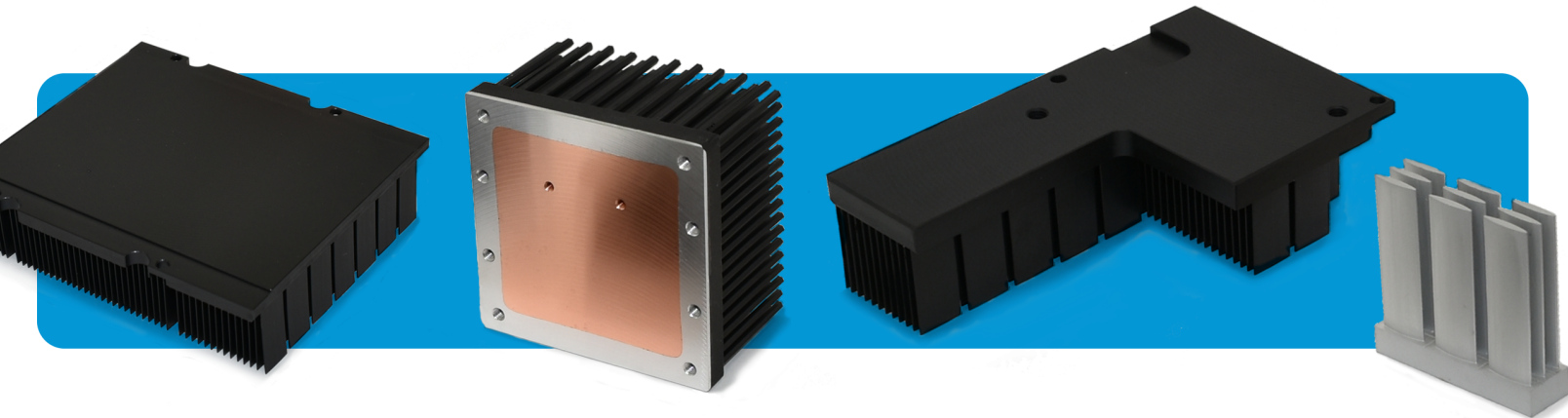
| Quantity | | Unit price (US\$) |
|----------|--------|-------------------|
| 1 | 162.35 | |
| 5 | 43.56 | |
| 10 | 28.71 | |
| 50 | 14.60 | |
| 100 | 13.70 | |
| 200 | RFO | |

Complete Input

| Change Base Size [Edit/Delete] | | | | | | | | | |
|--------------------------------|--|--|--|--|--|--|--|--|--|
| Base Width | | Base Length | | | | | | | |
| 115 | | The cut section interferes with fins. Suggested size 65.3mm or 68.8 mm | | | | | | | |

| Add Hole [Edit/Delete] | | | | | | | | | |
|------------------------|----------|------------------------|------------------|----------------------|--------|-----------------------|-------|-----------------|-------|
| ID | Diameter | Effective Length/ THRU | Fin Removal Area | Location from Center | | C-bore Component side | | C-bore Fin side | |
| | | | | X-axis | Y-axis | Diameter | Depth | Diameter | Depth |
| 1 | 6 | Through | 8 | 15 | 15 | 8.00 | 2.0 | - | - |
| 2 | 6 | Through | 8 | -15 | -15 | 8.00 | 2.0 | - | - |

Add Tapped Hole



Proto lead time
1-2 weeks

Typical production lead time is 2-3 weeks.

No NRE fee

In most cases, a tooling fee will not be required.

No MOQ, No Min. order value

Alpha can supply from a single piece to production volumes.

Quick and Easy

A custom heat sink can be designed in minutes.

ALPHA Co., Ltd.
 Head Office
www.micforg.co.jp

256-1 Ueda, Numazu City, Japan 410-0316
 Tel: +81-55-966-0789 Fax: +81-55-966-9192
 Email: alpha@micforg.co.jp

ALPHA NOVATECH, INC.
 USA Subsidiary
www.alphanovatech.com

473 Sapena Ct. #12, Santa Clara, CA 95054 USA
 Tel: +1-408-567-8082 Fax: +1-408-567-8053
 Email: sales@alphanovatech.com

October 20 – 21 2020

thermalLIVE 2020

ONLINE EVENT

The Largest Single Thermal Management Event of The Year - Anywhere.

Thermal Live™ is a new concept in education and networking in thermal management - a FREE 2-day online event for electronics and mechanical engineers to learn the latest in thermal management techniques and topics. Produced by *Electronics Cooling*® magazine, and launched in October 2015 for the first time, Thermal Live™ features webinars, roundtables, whitepapers, and videos... and there is no cost to attend.

For more information about Technical Programs,
Thermal Management Resources, Sponsors & Presenters

please visit:

thermal.live

thermalLIVE
2020

Presented by

electronics
COOLING

Call for Authors and Contributors!

Want to be a part of the next issue of Electronics Cooling? Have an article or blog post you'd like to write for Electronics-Cooling.com?

Let us know at
editor@electronics-cooling.com

 **electronics
COOLING**

www.Electronics-Cooling.com

CONTENTS

2 EDITORIAL

Victor A. Chiriac

4 CALCULATION CORNER

Application of Transient Thermal Methods
to Moisture Diffusion Calculations, Part 2

Bruce Guenin

10 STATISTICS CORNER

Normal Distribution

Ross Wilcoxon

12 TECH BRIEF

Effective Heat Spreading Angle

Dirk Schweitzer

16 THE FUTURE OF DATA CENTER COOLING: PASSIVE TWO-PHASE COOLING

Raffaele Luca Amalfi, Filippo Cataldo, John Richard Thome

22 DESIGN CONSIDERATIONS WHEN USING HEAT PIPES

George Meyer

28 HEADSET COMFORT ASSESSMENT THROUGH THERMAL ANALYSIS AND IR IMAGING

Rachel McAfee, Matt Harrison, Joshua Gess

34 RESEARCH SPOTLIGHT

Increased System Performance in Mobile Electronics Using
High Performance Insulation-Graphite Composites

Mitchell Warren, Julian Norley, John Allen, Jonathan Taylor,
Lindsey Keen

42 ADVERTORIAL

Duocel® Metal Foam Heat Exchangers

Burhan Ozmat, Metodi Zlatinov, and Denver Schaffarick

48 2020 COMPANY PRODUCTS & SERVICES DIRECTORY

52 INDEX OF ADVERTISERS

PUBLISHED BY

Lectrix

1000 Germantown Pike, F-2

Plymouth Meeting, PA 19462 USA

Phone: +1 484-688-0300; Fax: +1 484-688-0303

info@lectrixgroup.com

www.lectrixgroup.com

CHIEF EXECUTIVE OFFICER

Graham Kilshaw | Graham@lectrixgroup.com

VP OF MARKETING

Geoffrey Forman | Geoff@lectrixgroup.com

EDITORIAL DIRECTOR

Jennifer Arroyo | Jennifer@lectrixgroup.com

CREATIVE DIRECTOR

Chris Bower | Chris@lectrixgroup.com

BUSINESS DEVELOPMENT DIRECTOR

Janet Ward | Janet@lectrixgroup.com

BUSINESS DEVELOPMENT DIRECTOR

Mark Pantalone | Mark@lectrixgroup.com

PRODUCTION COORDINATOR

Jessica Stewart | Jessica@lectrixgroup.com

LEAD GRAPHIC DESIGNER

Kristen Tully | Kristen@lectrixgroup.com

CONTENT MARKETING MANAGER

Danielle Cantor | Danielle@lectrixgroup.com

ADMINISTRATIVE MANAGER

Eileen Ambler | Eileen@lectrixgroup.com

ACCOUNTING ASSISTANT

Susan Kavetski | Susan@lectrixgroup.com

EDITORIAL BOARD

Bruce Guenin, Ph.D.

Consultant

San Diego, CA

sdengr-bguenin@usa.net

Ross Wilcoxon, Ph.D.

Associate Director

Collins Aerospace

ross.wilcoxon@collins.com

Genevieve Martin

R&D Manager, Thermal & Mechanics Competence

Signify

genevieve.martin@signify.com

Victor Chiriac, PhD, ASME Fellow

Co-founder and Managing Partner

Global Cooling Technology Group

vchiriac@gctg-llc.com

► SUBSCRIPTIONS ARE FREE

Subscribe online at

www.electronics-cooling.com

For subscription changes email

info@electronics-cooling.com

Reprints are available on a custom basis at
reasonable prices in quantities of 500 or more.
Please call +1 484-688-0300.

All rights reserved. No part of this publication may be reproduced or transmitted in any form or by any means, electronic, mechanical, photocopying, recording or otherwise, or stored in a retrieval system of any nature, without the prior written permission of the publishers (except in accordance with the Copyright Designs and Patents Act 1988).

The opinions expressed in the articles, letters and other contributions included in this publication are those of the authors and the publication of such articles, letters or other contributions does not necessarily imply that such opinions are those of the publisher. In addition, the publishers cannot accept any responsibility for any legal or other consequences which may arise directly or indirectly as a result of the use or adaptation of any of the material or information in this publication.

ElectronicsCooling is a trademark of Mentor Graphics Corporation and its use is licensed to Lectrix. Lectrix is solely responsible for all content published, linked to, or otherwise presented in conjunction with the ElectronicsCooling trademark.

FREE SUBSCRIPTIONS

Lectrix®, Electronics Cooling®—The 2020 Summer Edition is distributed annually at no charge to engineers and managers engaged in the application, selection, design, test, specification or procurement of electronic components, systems, materials, equipment, facilities or related fabrication services. Subscriptions are available through electronics-cooling.com.

LECTRIX®

EDITORIAL

Victor A. Chiriac

Associate Technical Editor



Dear Readers,

On behalf of the editorial board, I am pleased to welcome you to the 2020 summer edition of the *Electronics Cooling*. We are excited to share with you featured articles, Calculation/Statistics Corner, Tech Brief, and other materials that we hope will be of interest to you and will provide a great learning experience.

So far, in the first few months of 2020 we have experienced challenging times with the worldwide COVID-19 pandemic outbreak. Yet, these challenges could turn into great creativity and multiple opportunities for technology developments and breakthroughs in several areas of life. Our daily lives are changing at a fast pace, driven by an increase in connectivity and mobile communication, and technology is at the forefront of the fight against the spread of the virus.

Telecommunication is critical for businesses across many industries, including the medical field. The medical doctors started to use the digital platforms to consult, prescribe medicines, and keep their patients updated with the latest medical advice. Telemedicine is thus assisting the diagnostic and treatment process. Ventilators are essential equipment for providing critical treatment. Engineering firms are looking at using 3D printing to manufacture the needed respirator components, with the goal of making them available to health care providers. Artificial intelligence (AI) could become a powerful tool for predicting the COVID-19 disease's future trend, and even looking for possible treatments. Biotech companies use AI technology to analyze millions of immune cells in order to identify those cells that are able to produce antibodies to help the patients recover. Thanks to AI, 500 antibodies have been identified as possible candidates for use in future coronavirus therapies. Also, machine learning was used to determine that the loss of smell and taste are among the most common indicators, a fact not widely known in the early days of the virus outbreak.

These are just a few examples of projects and initiatives that wouldn't have been possible during previous pandemics or epidemics due to the lack of infrastructure to collect and process data at this scale, and there was no social media to encourage people to get involved. But, there are also technology advancements that are accelerated by the current pandemic needs, a race where the tech giants are either growing or fading away. This is true, especially in the mobile/communication sector where the growth/decay cycles are so fast these days that any misstep could impact severely the business and market share of competing companies.

Although we are living tough times, we have a mission to assist in the development of new cooling technologies and innovation that will make the society recover, grow, and become stronger in the future. It is a call for reinvention happening across the industry that affects companies, society, and, ultimately, our lives. Traditional industries are merging and evolving together: the automotive, the health care, the computing, and telecommunication industries create a renewed environment for growing business success. The 5G technology will provide the infrastructure needed to carry large amounts of data, allowing for a smarter and more connected world. Everything requires higher performance, more data, and faster processors, and with thermal management and electronics cooling at the center of it all! The role of the thermal engineer will become more critical due to the convergence of the above-mentioned industries requiring dedicated and customized innovative cooling solutions. As the world is changing and evolving, it may be as well the time for the thermal engineers to take a lead and expand their contribution and industry impact beyond the traditional support role.

I encourage our *Electronics Cooling* readers to provide their feedback and share with us and the thermal community articles that provide an insight into the novel and exciting work happening across all the industries, from large companies that build the future to small technology firms that nibble at tech breakthroughs, and all together push the boundaries of our known thermal limits! We invite you to become active members of our *Electronics Cooling* community, and we welcome your technical contributions and feedback for the improvement of our publication. Thank you for your continued support.

Happy readership: stay healthy and creative!!!

– **Victor A. Chiriac**

Industrial



Consumer



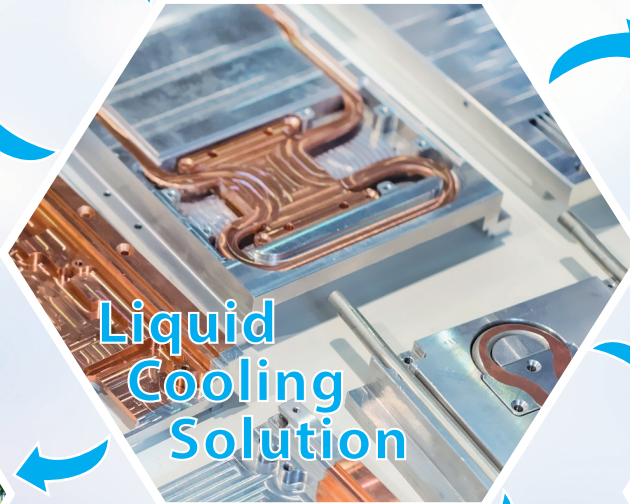
Networking / Telecom



Renewable Energy Solutions



Liquid Cooling Solution



Server / AI



Autonomous Systems



Liquid Cooling Solutions

Professionally designed, built and tested to withstand harsh environments

- High performance Coolant Distribution Unit (CDU)
- Impinging cold plate design with lower pressure drop
- Broad range of testing equipment to ensure product quality and performance
- Micro-channel cold plate block designs
- Liquid direct cooling for memory DIMMs
- High-grade tubing with low permeation, high-pressure capacity and small bending radii achievable
- Hot-swappable quick-disconnect capability for dry disconnect

www.delta-fan.com | dcfansales.us@deltaww.com

 **DELTA**
Smarter. Greener. Together.

Application of Transient Thermal Methods to Moisture Diffusion Calculations, Part 2

Reprinted from the *Electronics Cooling*® 2013, Spring Issue

Bruce Guenin
Assoc. Technical Editor

INTRODUCTION

This two-part column was motivated by concerns regarding the important role of organic materials in electronic systems and their accompanying vulnerabilities due to moisture diffusion. The methods described herein are intended to provide an efficient means of predicting the rate of moisture diffusion under a variety of conditions in order to better manage the associated risks.

Part 1 established the basic validity of the methodology and demonstrated its use in modeling one-dimensional (1D) diffusion flow geometries[1]. Part 2 continues the development of these methods and applies them to a variety of situations of practical importance.

CALCULATION METHOD FOR 2D DIFFUSION GEOMETRIES

As demonstrated in Part 1, the use of a multi-stage resistor-capacitor (RC) network, solved using a numerical method, can be extended beyond its original scope involving thermal transient modeling to the prediction of moisture diffusion. It can be adapted to various geometries by using the appropriate analytical formulas for calculating the particular values of R and C. The ex-

clusion of the numerical method is relatively independent of these geometrical details.

Figure 1 depicts the geometry assumed in the calculation, that is representative of the design of organic laminates used in package substrates and printed circuit boards (PCBs). It represents a single dielectric core region in a multi-layer package substrate. The core material is the same as that in Part 1, namely, bismaleimide triazine (BT). The BT is assumed to be 0.015 cm thick and is 1 cm square. It is assumed to be sandwiched between two continuous copper planes. The presence of the copper is not explicitly accounted for in the model. Their effect, as far as the model is concerned, is to prevent any diffusion of moisture into the BT from its top and bottom surfaces. Moisture can only diffuse into the core by way of the exposed edge. Note that this is a rather constraining condition. To the extent that the metal planes prevent the diffusion of moisture from one core to another, it is only necessary to model a single core to capture the physics of the diffusion process.

However, in the real world, life is not quite this simple. Typically, in laminated organic package substrates and PCBs, there are perforations in the metal planes as required by the fabrication process

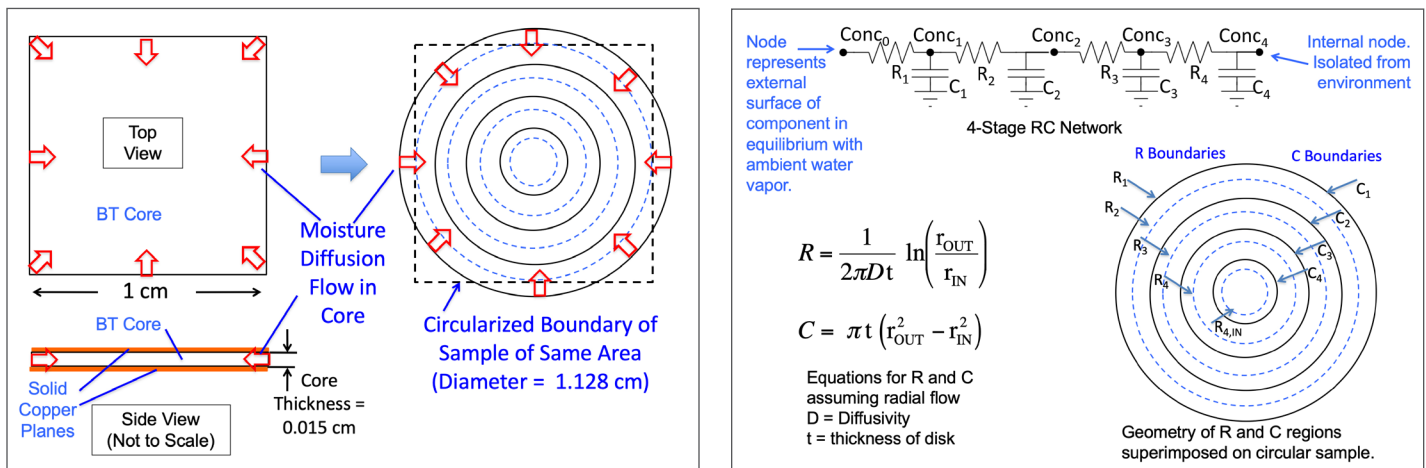


Figure 1: a) Diagram of diffusion sample (left). b) Four-stage transient RC circuit representing the diffusion process. Diagram of boundaries for capacitor regions (solid lines) and resistor regions (dotted lines). Equations shown, for calculating R and C values, representing 2D diffusion (right).

or resulting from via or trace routing in the laminate. These perforations would serve to provide additional paths for moisture to diffuse into the interior regions of the laminate. Hence, the time for moisture diffusion in actual components would tend to be less than that predicted here. However, the simple construction assumed here will enable us to more efficiently explore the basic physical effects involved with the exchange of moisture between an organic substrate and the ambient air and simultaneous diffusion within the component.

Before the numerical method can be applied, it is necessary to subdivide the sample into several regions, each of which must be represented by a separate value of R and C in the RC circuit. There is no standard way to do this. However, the method used in Part 1 for a 1D flow in a slab-shaped component can be adapted to the 2D situation as follows:

- Circularize the square by transforming it into a disk having an equal area. This has been shown to be a reasonable approximation for radial heat flow in a square geometry[2].
- To create the capacitor volumes, divide the disk into four annular regions for which $r_{OUT} - r_{IN} = r_{DISK}/4$, where r_{OUT} and r_{IN} are the outer and inner radii of a given annulus and r_{DISK} is the radius of the disk. This is depicted by the array of concentric solid-line circles in *Figure 1*.
- The resistor geometries span two adjacent annuli and terminate at the bisecting radius of each. [The bisecting radius divides each capacitor annulus into two equal areas.] This is depicted by the array of concentric dotted-line circles in *Figure 1*.
- The C and R values can be calculated using the particular values of r_{OUT} and r_{IN} of the appropriate annuli and the appropriate formula in *Figure 1*.

Table 1 lists the inner and outer radii for each C and R region, and the resultant C and R values. The R calculations assume three different diffusion coefficients, one for each of the three BT temperatures assumed in the case studies to follow.

ADAPTING DIFFUSION CALCULATION METHOD TO DIFFERENT ENVIRONMENTS

Visually, the most prominent feature of the four-stage RC circuit is the ladder arrangement of the resistor and capacitor symbols. From a physical perspective, the topology of this network and the particular R and C values will determine how rapidly moisture will be transported through the structure.

However, the value of $Conc_0$, the moisture concentration at the outer skin of the BT, is important in providing the potential difference to drive the diffusive flow of moisture either into or out of the BT. The value of $Conc_0$ is, in turn, determined entirely by the local relative humidity (RH) at the exposed surface of the BT and by its local temperature.

Hence, in order to accurately predict the instantaneous diffusion rate within the BT, it is necessary to determine:

- The diffusion coefficient—it is determined only by the choice of organic material and its temperature.
- Local RH at the exposed surface of the organic material—determined by the ambient temperature and RH and the local temperature of the material.
- Equilibrium value of $Conc_0$ —determined by the local temperature and local RH and the choice of organic material.

The following sections provide procedures for calculating each of these properties and the relevant environmental conditions:

Diffusion Coefficient

In Part 1, a method of calculating D for BT was described using *Equation 3* (in Part 1), and assuming an activation energy for moisture diffusion of 0.48 eV. *Table 2* provides calculated values of D at temperatures of interest. Since D is an exponential function of temperature, its value changes significantly with changes in temperature.

| CIRCUIT ELEMENT | MAT'L | INNER RADIUS | OUTER RADIUS | THICKNESS | TEMPERATURE | D | R | C |
|-----------------|-------|--------------|--------------|-----------|-------------|----------|----------|--------|
| | | (cm) | (cm) | | | | | |
| R1 | BT | 0.499 | 0.564 | 0.015 | 60 | 1.29E-08 | 1.01E+08 | |
| R2 | BT | 0.360 | 0.499 | 0.015 | 60 | 1.29E-08 | 2.69E+08 | |
| R3 | BT | 0.223 | 0.360 | 0.015 | 60 | 1.29E-08 | 3.93E+08 | |
| R4 | BT | 0.100 | 0.223 | 0.015 | 60 | 1.29E-08 | 6.62E+08 | |
| R1 | BT | 0.499 | 0.564 | 0.015 | 85 | 3.03E-08 | 4.32E+07 | |
| R2 | BT | 0.360 | 0.499 | 0.015 | 85 | 3.03E-08 | 1.14E+08 | |
| R3 | BT | 0.223 | 0.360 | 0.015 | 85 | 3.03E-08 | 1.67E+08 | |
| R4 | BT | 0.100 | 0.223 | 0.015 | 85 | 3.03E-08 | 2.82E+08 | |
| R1 | BT | 0.499 | 0.564 | 0.015 | 105 | 9.44E-08 | 1.39E+07 | |
| R2 | BT | 0.360 | 0.499 | 0.015 | 105 | 9.44E-08 | 3.67E+07 | |
| R3 | BT | 0.223 | 0.360 | 0.015 | 105 | 9.44E-08 | 5.37E+07 | |
| R4 | BT | 0.100 | 0.223 | 0.015 | 105 | 9.44E-08 | 9.04E+07 | |
| C1 | BT | 0.423 | 0.564 | 0.015 | | | | 0.0066 |
| C2 | BT | 0.282 | 0.423 | 0.015 | | | | 0.0047 |
| C3 | BT | 0.141 | 0.282 | 0.015 | | | | 0.0028 |
| C4 | BT | | 0.141 | 0.015 | | | | 0.0009 |

| TABLE 2 | | |
|---|-----------------------------|------------|
| Calculated Coefficient for Moisture Diffusion in BT | | |
| T (°C) | D(T) (cm ² /sec) | D(T)/D(20) |
| 20 | 1.32E-09 | 1.0 |
| 30 | 2.47E-09 | 1.9 |
| 40 | 4.44E-09 | 3.4 |
| 50 | 7.69E-09 | 5.8 |
| 60 | 1.29E-08 | 9.8 |
| 70 | 2.10E-08 | 15.9 |
| 80 | 3.33E-08 | 25.2 |
| 90 | 5.14E-08 | 39.0 |
| 100 | 7.75E-08 | 58.8 |

Relative Humidity at Interface with the Sample

The value of RH at the interface with the polymer component plays a significant role in the ultimate moisture concentration in the sample. It is critically dependent on the ambient temperature. In situations in which the substrate temperature differs from that of the ambient, then this difference must be taken into account. The following equation, which provides the relationship between the partial pressure of water in the atmosphere, at saturation, as a function of temperature, can be used as the basis of all the required relative humidity calculations.

$$P_{Water,Sat}(T) = \frac{e^{(77.3450+0.0057-7235/T)}}{T^{8.2}} \quad (1)$$

where $P_{Water,Sat}$ is the partial pressure of water in units of Pa and T is the absolute temperature, in units of K [3]. At a given value of RH, the partial pressure of water is simply equal to

$$P_{Water}(T,RH) = RH \cdot P_{Water,Sat}(T) = RH \cdot \frac{e^{(77.3450+0.0057-7235/T)}}{T^{8.2}} \quad (2)$$

Equation 2 was used to generate the various curves of P_{Water} vs. temperature at specified values of RH in Figure 2a. Equation 2 was also used to create the curves in Figures 2b and c. Their behavior results from the fact that, when a surface is maintained at a local temperature different from the ambient, the RH value at that surface is also different from the ambient RH. Figure 2b assumes an ambient temperature of 20°C. When a given surface is heated the

partial pressure of the water in the air at its surface is unchanged. However, since the hotter air at the interface has a higher $P_{Water,Sat}$, the local RH is reduced compared with the ambient value. Conversely, when a surface is cooled, the RH increases and can lead to condensation (i.e.: the local RH reaches 100%). The graph accounts for that effect also. Figure 2c shows the same sort of curves, but this time, assuming an ambient temperature of 40°C. The higher value of $P_{Water,Sat}$ at a 40°C ambient leads to higher values of local RH at a given surface temperature than for 20°C.

Moisture Concentration at the Sample Surface

The relationship between the saturated moisture concentration and ambient temperature and RH for BT samples in equilibrium with the ambient has been quantified through weight measurements on saturated samples [4].

Figure 3 shows the result of applying a regression analysis to the raw data from the reference and provides a means of estimating values of moisture concentration at values of temperature and RH other than those measured. Furthermore, a power law regression (not shown on the graph) was generated for each trendline and was used to estimate values for RH between 0 and 40%.

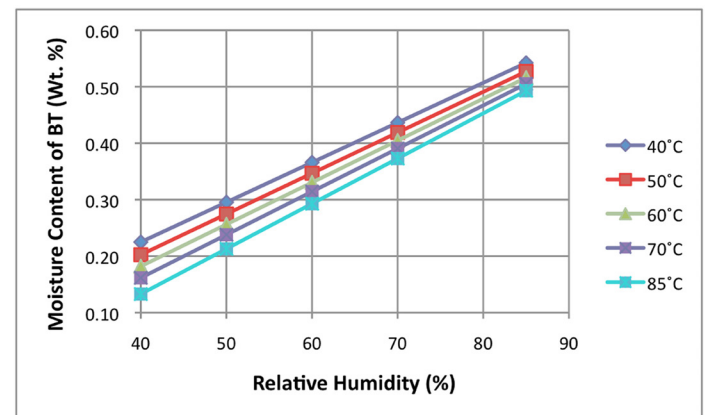


Figure 3: Saturated moisture content of BT vs relative humidity and ambient temperature. Regression fit to data in Ref [4].

MOISTURE DIFFUSION CALCULATIONS FOR SIX CASE STUDIES

A total of six case studies were performed. They are listed in Table 3. In all cases there was a soak process under 85°C/85%RH

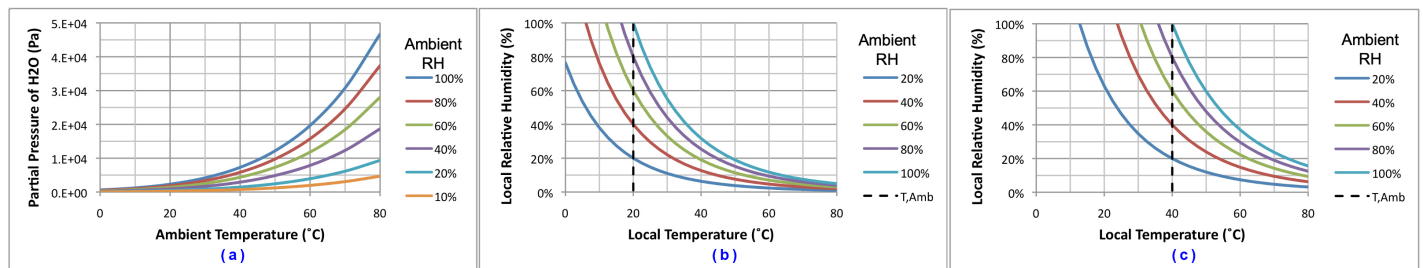


Figure 2: a) Graph of H₂O partial pressure vs. ambient temperature and relative humidity, b) & c) Local relative humidity at sample surface vs. local sample temperature and ambient RH.

conditions. For Case 1, the soak process lasted for 500 hours, and was simulated explicitly. For all other cases, they were assumed to proceed to saturation. They were not explicitly simulated. Their effect was represented by assigning a constant value of concentration (equal to 8.85 mg/cm³) to all of the capacitors as an initial condition in the bakeout simulation.

Cases 1 and 2 are similar to the one analyzed in Part 1. The simulation results for these cases are shown in Figure 4. In this figure, the top row of graphs plot the value of moisture concentration calculated for each of the capacitors at various values of elapsed time. For a given time, the radius value associated with each data point represents that of the bisecting radius of each capacitor.

| TABLE 3 Environmental Conditions Assumed in Diffusion Case Studies | | | | | | | | |
|---|-----------------------------------|---------------|----------------------------|--------------------|--------|---------|-----------------------|----------------------------|
| Case # | SOAK CONDITIONS | | | BAKEOUT CONDITIONS | | | | |
| | Temperature/ Relative Humidity | Soak Time | Conc @ BT/Air Interface | Air Temp | Air RH | BT Temp | RH @ BT/Air Interface | Conc @ BT/Air Interface |
| | (°C/% RH) | (hrs) | (mg/cm ³) | (°C) | (%) | (°C) | (%) | (mg/cm ³) |
| 1 | 85/85 | 500 | 8.85 | 20 | 20% | 105 | 0.4% | 0.00 |
| 2 | 85/85 | To Saturation | 8.85 | 20 | 20% | 105 | 0.4% | 0.00 |
| 3 | | | | 20 | 20% | 60 | 2.4% | 0.07 |
| 4 | | | | 20 | 60% | 60 | 7.1% | 0.33 |
| 5 | | | | 40 | 40% | 60 | 14.8% | 0.83 |
| 6 | | | | 40 | 60% | 60 | 22.2% | 1.52 |

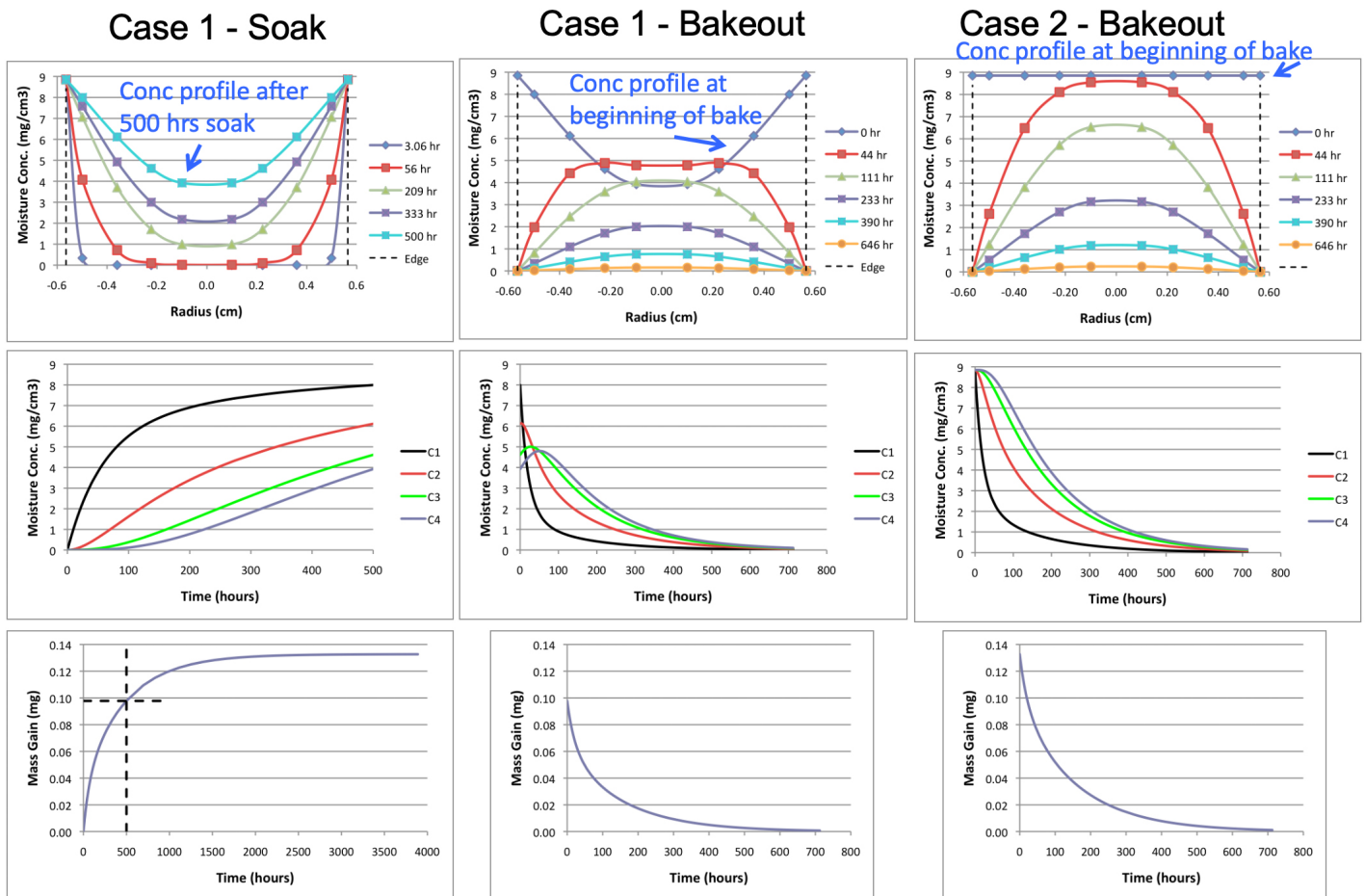


Figure 4: Solution results for BT samples, 85 °C/85%RH soak and 105 °C bakeout exposure. a) 2D diffusion profile versus time. b) Concentration values at each capacitor versus time. c) Mass gain curve versus time.

The middle row of graphs plot the concentration calculated for each capacitor versus time. C1 is associated with the outermost annulus. As such, its concentration is the fastest to rise during soaking and likewise to fall during bakeout.

The bottom row of graphs plots the total mass of absorbed moisture vs time. It is calculated using Equation 3, below.

$$M_{H_2O} = \sum_{i=1}^4 Conc_i \cdot C_i \quad (3)$$

(Note that the equivalent equation in Part 1 (Equation 4) had a prefactor equal to 2 to compensate for the half symmetry of the 1D model.)

The results for the soak process in Case 1 are worth noting. In spite of the 500 hr duration, the moisture concentration at the center of the sample reached only about half of its saturation value. This is simply due to the rather large radius on the modeled sample, equal to 0.56 mm. By comparison, in Part 1, the diffusion length between the mid-plane and the exterior surface of the sample was 0.012 mm. Here, full saturation was achieved in only about 4 hours.

The bakeout process for these two cases assumes the use of an oven set to a temperature of 105°C. Since the oven is assumed to be open to the atmosphere, in the vicinity of the BT, a very low RH value of 0.4% is calculated. At this high temperature, the diffusion coefficient is high enough that the bakeout is complete at approximately 650 hrs. This was nearly independent of the initial moisture content of the BT at the start of bakeout.

The bakeout process for Cases 3-6 is more representative of conditions in application environments. In all four cases, the temperature of the BT was assumed to be 60°C, which was higher than the ambient temperature in each case.

Cases 3 and 4 assume an ambient temperature of 20°C, at RH values of 20% and 40%, respectively. These would be considered rather mild application environments and would be representative of ASHRAE data center guidelines of today. These results are displayed in Figure 5. The time required for the moisture content to reach a steady minimum is nearly 5,000 hours.

As mentioned, this is probably a conservative estimate. However, it is indicative of a much slower drying process than in a dedicated bakeout oven. One notes, also, the beginning of a trend in that the residual moisture level in the BT is greater than the near

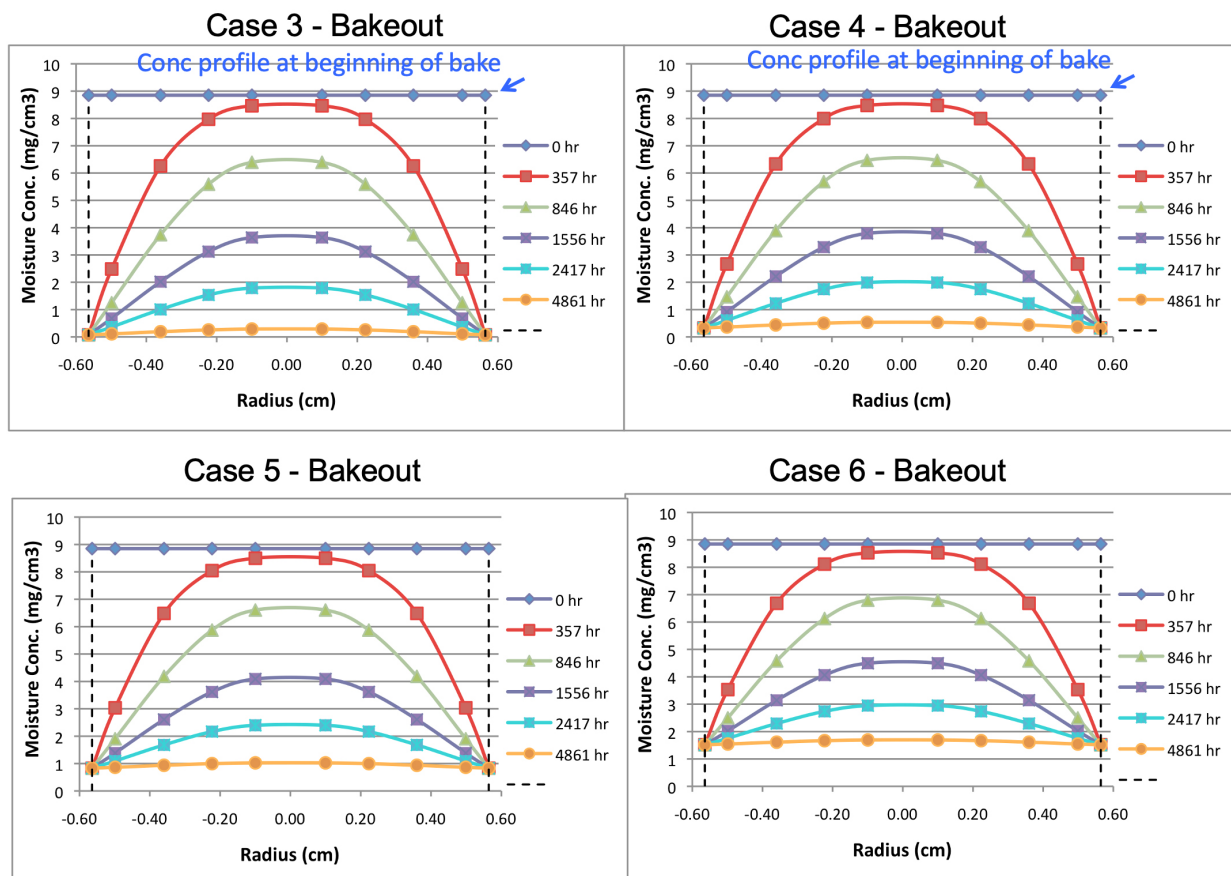


Figure 5: Solution results for BT samples, Cases 3-6, showing change in diffusion profile versus time due to bakeout process at varying ambient temperature and RH values

zero value obtained in the bakeout oven. These residual moisture concentration levels were calculated at 0.07 and 0.3 mg/cm³, respectively.

There is a trend among data centers to push ambient temperature and RH values to higher levels in the interest of improving data center cooling efficiency. ASHRAE has been supportive of this trend by relaxing temperature and humidity guidelines and allowing temperatures in the 40 to 45°C range, with appropriate controls on humidity [5]. Cases 5 and 6 assume an ambient temperature of 40°C and RH levels of 40 and 60%, respectively. The results in Figure 5 indicate a similar time for the residual moisture to reach a stable value. This should not be a surprise, since this is largely the result of the BT temperature, since this determines the diffusion coefficient. However, the residual concentration values of 0.8 and 1.5 mg/cm³ are significantly higher than those associated with the 20°C ambient.

CONCLUSIONS

Computationally efficient methods have been demonstrated that are useful in calculating moisture diffusion rates for simple geometries over a wide range of ambient conditions of temperature and humidity.

The use of ambient air with elevated temperature and humidity levels for cooling electronic components containing organic materials has been shown to promote a higher concentration of residual moisture in these materials. It behooves the industry to not only quantify moisture levels in organic materials more effectively, but also to better understand the impact of increased moisture levels on the reliability and electrical performance of these materials.

REFERENCES

1. B. Guenin, "Application of Transient Thermal Methods to Moisture Diffusion Calculations, Part1," ElectronicsCooling, Vol. 18, No. 4 (2012).
2. B. Guenin, "Heat Spreading Calculations Using Thermal Circuit Elements," ElectronicsCooling, Vol. 16, No. 3 (2010).
3. Engineering Toolbox webpage," http://www.engineeringtoolbox.com/water-vapor-saturation-pressure-air-d_689.html
4. M. Pecht, H. Ardebili, A. Shukla, J. Hagge, and D. Jennings, "Moisture Ingress Into Organic Laminates," IEEE Trans. Comp. Pack. Tech., Vol. 22, No. 1, (1999) pp. 104-110.
5. R. Schmidt, "A History of ASHRAE Technical Committee TC9.9 and its Impact on Data Center Design and Operation," ElectronicsCooling, Vol. 18, No. 4 (2012).

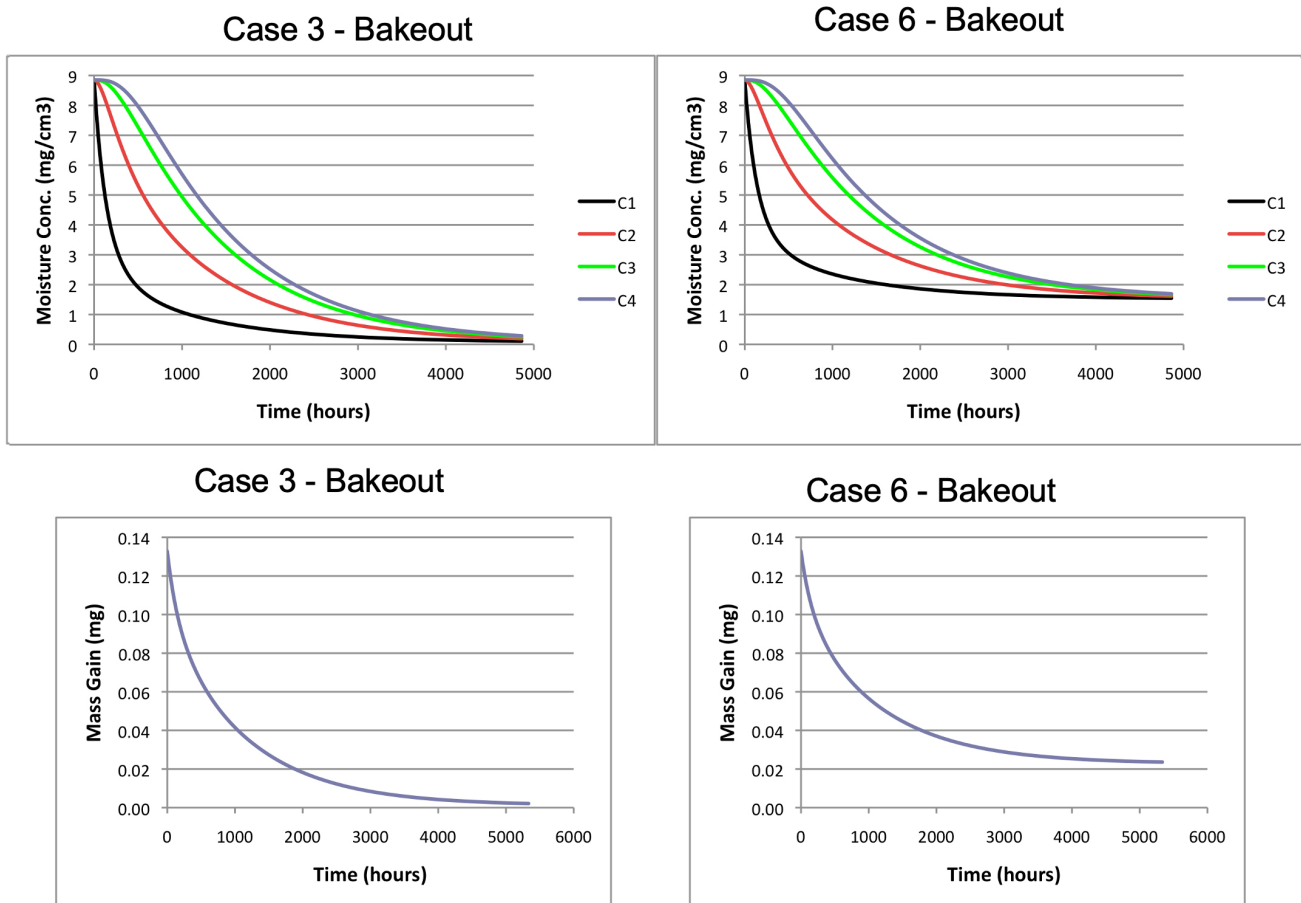


Figure 6: Additional plots of Cases 3 and 6: moisture concentration values at each capacitor versus time and mass gain curve versus time.

Normal Distribution

Ross Wilcoxon
Assoc. Technical Editor

INTRODUCTION

The previous column in this series [1] discussed statistical probability and showed that the plot of the probability of a given value occurring within a population can look like a hill in which there is a peak in the middle that tapers off to increasingly smaller slopes on each side. The example in that column referred to the scores produced by shaking a number of dice, and the ‘hilly’ plot was described with the more common term of ‘bell-shaped curve’. The purpose of establishing a probability distribution to describe a population of data with uncertainty is that it provides a mathematical framework for dealing with that uncertainty—if a reasonable mathematical model of the distribution curve can be defined. As we will see in subsequent columns, many different models for probability distributions exist; the selection of the correct model depends on characteristics of the population and what data are available for analysis.

This column focuses on the probability model that is most widely used and most recognized: the Gaussian, or normal, distribution. The normal distribution, as written in terms of a probability density function is shown in Equation (1):

$$f(x) = \frac{1}{\sigma\sqrt{2\pi}} e^{-\frac{1}{2}\left(\frac{x-\mu}{\sigma}\right)^2} \quad (1)$$

Equation (1) allows one to estimate the probability of a given value, x , occurring in a population that is defined with the two parameters μ and σ . While the normal distribution equation itself may not be familiar to everyone, the terms μ and σ should be recognizable to anyone who deals with data: μ is the mean (or average) value and σ is the standard deviation. If the mean and standard deviation of a population are known, the probability that a randomly selected member of that population will have a value of x can be calculated with Equation (1). Or, if you are like me and rely on spreadsheets to do most of your calculations, you can use the function: `@norm.dist(x, μ , σ , false)`.¹

The mean and standard deviations can be calculated for a set of N samples, x_1, x_2, \dots, x_n , by:

$$\mu_s = \frac{\sum_{i=1}^N x_i}{N} \quad (2)$$

$$\sigma_s = \sqrt{\frac{\sum_{i=1}^N (x_i - \mu_0)^2}{N}} \quad (3)$$

Equations (2) and (3) include the subscript ‘s’ for the mean and standard deviation as a reminder that the values determined from a sample (the set of data drawn from a population) are not exactly equal to those for the entire population (all possible elements). Traditionally, the mean and statistical deviation of a sample are written as \bar{x} and s , respectively. A future column in this series will discuss how to use the values of μ_s and σ_s , also known as \bar{x} and s , to determine a range in which we can be confident that the population mean, μ , actually lies. Note that the mean and standard deviation of a data set can be calculated in a spreadsheet with the functions `@average(‘data’)` and `@stdev(‘data’)`, respectively, where ‘data’ refers to the cells that contain the data.

Our familiarity with the term ‘average’ can lead to its occasional misuse, which can be avoided if we keep its relationship to the normal distribution in mind. The version of the classic illustration of a misuse of the term ‘average’ is the example of nine people, who all have a net worth of \$500,000, are sitting in a bar. In walks the founder of a “multinational conglomerate technology company that focuses on e-commerce, cloud computing, digital streaming, and artificial intelligence” who has a net worth of \$140B. Using Equation (2), the average net worth of the individuals in the bar suddenly increases to \$14B, which may be mathematically correct but not physically relevant. The primary basis for this discrepancy is the fact that the population of the 10 individuals in the bar is not representative of a normal distribution. In cases like this, the median may be a more appropriate parameter for reporting a typical value. The median is the middle value in a ranked list of the

¹The ‘false’ in this equation specifies that the probability distribution (a bell-shaped curve that goes to zero as x goes to infinity) is calculated. If ‘true’ is used instead, the function returns the cumulative distribution (an S-shaped curve that goes to 1 as x goes to infinity)

²Equation (2) defines the arithmetic mean, which is the same as the arithmetic average. The more generic terms mean and average are often used interchangeably, but can refer to different definitions.

sample set such that an equal number of values are greater than and less than it (the spreadsheet function for calculating median is @median('data'). When the mean and median of a data set are substantially different, such as in the aforementioned example of the people in the bar, one should suspect that the sample set is not normally distributed.

A fundamental strength and justification for utilizing the normal distribution is the central limit theorem, which shows that when multiple, independent random variables are added, the result tends towards a normal distribution—even if the variables themselves are not normally distributed (see for example *Reference [2]*). *Reference [1]* discussed the results of throwing dice, beginning with the assumption that a single die is 'fair' such that the probability of it showing any particular value is equal to the inverse of the number of sides on the die (i.e., 1/6th for a six-sided die). The distribution of scores that result from throwing that one die is certainly not normal; it would be a straight line with equal probability of 16.7% for each of the six values. With two dice, the distribution had a triangular shape and, as the number of dice increased, the distribution looked more and more like a bell-shaped curve.

Figure 1 shows simulated results for throwing 6 six-sided dice 100 and 5,000 times. The larger number of throws leads to a more well-behaved distribution of results (red bars appear to be more 'bell shaped'). However, both data sets produce very similar normal distributions with mean values of ~21 and standard deviations of 4.2. This illustrates the power of the normal distribution and the results of the central limit theorem. Even when we have results from a small data set that in of itself does not appear to be normally distributed (have a 'clean' bell-shaped curve), if the data were drawn from a normal distribution there is a good chance

that they can be used to accurately estimate the fundamental characteristics of that population.

The normal distribution provides a straightforward method for using measurable characteristics of a data set (the mean and standard deviation of the sample) to estimate the probabilities of future measurements falling within a prescribed range of values (related to the properties of the entire population). This is incredibly useful in that it allows us to perform tasks such as:

- Determining how many samples must be measured to have confidence that a population has been adequately characterized
- Comparing different data sets and decide with they are from the same population or not (e.g. to determine if differences in their mean values are 'statistically significant')
- Deciding whether a value that seems to be an outlier is likely to be from the population that we are evaluating or if it is due to a factor such as a measurement error,
- Defining how much confidence we should have in a curve fit we generate from a data set

These types of practical tools are all topics that will be discussed in future columns, now that these foundational topics of probability and distributions have been covered.

REFERENCES

1. Ross Wilcoxon, "Statistics Corner—Probability", Electronics Cooling Magazine, Spring 2020, pp. 16-18
2. http://sphweb.bumc.bu.edu/otlt/MPH-Modules/BS/BS704_Probability/BS704_Probability12.html

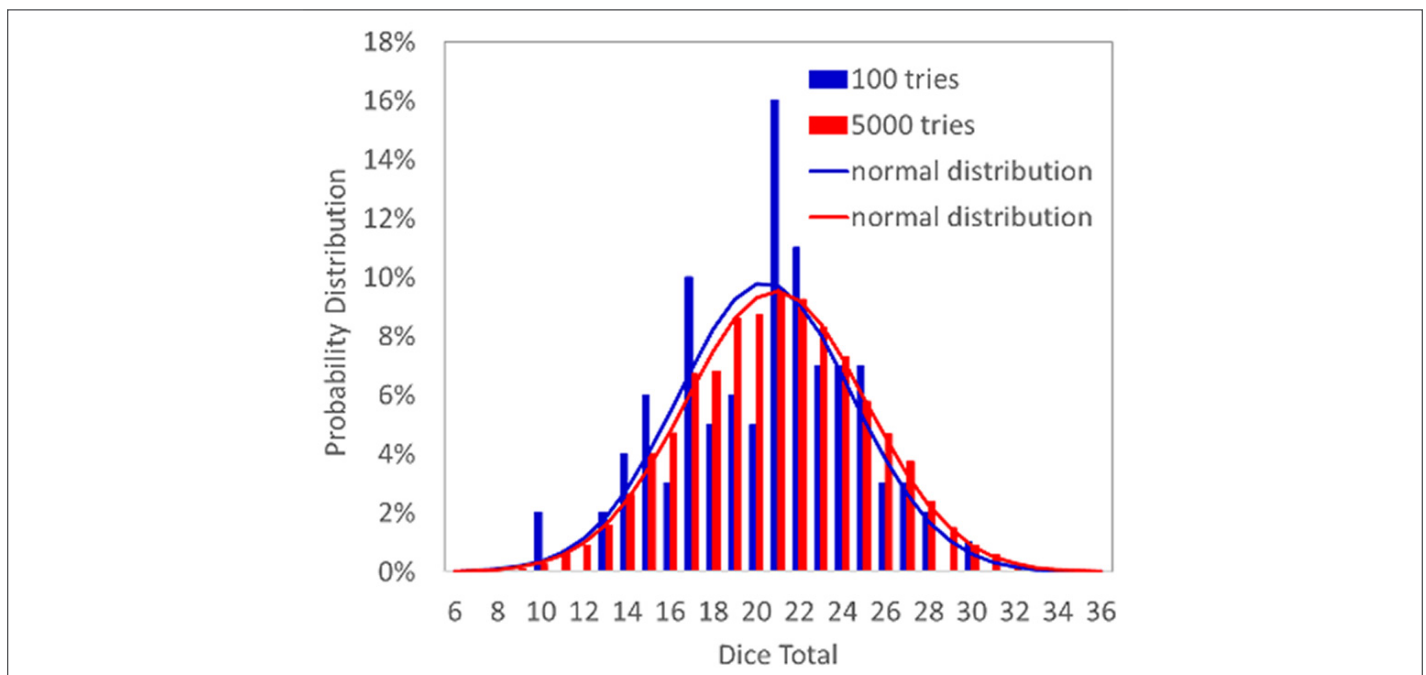


Figure 1: Simulated results for throwing 6 six-sided dice.

Effective Heat Spreading Angle

Reprinted from the *Electronics Cooling*® 2015, Fall Issue

Dirk Schweitzer

Infineon

dirk.schweitzer@infineon.com

INTRODUCTION

To accurately compute the thermal resistance of a layered structure, such as the Junction-to-Case thermal resistance of a power semiconductor, the heat spreading inside the structure has to be considered. The calculation of the spreading resistance is not a trivial problem [1] and analytical solutions exist only for extremely simple geometries.

Using finite element analysis (FEA) the heat spreading and resulting temperature distribution can be accurately computed. But for a quick and simple analysis of the spreading resistance, the thermal engineer has to resort to rules of thumb such as the 45° spreading angle [2, 3], or to approximation formulas which can be found in literature [1, 4]. This article presents an alternative approach, namely the concept of the effective heat spreading angle [5].

EFFECTIVE HEAT SPREADING PROFILE

To explain this concept we consider a silicon chip on a copper (Cu) leadframe as shown in *Figure 1*. A power of $P_H = 10$ W is dissipated homogeneously on an active area of 1.0×1.0 mm² on the 3.0×3.0 mm² chip whereas the bottom temperature of the leadframe is kept constant (ideal cooling).

Monitoring the local heat flux density $p(x)$ from the center of the die surface to the center of the bottom surface (x being the distance from the heat source), *Figure 2*, we notice that the heat flux density drops continuously from initially 10 W/mm² to about 1 W/mm² at the bottom. Obviously the heat spreading is the reason for the decreasing heat flux density. If the cross sectional area of the heat flow path was constant the heat flux density would also remain constant throughout the structure. Since the variation of the heat flux density is closely related to the amount of heat spreading, the obvious idea was to derive a measure for the spreading angle from the derivative dp/dx of the heat flux density.

For simplification we shall assume that the heat flux is homogeneously distributed over each cross section $A(x)$ of the heat flow path (which is not the case in reality). At each position x , the product of cross-sectional area $A(x)$ and heat flux density $p(x)$ equals the total power dissipation P_H .

$$A(x)p(x) \tag{1}$$

Furthermore, we shall assume that the shape of the heat flow cross section does not change as the heat propagates (which is not true either); i.e.: in this case it remains a square area independent of the distance x from the chip surface. For the half side length $y(x)$ of this square we obtain:

$$y(x) = \frac{1}{2} \sqrt{A(x)} = \frac{1}{2} \sqrt{\frac{P_H}{p(x)}} \tag{2}$$

Plotting $y(x)$ vs. distance x we obtain the *effective heat spreading profile* (*Figure 3*). We call this the *effective heat spreading profile* as opposed to the real spreading profile because it has been derived for above non-true assumptions. This approach is justified by the fact that we can use the effective heat spreading profile to calculate the spreading resistance within any desired accuracy. *Figure 4* shows a discretization of the effective spreading cone. In this example chip and leadframe are each subdivided into four slices and the die attach is represented by one more slice. The temperature drop ΔT_i across each slice can be calculated from the density p_i of the heat flux passing through it, its thickness d_i , and its thermal conductivity λ_i :

$$\Delta T_i = \frac{p_i}{\lambda_i} d_i \tag{3}$$

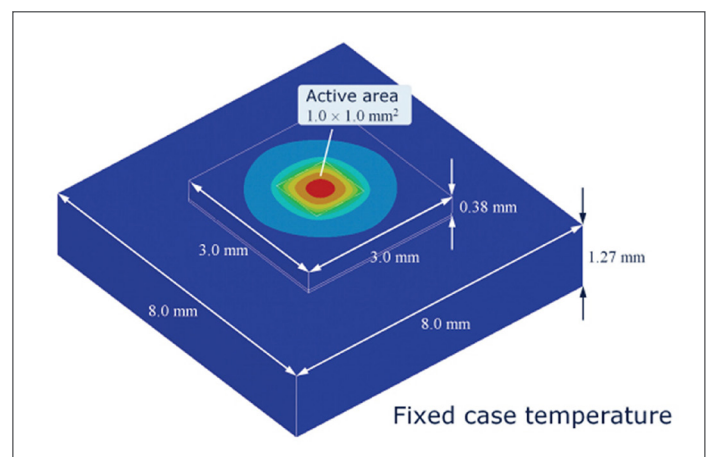


Figure 1: Silicon chip on Cu leadframe (solder die attach).

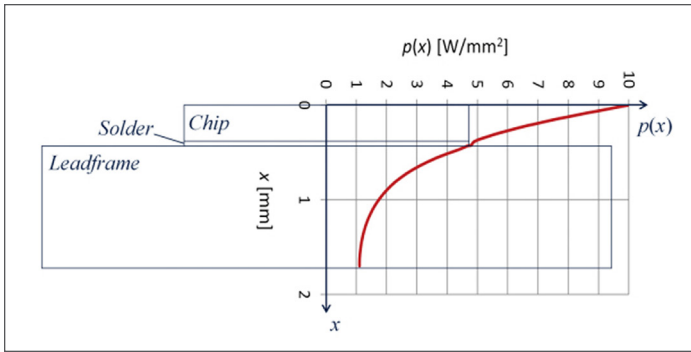


Figure 2: Heat flux density along heat flow path.

Because the cross sectional area A_i of each slice has been constructed such that $A_i = P_H / p_i$ we have:

$$\Delta T_i = \frac{P_H}{A_i \lambda_i} d_i = P_H \theta_i \quad \text{with} \quad \theta_i = \frac{d_i}{A_i \lambda_i} \quad (4)$$

where θ_i represents the thermal resistance of the i -th slice such that if we multiply it by the total heat flux P_H we obtain the correct temperature difference across that slice. Therefore, the sum over all slices:

$$\theta = \sum_{i=1}^n \theta_i = \sum_{i=1}^n \frac{d_i}{A_i \lambda_i} \quad (5)$$

approximates (and for $n \rightarrow \infty$ exactly returns) the thermal resistance of the structure. In practice even a rather coarse discretization of the effective heat spreading profile as in Figure 4 results in a quite good approximation of the actual thermal resistance (<1% error in this case). Application of the popular 45° heat spreading assumption on the other hand would overestimate the size of the spreading cone and thus result in a too low value for the thermal resistance (Figure 3).

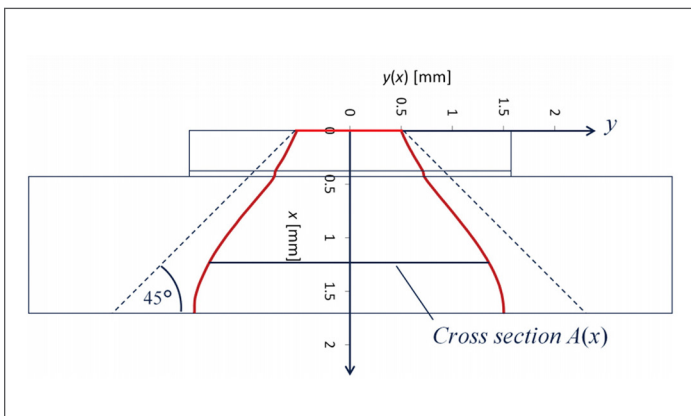


Figure 3: Effective heat spreading profile.

EFFECTIVE HEAT SPREADING ANGLE

Based on the effective heat spreading profile $y(x)$ the correspond-

ing effective spreading angle can be easily computed (Figure 5):

$$\tan \phi_{\text{eff}} = \frac{dy}{dx} \quad (6)$$

Using Equation (2) we obtain for the heat spreading cone with square cross section:

$$\tan \phi_{\text{eff}} = -\frac{1}{4} \sqrt{\frac{P_H}{p(x)}} \frac{1}{p(x)} \frac{dp}{dx} \quad (7)$$

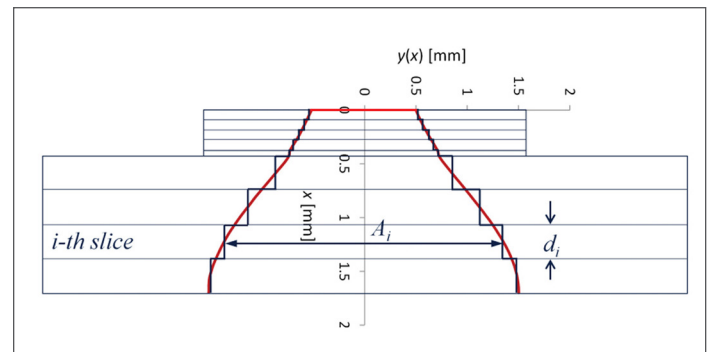


Figure 4: Discretization of the effective heat spreading cone.

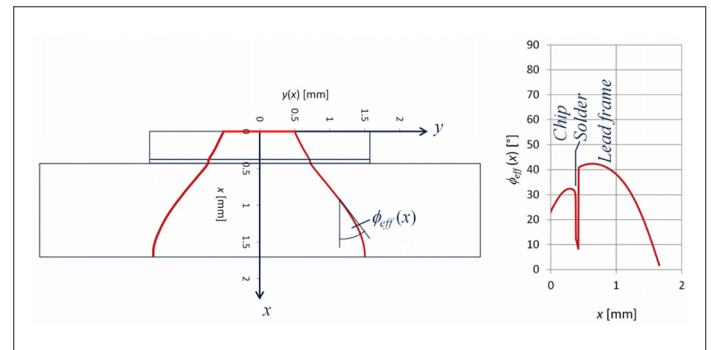


Figure 5: Effective heat spreading angle.

BENEFITS OF THE EFFECTIVE HEAT SPREADING CONCEPT

The attentive reader will now object: That is all well and good, but how do I know the heat flux density $p(x)$ along the heat flow path which is required to calculate the effective spreading profile?

Which is a valid objection, since $p(x)$ can only be obtained by finite element (FE) simulation. There would be little motivation to perform a FE simulation to calculate the heat flux density since we could as well use the FE simulation to directly compute the temperature difference and thermal resistance between junction and case.

In the author's view, the effective heat spreading concept serves two purposes. On the one hand it provides a clear definition of

heat spreading cone and spreading angle which so far is often based on a somewhat vague idea of how the heat is spread inside a structure. Heat spreading cone and angle can be visualized which helps us to gain insight into spreading mechanism and influencing factors. Looking at *Figure 3*, we see e.g. that the popular assumption of a 45° spreading angle is overly optimistic in that case. This is the educational aspect.

On the other hand, the effective heat spreading concept also serves a practical purpose. As shown in [5], we can often find generally applicable rules for the effective spreading angle which are valid not only for one particular case/device but provide a good approximation for a whole sub-class of cases (e.g. all power semiconductors with solder die attach). Based on these rules and *Equation (5)* we can implement more accurate spreadsheet calculators for the thermal resistance of this sub-class of devices.

FINAL REMARK

We could also try to define the spreading cone by a surface that intersects all isothermals at 90° angle thus ensuring zero heat flux across that border. But contrary to the approach presented above

the resulting heat spreading cone would be useless when it comes to computing the associated thermal resistance since the heat flow density over parallel cross sections of the spreading cone is not constant.

REFERENCES

1. Clemens J.M. Lasance, "Heat Spreading – Not a trivial Problem", *Electronics Cooling*, Vol. 14, No. 2, May 2008.
2. Bruce Guenin, "The 45° Heat Spreading Angle – An Urban Legend?", *Electronics Cooling*, Vol. 9, No. 4, Nov. 2003.
3. Yasushi Koito, Shoryu Okamoto, and Toshio Tomimura, "Two dimensional numerical investigation on applicability of 45° heat spreading angle", *Journal of Electronics Cooling and Thermal Control*, Vol. 4, pp. 1-11, 2014.
4. Seaho Song, Seri Lee, and Van Au, "Closed-Form Equations for Thermal Constriction/Spreading Resistances with Variable Resistance Boundary Condition," *IEPS Conference*, pp. 111-121, 1994.
5. Dirk Schweitzer and Liu Chen, "Heat Spreading Revisited – Effective Heat Spreading Angle", *Proc. 31st SEMITHERM*, San Jose, pp. 88-94, 2015.



IT'S HARD NOT TO USE A CONNECTOR THIS EASY.

CPC engineers design connectors with ergonomic thumb latches that make disconnecting quick and easy. Technicians are able to use an appropriate connection force and reduce repetitive stress. Many connectors also "click" when a secure connection is made.

Ease of use is just one factor that makes CPC connectors stand apart from the rest; discover them all.

Learn the difference purpose-built connectors make at cpcworldwide.com/LQ



©2020 Colder Products Company

37th Annual Semiconductor Thermal Measurement, Modeling and Management Symposium
March 22-26, 2021 at the DoubleTree by Hilton, San Jose, CA USA

About SEMI-THERM

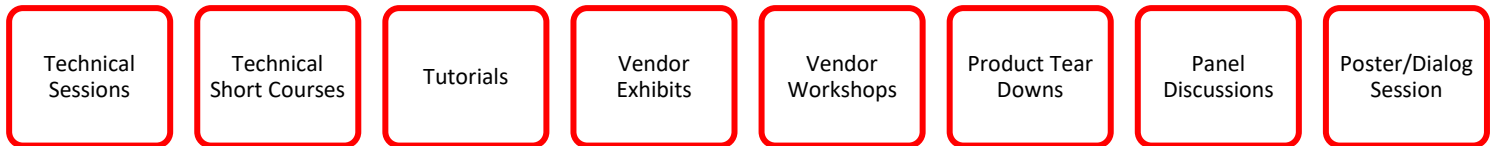
SEMI-THERM is an international symposium dedicated to the thermal management and characterization of electronic components and systems. Its goals are to:

- Provide knowledge covering all thermal length scales from integrated circuits to facility levels
- Foster discussions between thermal engineers, professionals and industry experts
- Encourage the exchange of information on academic and industrial advances in electronics cooling

Topics Include: Component/Board/System Thermal Design, Fluid Movers, Acoustics, Advanced Materials, Measurement Methods, Modeling & Simulation, Additive Manufacturing, Reliability, etc.

Applications Include: Processors/ICs/Memory, 3-D packaging, Computing Systems, Data Centers, Portable/Consumer/Wearable Electronics, Power Electronics, Harsh Environments, Defense/Aerospace Systems; Solid-State Lighting & Cooling, Biomedical; Micro/Nano-scale Devices, etc.

Symposium Highlights



Three options for participating in the technical program (additional details provided on [FAQs](#)):

Peer-reviewed paper: Submit a full **manuscript** for peer review in October. Authors notified of acceptance in November. Reviewer comments provided to authors in December. Final manuscript due in January. Manuscripts will be provided to conference attendees and uploaded to IEEE Xplore.

Non-peer-reviewed paper: Submit an **extended abstract** (2-5 pages) that describes the scope, contents, key results, findings and conclusions. Authors notified of acceptance in November. Final manuscript due in January. Manuscripts will be provided to conference attendees and uploaded to IEEE Xplore.

Presentation only: Submit an **extended abstract** (2 -5 pages) that describes the scope, contents, key results, findings and conclusions. Authors notified of acceptance in November. Final presentation slides are due in March. Presentations will be provided to conference attendees.

Note for authors of accepted 2020 SEMI-THERM (36) presentation/manuscripts: Please refer to the FAQs for guidance on resubmission of manuscripts and presentation-only submissions:
<https://semi-therm.org/presenters>

Awards: All papers with manuscripts are eligible for the Best Paper Award. Student papers presented at the conference are eligible for Student Scholarships. Presentation-only submissions are not eligible for awards.

| Manuscripts and extended abstracts submission deadline | Date that authors are notified of acceptance | Photo-ready full manuscript submission due date |
|--|--|---|
| Oct 4, 2020 | Nov 15, 2020 | Jan 17, 2021 |

Upload your paper electronically in RTF, DOC or PDF formats at www.semi-therm.org.

For further information please contact the Program Chair

Marcelo del Valle, E-mail: mvalle@infinera.com

Visit our website: <http://www.semi-therm.org>

**** All authors qualify for reduced symposium rates ****

The Future of Data Center Cooling: Passive Two-Phase Cooling

Raffaele Luca Amalfi¹, Filippo Cataldo², John Richard Thome³

¹Nokia Bell Labs, Efficient Energy Transfer Department, Murray Hill, New Jersey, USA

²Provides Metalmeccanica S.r.l., Micro-Cooling Department, Latina, Italy

³JJ Cooling Innovation Sàrl, Lausanne, Switzerland



Raffaele Luca Amalfi

Raffaele Luca Amalfi is a Lead Researcher at Nokia Bell Labs New Jersey, where he performs cutting-edge research in the field of thermal management of high-performance communications and computing systems across multiple scales. He is the Principal Investigator on behalf of Nokia of America Corporation and Bell Labs for the Eurostars Project PCOOLDATA focused on the development of innovative cooling solutions for data centers. Since 2016, he worked as Scientific Collaborator and Lab Manager at the Swiss Federal Institute of Technology of Lausanne (EPFL), at the Heat and Mass Transfer Lab, in Switzerland. In 2015, he joined Alcatel-Lucent Bell Labs in New Jersey, where he performed disruptive research on hybrid cooling technologies for telecom equipment. In 2012, he joined IBM Research Lab in Switzerland where he developed a novel cooling system for high-power electronics. He has received a Ph.D. in Energy Engineering from EPFL and he has authored more than 30 scientific publications.



Filippo Cataldo

Filippo Cataldo is a Senior Engineer at Provides Metalmeccanica S.r.l. in Italy working on micro-cooling solutions. He is the supervisor of the lab testing and design of micro-channels evaporators, condensers and passive systems, such as thermosyphons and heat pipes. He is the lead engineer for the E.U. funded projects (Clean Sky and PCOOLDATA). He has received a Ph.D. from University of Naples Federico II in 2015, where he gained extensive experience in experimental design/analysis, numerical modelling, energy conversion, and optimization of Organic Rankine Cycles. In the same year, he joined the Heat and Mass Transfer Lab (LTCM) at EPFL as a scientific collaborator. He conducted research in design, installation, and testing of a novel, completely passive, cooling system for a transistor module. He has authored more than 10 scientific publications and he serves as a reviewer for journals and conferences papers on the topics of energy conversion, heat transfer and thermal management.



John Richard Thome | john@thome@epfl.ch

John Richard Thome is currently Professor-Emeritus of Heat and Mass Transfer at the Swiss Federal Institute of Technology of Lausanne (EPFL), Switzerland, and he was Full Professor from 1998 to 2018. In 2014, he co-founded a consulting company, JJ Cooling Innovation Sàrl, in Lausanne. He is the author of five books and more than 250 journal papers on two-phase flow heat transfer and micro-two-phase cooling systems for electronics cooling. He received the Nusselt-Reynolds Prize in 2017, the ASME Journal of Heat Transfer Best Paper Award in 1998, the United Kingdom's Institute of Refrigeration J.E. Hall Gold Medal in 2008, the ASME Heat Transfer Memorial Award in 2010, the IEEE Richard Chu IThERM Award in 2019 and the ASME Allan Krause Thermal Packaging Medal at InterPACK 2019. He obtained his Ph.D. at Oxford University and he founded the Virtual International Research Institute of Two-Phase Flow and Heat Transfer to promote research collaborations and education.

INTRODUCTION

The world is becoming more digitalized than ever before. The workload of data centers has tripled since 2015 [1]. Despite huge progress in thermal management, traditional air-based cooling technology still represents a critical factor which significantly impacts data center operating costs and the environment. Depending on the size and operating conditions of a data center, a significant portion of the total energy consumption (up to 55%) is used to cool the servers. Therefore, the implementation of greener cooling technologies that can re-use the heat generated by the servers for other purposes (i.e. room heating, power generation, etc.) is becoming more and more attractive. The novel passive two-phase cooling technology, presented in this article, offers not only a very efficient way to manage the heat load of the servers, with a substantially higher heat flux limit versus traditional technology, but also offers a feasible and economically viable way to re-use that energy.

THERMAL AND FLUIDIC PHENOMENA IN THE OPERATION OF A SINGLE LOOP THERMOSYPHON

A single loop thermosyphon is composed of four elements:

1. **The evaporator:** where the absorbed latent heat changes the working fluid's phase from liquid to a liquid-vapor mixture
2. **The condenser:** where the latent heat rejection changes the vapor back to the liquid phase
3. **The riser:** which transports the liquid-vapor mixture upward from the evaporator to the condenser
4. **The downcomer:** which carries the liquid downward from the condenser to the evaporator

A schematic of a single loop thermosyphon is reported in *Figure 1*. The condenser must be placed above the evaporator to favor buoyantly driven passive flow circulation, and due, to the small channel sizes, slug and annular flows are the main flow patterns occurring during the operation of a thermosyphon [2, 3].

As general design guidelines for electronics cooling applications, it is important to ensure a subcooled liquid at the evaporator inlet and a sufficiently low vapor quality at the evaporator outlet to avoid four phenomena related to the two-phase flow in micro-channels and thermosyphons in particular:

- **Dry-out:** the vapor phase, with its poor heat transfer characteristics, may blanket the wall when the vapor quality approaches 1. Therefore, it is imperative to have a fully wetting flow at the evaporator outlet. Generally, the thermosyphon can safely operate with vapor quality in the range of between 0.1 and 0.5. Note: vapor quality is defined as the ratio between the mass of vapor flow divided by the total mass flow rate (liquid and vapor).
- **Instabilities:** a subcooled liquid at the evaporator inlet eliminates pressure-related instabilities in micro-channels and Ledinegg's instability in a thermosyphon loop [4].

- **Backflow:** at high heat loads, the rapid growth of vapor may push the flow backward, triggering flow instabilities and decreasing thermal performance. The subcooled liquid prevents this from occurring, but it must be coupled with careful design of the inlet manifold and flow distribution in the evaporator.
- **Gravity-driven flow:** a single loop thermosyphon has two working regimes. The gravity-dominant regime occurs when the buoyancy in the riser is the primary force, up to when the heat duty creates sufficient vapor quality to change to friction-dominant flow. A thermosyphon should be designed to operate in a gravity-dominant regime as the mass flow rate increases with the heat load, and the subcooled liquid at the evaporator inlet serves this purpose [5].

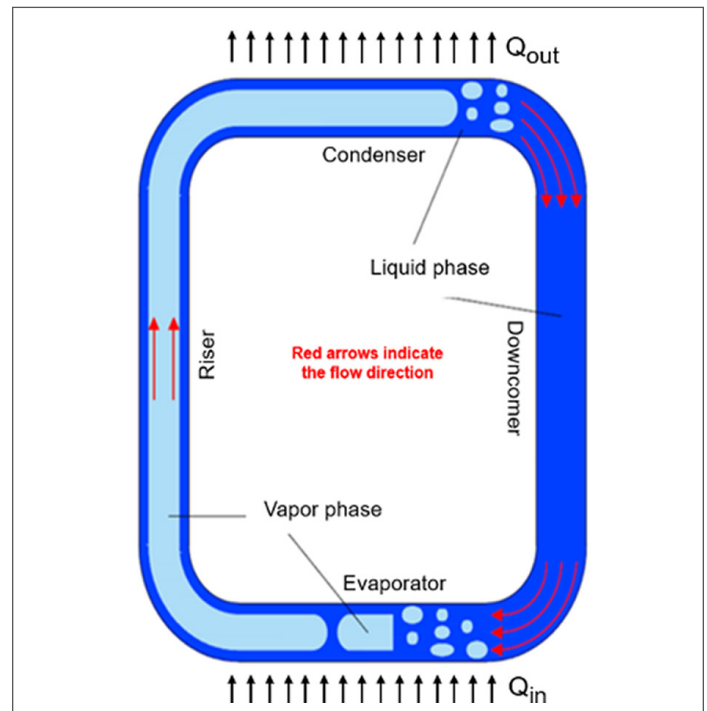


Figure 1: Schematic of a single loop thermosyphon indicating the main components and flow direction.

Subcooling at the inlet and the latent heat transfer both affect the thermal performance. They are related to the heat load through the energy balance on the working fluid:

$$Q = \dot{m} \left(c_p \cdot \Delta T_{sub} + \Delta h_{lv} \cdot x_{out} \right)$$

where Q (W) is the total heat load (comprised of subcooled and saturated heat loads), \dot{m} (kg/s) is the coolant mass flow rate, c_p (J/kg/K) is the specific heat at constant pressure, ΔT_{sub} (K) is the subcooling at the evaporator inlet, Δh_{lv} (J/kg) is the latent heat of vaporization, and x_{out} (-) is the outlet vapor quality. To minimize the total thermal resistance, the subcooled heat load needs to be minimized, while the saturated heat load needs to be maximized. Therefore, it is paramount to find the right trade-off together with the design guidelines reported above.

TEST RESULTS WITH A SINGLE LOOP THERMOSYPHON PROTOTYPE

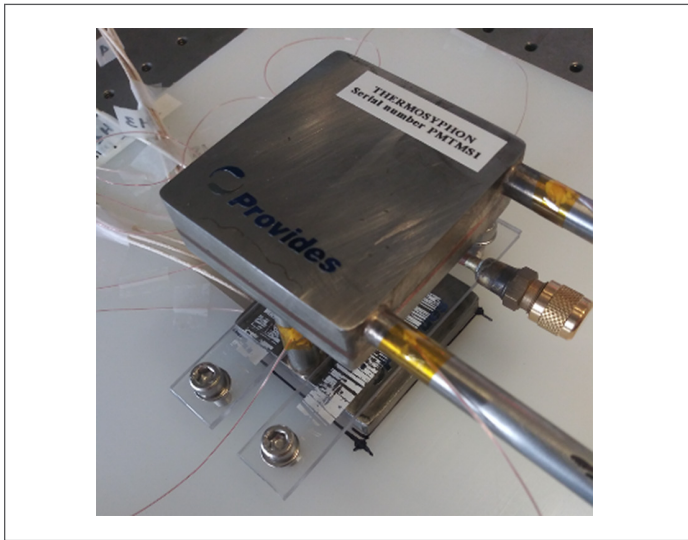


Figure 2: Experimental setup built at Nokia Bell Labs to characterize thermal performance of the thermosyphon operating with R1234ze. The heat was dissipated to a secondary side water cooling loop.

A newly designed thermosyphon prototype suitable for server-level cooling is depicted in Figure 2; Figure 3 illustrates a schematic diagram including the main components and measurements. The main components of the test setup are the following:

- A low-height water-cooled thermosyphon designed for cooling 2-U servers. The evaporator was directly attached to the heat source via a highly conductive thermal grease (Thermal Grizzly Kryonaut: thermal resistance of 0.0032 K/W and thermal conductivity of 12.5 W/m/K)
- A pseudo-chip with a footprint area of 4 x 4 cm² designed with four cartridge heaters in parallel, that were located in a copper block. Four calibrated K-type thermocouples (accuracy of ± 0.25 °C) were used to measure the mean heater temperature. The junction (evaporator base) temperature was evaluated from the mean heater temperature and a 1D heat conduction calculation accounted for the thermal resistance through the copper and thermal interface material. Another K-type thermocouple was attached on the adiabatic section of the riser to measure the saturation temperature
- A thermal bath circulated cold water at a given temperature and flow rate on the secondary side of the thermosyphon. Its flow rate was indirectly determined from an energy balance using the water's temperature rise, with K-type thermocouples attached on the inlet and outlet tubes, and imposed heat load, assuming negligible heat loss to the ambient
- A customized charging station (not shown here) was designed and fabricated to fill the thermosyphon with R1234ze up to the desired charge
- An electrical circuit (a power supply, four cartridge heaters and a shunt resistor) were used to power the pseudo-chip and to accurately measure the heat delivered to the refriger-

ant flow (maximum value of 333 W, but thermosyphon tests were executed up to about 200 W)

- A data acquisition system was coupled to LabView to control the operating conditions, monitor the thermal performance over time, and record the measured parameters (i.e. temperatures, power, etc.), which were post-processed separately

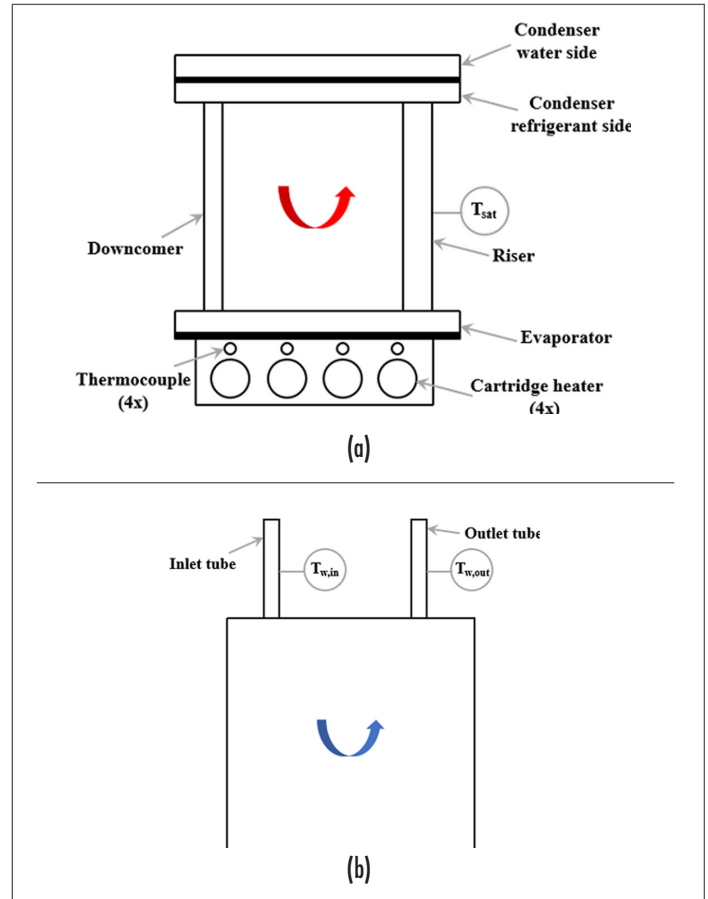


Figure 3: Schematic diagram of the thermosyphon: (a) front view, where the red arrow indicate the refrigerant flow direction; (b) top view showing the condenser secondary side and water flow direction.

Table 1 reports the external dimensions of the thermosyphon (the internal features are confidential).

| 1: Dimensions of the thermosyphon | |
|------------------------------------|----------------------|
| Parameter | Value |
| Evaporator length, width and depth | 60 x 60 x 9.50 (mm) |
| Riser height | 42 (mm) |
| Riser external diameter | 10 (mm) |
| Condenser length, width and depth | 60 x 60 x 18.50 (mm) |
| Downcomer height | 42 (mm) |
| Downcomer external diameter | 8 (mm) |
| Total thermosyphon height | 70 (mm) |

The cooling capabilities of the server-level thermosyphon were evaluated under transient and steady-state conditions. In particular, the

results presented in this section refer to a secondary side water mass flow rate in the condenser of 364 kg/h and water inlet temperature of 15°C and a maximum heat load of 200 W (corresponding to a footprint heat flux of 16.3 W/cm²) using the refrigerant R1234ze as the working fluid. This is a very promising refrigerant for electronics cooling applications due to its negligible environmental impact (i.e. Global Warming Potential is less than 1) [6].

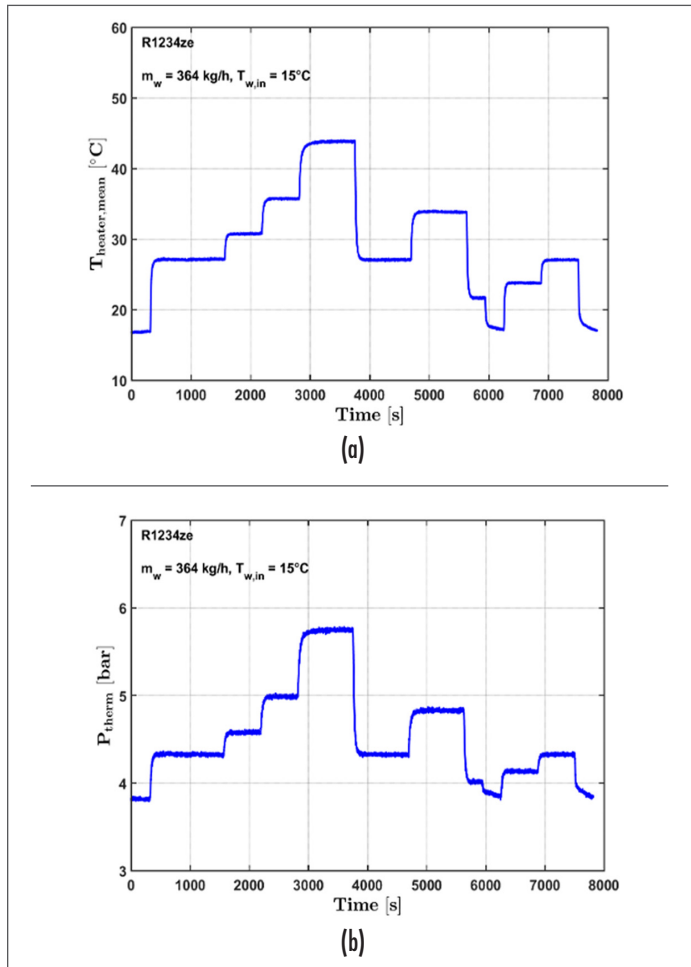


Figure 4: Proof-of-concept experiment over two hours with step changes in heat load from 50 W to 200 W: (a) mean heater temperature of four temperature measurements inside the copper block (one per heater); (b) thermosyphon internal pressure over time calculated from the saturation temperature.

Figures 4(a) and 4(b) depict the server-level thermosyphon thermal performance with a maximum heater temperature of 46°C at the maximum power of 200 W, while the corresponding system pressure was measured to be only 5.8 bar. No temperature overshoots or pressure fluctuations were observed, meaning that the thermosyphon offered stable cooling over a wide range of changing heat loads. Also, rapid thermal responses and smooth transients were observed during the start-up operations at the times of 300 s (0-100 W) and 6,300 s (0-70 W). This is due to the fact that passive two-phase flow instabilities were minimized by ensuring the right level of liquid in the downcomer in order to prevent condenser flooding and to balance the total pressure drop in

the loop (the latter was important to avoid intermittent flow in the evaporator which may induce partial dry-out). The temperature and pressure measurements followed similar trends and they both increased with the heat load, due to the higher vapor formation rate in the closed system.

Figure 5 shows the total thermal resistance as a function of the heat load. Conduction thermal resistance played a negligible role in the heat transfer as the gravity-driven two-phase flow circulation was triggered at very low heat loads (3-5 W). Overall, the total thermal resistance decreased with increasing heat load due to the enhancement of the boiling process due to the higher refrigerant mass flow rate, vapor quality and heat flux. The change in the thermal resistance slope at about 30 W coincided with the enhanced heat transfer performance when changing from slug-plug flow to annular flow in the evaporator. The minimum value of thermal resistance was about 0.113 K/W when the heat load was 120 W.

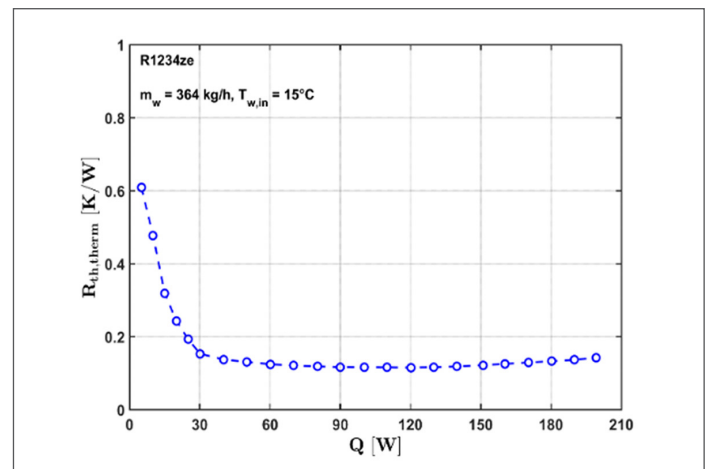


Figure 5: Total (thermosyphon) thermal resistance as a function of the heat load. This was evaluated as the ratio between the temperature difference between the junction to water-inlet divided by the imposed heat load.

CALCULATION OF WORKING FLUID'S MASS FLOW RATE

The thermosyphon's working fluid mass flow rate could not be directly obtained through single-phase pressure drop measurements [7] or energy balance calculations [8] due to the small form factor of the system. A commercial code [9, 10] was then used to estimate the thermosyphon mass flow rates. Specifically, the inputs needed to solve for the mass flow rates were the full geometry, fluids (R1234ze and water), operating conditions, and measured thermal resistance curve (see Figure 5). This in-house simulator has already been shown to be accurate in validations against many independent thermosyphon databases [8, 11-14].

Figure 6 depicts the simulated thermosyphon mass flow rates as a function of the heat load. As expected, the mass flow rate increased with the heat load due to the larger system driving force (buoyancy in the riser), which was able to overcome the total pressure drop in the thermosyphon (evaporator, riser, downcom-

er, and condenser). The server-level thermosyphon was seen to be operating in the desired gravity-dominant regime [5].

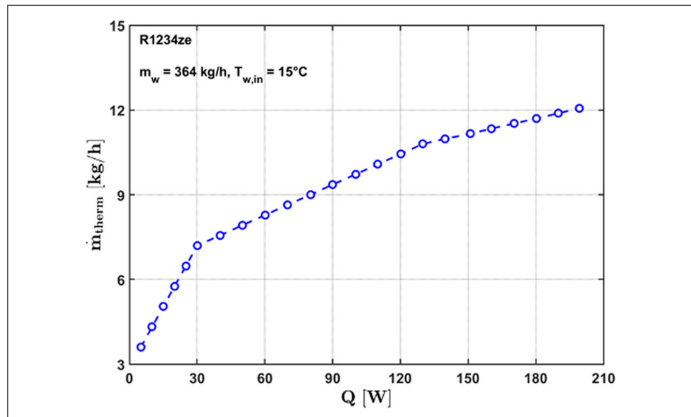


Figure 6: Predicted thermosyphon mass flow rate as a function of the heat load.

Figure 7 presents the corresponding outlet vapor quality as a function of the heat load, calculated through an energy balance across the evaporator under the assumption of negligible heat loss to ambient (reasonable as the thermosyphon is fully insulated). The highest exit vapor quality was 29%, which was well below the critical value of 55% at the onset of dry-out (based on the simulated threshold value from the code).

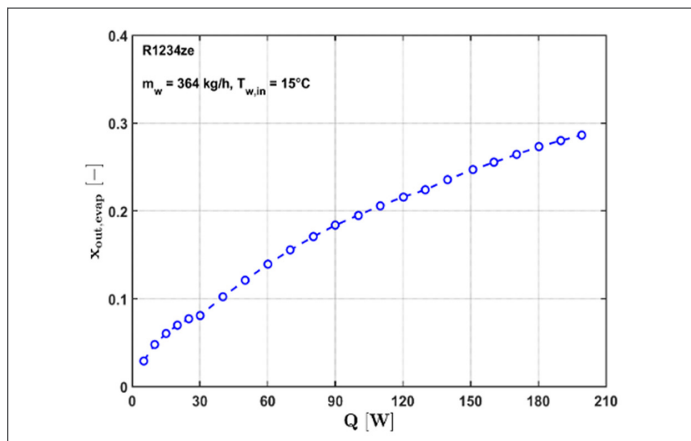


Figure 7: Evaporator outlet vapor quality as a function of the heat load.

TWO-PHASE COOLING IMPLEMENTATION

The envisioned cooling technology applied to an entire server rack is presented in Figure 8. In particular, this cooling technology operates with numerous server-level thermosyphons in order to dissipate the heat produced by the large heat sources (i.e. micro-processors, memories, etc.) into the two-phase micro-evaporators and out through the two-phase micro-condensers [8]. Then, the heat is transferred to rack-level thermosyphons designed with a common overhead compact condenser, which dissipates the total heat from the server rack (20-100 kW or more) into the data center's water cooling loop [15]. The low power components (i.e. motherboards, lighting, etc.) can be air-cooled and the warm air is rejected into the room.

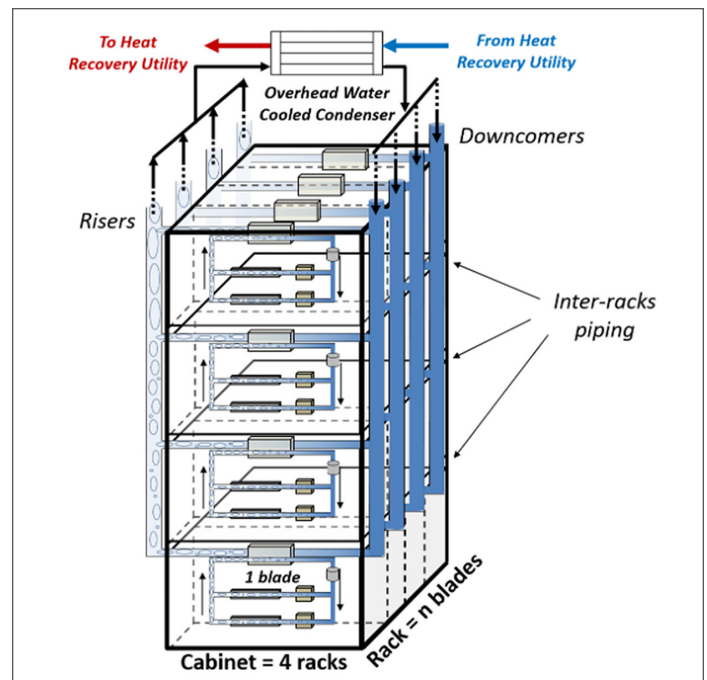


Figure 8: Concept of the proposed cooling technology for high power server racks [15]. The experimental results and thermal and fluidic phenomena in the operation of multiple thermosyphons in parallel (instabilities, flow regulation, etc.) are not addressed here as they represent the next step of this study.

This technology provides high thermal performance due to two-phase heat removal from server-to-rack-level, coupled with a significant energy savings (fewer server-level fans, air movers/blowers, and CRAC/CRAH units). In addition, thanks to the low overall thermal resistance, the secondary side water cooling loop can operate at relatively high temperatures, which makes this technology suitable for waste heat recovery (i.e. distribute to a district heating network or use to enhance the energy efficiency of a power plant [16]).

CONCLUSIONS

The present paper describes and presents test results for an innovative passive two-phase cooling technology for next-generation high-performance computers, which provides higher energy efficiency compared to air- and liquid-cooling technologies deployed today. The experimental study presented in this article was mainly focused on the thermal performance characterization of a low-height thermosyphon to be used in 2-U servers. Experimental results demonstrated very good heat transfer performance and stable cooling capabilities over a wide range of heat loads. The present cooling technology enables high heat transfer performance, low noise level, scalability towards higher heat dissipations and improved reliability while using an environmentally friendly refrigerant (R1234ze) as the working fluid.

ACKNOWLEDGEMENTS

This work is carried out as part of the Eurostars Project (PCOOL-DATA) that is co-funded by Eureka member countries and the Eu-

ropean Union Horizon 2020 Framework Programme, which are gratefully acknowledged for their support. Also, the authors would like to acknowledge Dr. Jackson Braz Marcinichen (JJ Cooling Innovation Sàrl) for contributing on the thermosyphon design and advising on the implementation of the proposed technology.

REFERENCES

1. J. Dulac, T. Abergel, C. Delmastro, Data centres and Data Transmission Networks. International Energy Agency report, online webpage: <https://www.iea.org/reports/tracking-buildings/data-centres-and-data-transmission-networks>, 2019.
2. C.L. Ong, J.R. Thome, Macro-to-microchannel transition in two-phase flow: part 1 - two-phase flow patterns and film thickness measurements. *Experimental Thermal and Fluid Science*, 2011.
3. J.W. Coleman, S. Garimella, Two-phase flow regimes in round, square and rectangular tubes during condensation of refrigerant R134a. *Internal Journal of Refrigeration*, 2003.
4. L.C. Ruspini, C.P. Marcel, A. Clausse, Two-phase flow instabilities: a review. *International Journal of Heat and Mass Transfer*, 2014.
5. H. Bielski, J. Mikielwicz, Natural circulation in single and two-phase thermosyphon loop with conventional tubes and minichannels. *Heat transfer-mathematical modeling, numerical methods and information technology*, 2011.
6. ESRL Chemical Sciences Division, Scientific assessment of ozone depletion: 2018. Online webpage: <https://www.esrl.noaa.gov/csd/assessments/ozone/2018/downloads/>, Ozone, 2018.
7. T. Salamon, R.L. Amalfi, N. Lamaison, J.B. Marcinichen, J.R. Thome, Two-Phase Liquid Cooling System for Electronics, Part 1: Pump-Driven Loop. *Intersociety Conference on Thermal and Thermomechanical Phenomena in Electronic Systems (ITHERM)*, 2017.
8. C.L. Ong, R.L. Amalfi, N. Lamaison, J.B. Marcinichen, J.R. Thome, Two-Phase Mini-Thermosyphon for Cooling of Datacenters: Experiments, Modeling and Simulations. *International Technical Conference and Exhibition on Packaging and Integration of Electronic and Photonic Microsystems (InterPACK)*, 2017.
9. J.B. Marcinichen, R.L. Amalfi, N. Lamaison, T. Salamon, J.R. Thome, Two-Phase Liquid Cooling System for Electronics, Part 4: Modeling and Simulations. *Intersociety Conference on Thermal and Thermomechanical Phenomena in Electronic Systems (ITHERM)*, 2017.
10. [N. Lamaison, C.L. Ong, J.B. Marcinichen, J.R. Thome, Two-Phase Mini-Thermosyphon Electronics Cooling: Dynamic Modeling, Experimental Validation and Application to 2U Servers. *Applied Thermal Engineering*, 2017.
11. [C.L. Ong, N. Lamaison, J.B. Marcinichen, J.R. Thome, Two-Phase Mini-Thermosyphon Electronics Cooling, Part 1: Experimental Investigation. *Intersociety Conference on Thermal and Thermomechanical Phenomena in Electronic Systems (ITHERM)*, 2016.
12. R.L. Amalfi, T. Salamon, N. Lamaison, J.B. Marcinichen, J.R. Thome, Two-Phase Liquid Cooling System for Electronics, Part 2: Air-Cooled Condenser. *Intersociety Conference on Thermal and Thermomechanical Phenomena in Electronic Systems (ITHERM)*, 2017.
13. R.L. Amalfi, T. Salamon, N. Lamaison, J.B. Marcinichen, J.R. Thome, Two-Phase Liquid Cooling System for Electronics, Part 3: Ultra-Compact Liquid-Cooled Condenser. *Intersociety Conference on Thermal and Thermomechanical Phenomena in Electronic Systems (ITHERM)*, 2017.
14. F. Cataldo, J.R. Thome, Experimental Evaluation of the Thermal Performances of a Thermosyphon Cooling System Rejecting Heat by Natural and Forced Convection. *Applied Thermal Engineering*, 2017.
15. R.L. Amalfi, F. Cataldo, J.R. Thome, An Optimization Algorithm to Design Compact Plate Heat Exchangers for Waste Heat Recovery Applications in High Power Datacenter Racks. *Intersociety Conference on Thermal and Thermomechanical Phenomena in Electronic Systems (ITHERM)*, 2019.
16. N. Lamaison, J.B. Marcinichen, J.R. Thome, Efficiency Improvements of a Thermal Power Plant by Making Use of the Waste Heat of Large Datacenters Using Two-Phase On-Chip Cooling. *Proceedings of the World Engineer's Convention*, 2011.

EPOXY for Chip Coating & Glob Top Applications

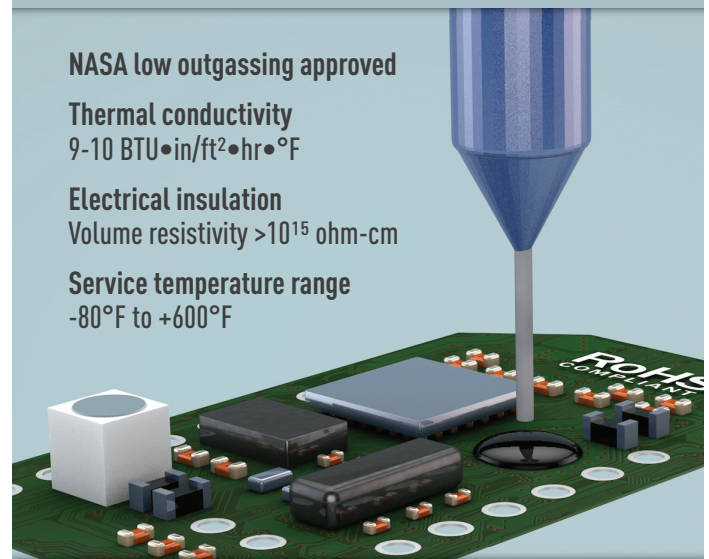
ONE PART ADHESIVE EP17HTND-CCM

NASA low outgassing approved

Thermal conductivity
9-10 BTU•in/ft²•hr•°F

Electrical insulation
Volume resistivity >10¹⁵ ohm-cm

Service temperature range
-80°F to +600°F



MASTERBOND[®]
ADHESIVES | SEALANTS | COATINGS

Hackensack, NJ 07601 USA • +1.201.343.8983 • main@masterbond.com

www.masterbond.com

Design Considerations When Using Heat Pipes

Reprinted from the *Electronics Cooling*® 2016, Fall Issue

George Meyer
Celsia, Inc.
gmeyer@celsiainc.com

INTRODUCTION

This article is intended to offer design guidance when using heat pipes for the most prevalent types of electronics applications: mobile to embedded computing and server type applications with power dissipation ranging from 15 W to 150 W using processor die sizes between 10 mm and 30 mm square. Discussion is constrained to those conditions as guidelines provided may not necessarily apply for power electronics applications. In addition, discussion is focused on the most ubiquitous type of heat pipe, i.e. copper tube with sintered copper wick using water as the working fluid. The article is also not intended to provide detailed analysis on the proper design of heat pipes and heat sinks, but rather to offer guidance on the number and size of heat pipes used as well as to provide guidance for estimating heat sink size and determining attachment methods of the heat sink to the printed circuit board (PCB). As this article does not review the fundamentals of heat pipe operation, for those readers not familiar with this technology good overviews can be found in [1-4].

As assistance, *Figure 1* serves to provide an overview of heat pipe construction and its principle of operation. A wick structure (sintered powder) is applied to the inside walls of the pipe. Liquid (usually water) is added to the device and vacuum sealed at which point the wick distributes the liquid throughout the device. As heat is applied to the evaporator area, liquid turns to vapor and moves to an area of lower pressure where it cools and returns to liquid form. Capillary action then redistributes it back to the evaporator section.



Figure 1: Heat pipe construction and principle of operation [1].

The application of heat pipes should be considered when the thermal design is either conduction limited or when non-thermal goals such as weight cannot be achieved with other materials such as solid aluminum and/or copper. The following factors need to

be considered when designing heat pipes into a thermal solution:

- Effective thermal conductivity
- Internal structure
- Physical characteristics
- Heat sink

and are discussed in the following sections.

1.0 EFFECTIVE THERMAL CONDUCTIVITY

Regularly published data for heat pipe thermal conductivity typically ranges from 10,000 to 100,000 W/m.K [4]. That is 250 to 500 times the thermal conductivity of solid copper and aluminum, respectively. However don't rely on those figures for typical electronics applications. Unlike solid metal, the effective thermal conductivity of copper heat pipes varies tremendously with heat pipe length, and to a lesser degree with other factors such as the size of the evaporator and condenser as well as the amount of power being transported.

Figure 2 illustrates the effect of length on heat pipe effective thermal conductivity. In this example, three heat pipes are used to transport heat from a 75 W power source. While thermal conductivity of 10,000 W/m.K is achieved at just under 100 mm heat pipe length, a 200 mm length has less than one-third the typically published maximum thermal conductivity of 100,000 W/m.K. As observed in the calculation for effective thermal conductivity in *Equation (1)*, the heat pipe effective length is a function of adiabatic, evaporator and condenser lengths:

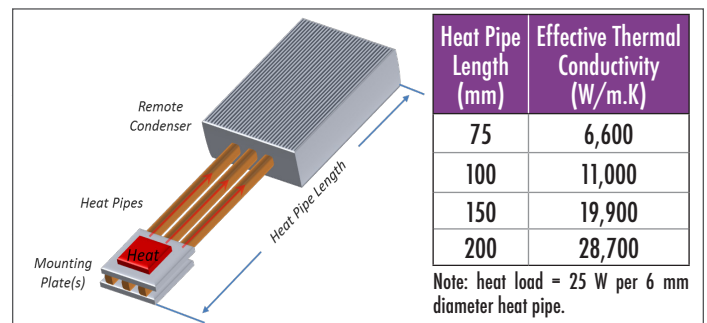


Figure 2: Measured heat pipe effective thermal conductivity as function of length.

2.0 INTERNAL STRUCTURE

Vendor specified heat pipe performance data are usually adequate for standard applications, but can be limited for specialized usage. Even when limiting the current discussion to copper/water/sintered wick versions, heat pipe customization can markedly affect operational and performance characteristics.

Changes to the internal structure of the heat pipe, most notably wick porosity and thickness, allow heat pipes to be tuned to meet specific operating parameters and performance characteristics. For instance, when a given diameter heat pipe is required to operate at higher power loads or against gravity, the capillary pressure in the wick needs to increase. For higher power handling capacities (Q_{max}), this means a larger pore radius. For effectively working against gravity (condenser below evaporator), this means a smaller pore radius and/or increased wick thickness. Additionally, it is possible to vary both wick thickness and porosity along the length of a single tube. Suppliers who specialize in heat pipe customization will regularly use custom formulated copper powders and/or unique mandrels to ensure the final product meets applications requirements.

3.0 PHYSICAL CHARACTERISTICS

With heat pipes, size generally matters most. However, changes to outward design will degrade performance for any given heat pipe, i.e. flattening and bending, in addition to the influence of gravity.

3.1 Flattening

Table 1 shows the Q_{max} for the most common heat pipe sizes as a function of diameter. As noted earlier, Q_{max} may vary amongst vendors for standard heat pipes. Therefore, in order to provide like-by-like comparison between the data presented in Table 1 it is taken from a project in which the author was involved.

Typically, sintered copper heat pipes can be flattened to a maximum of between 30% to 60% of their original diameter. Some may argue that it is the lower figure that is more realistic, before the centerline starts to collapse, but it's really a function of technique. For example, one-piece vapor chambers which begin life as a very large heat pipe can be flattened down to 90%. In this regard, the author would like to provide a rule of thumb for how much performance will degrade for every 10% decrease in thickness, but it would be irresponsible. Why? The answer comes down to how much excess vapor space is available before the heat pipe is flattened.

| Assessment Parameter | Diameter (mm) | | | | |
|--|---------------|------|------|------|-------|
| | 3 | 4 | 5 | 6 | 8** |
| Maximum power handling capacity (Q_{max})* [Watts] | 15.0 | 22.0 | 30.0 | 38.0 | 63 |
| Typical flattening height [mm] | 2.0 | 2.0 | 2.0 | 2.0 | 2.5 |
| Resulting width [mm] | 3.57 | 5.14 | 6.71 | 8.28 | 11.14 |
| Flattened maximum power* [Watts] | 10.5 | 18.0 | 25.5 | 33.0 | 52.0 |

Table 1: Heat pipe maximum power handling capacities as function of diameter.

Note: *Horizontal Operation, **A thicker wick is used compared to the 3 mm to 6 mm heat pipes.

Simply put, there are two performance limits important for terrestrial heat pipe applications: the wick limit and the vapor limit. The wick limit is the ability of the wick to transport water from the condenser back to the evaporator. As mentioned, the porosity and thickness of the wick can be tuned to specific applications, allowing for changes to Q_{max} and/or ability to work against gravity. The vapor limit for a particular application is driven by how much space is available for the vapor to move from the evaporator to the condenser.

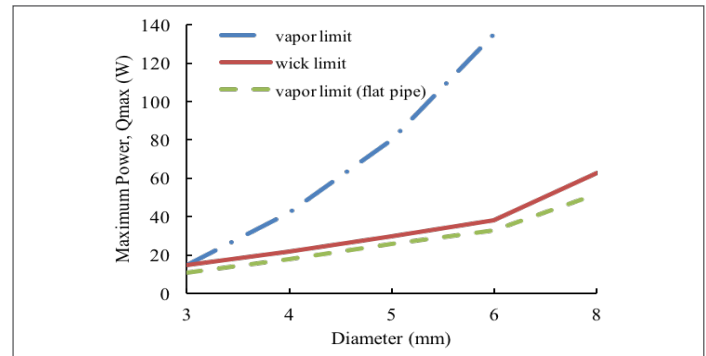


Figure 3: Measured heat pipe performance limits as a function of geometry, wick and vapor limits.

Note: Unless otherwise indicated heat pipe diameter is circular.

The wick (red) and vapor (blue) lines in Figure 3 plot the respective limits for the various heat pipe sizes shown in Table 1. It's the lesser of these two limits that determine Q_{max} and as shown the vapor limit is above the wick limit, albeit only slightly for the 3 mm heat pipe. As heat pipes are flattened, the cross sectional area available for vapor to move is gradually reduced, effectively moving the vapor limit down. So long as the vapor limit is above the wick limit, Q_{max} remains unchanged. In this example, we've chosen to flatten the heat pipes to the specifications in Table 1. As seen by the green line (vapor limit - flat pipe) in Figure 3, the vapor limit is below the wick limit, reducing the Q_{max} . Flattening the 3 mm by only 33% causes the vapor limit to become the determining factor whereas the 8 mm pipe needed to be flattened by over 60% for this to happen.

3.2 Bending

Bending the heat pipe will also affect the maximum power handling capacity, for which the following rules of thumb should be kept in mind. First, minimum bend radius is three times the diameter of the heat pipe. Second, every 45 degree bend will reduce Q_{max} by about 2.5%. From Table 1, an 8 mm heat pipe, when flattened to 2.5mm, has a Q_{max} of 52 W. Bending it 90 degrees would result in a further 5% reduction. The new Q_{max} would be $52 - 2.55 = 49.45$ W. Further information on the influence of bending on heat pipe performance is given in [5].

3.3 Working against gravity

Figure 4 illustrates how the relative position of evaporator to condenser can affect both Q_{max} and heat pipe selection. In each case, Q_{max} is reduced by approximately 95% from one orientation extreme to the next. In situations where the condenser must be

place below the evaporator, a sintered material is used to allow for smaller pore radius and/or increase the wick thickness. For instance, if an 8 mm heat pipe is optimized for use against gravity (-90°), its Q_{max} can be increased from 6 W to 25 W.

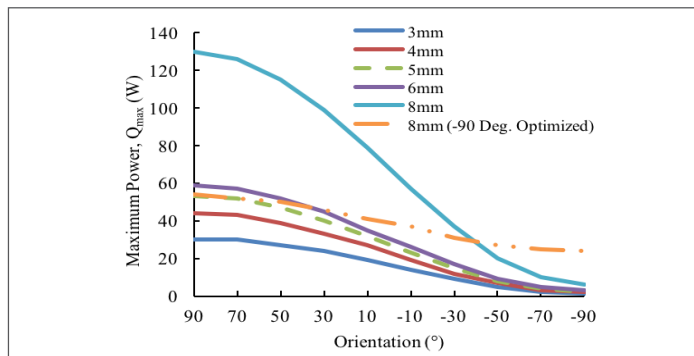


Figure 4: Measured effect of circular heat pipe performance as function of orientation and diameter.

Note: Evaporator above condenser = -90°

4. Heat Pipe Selection

The following example, summarized in *Table 2*, is presented to illustrate how heat pipes might be used to solve a thermal challenge for 70 W heat source with dimensions 20 mm x 20 mm and a single 90 degree heat pipe bend required to transport heat from evaporator to condenser. Furthermore, the heat pipes will operate in a horizontal position.

- To be at their most effective, heat pipes need to fully cover the heat source, which in this case is 20 mm wide. From *Table 1*, it appears that there are two choices: three round 6 mm pipes or two flattened 8 mm pipes. Remember the three 6 mm configuration will be placed in a mounting block with 1 to 2 mm between the heat pipes.
- Heat pipes can be used in conjunction to share the heat load. The 6 mm configuration has a Q_{max} of 114 W (3 x 38 W), while the flattened 8 mm configuration has a Q_{max} of 104 W (2 x 52 W).
- It's just good design practice to build in a safety margin, and it is suggested to typically use 75% of rated Q_{max} . Therefore select 85.5 W for the 6 mm (75% x 104 W) and 78 W for the 8 mm (75% x 104 W).
- Finally the influence of bending needs to be accounted for. A 90 degree bend will reduce Q_{max} of each configuration by another 5%. The resulting Q_{max} for the 6 mm configuration is therefore just over 81 W and for the 8 mm configuration it is 74 W, both of which are higher than the 70 W heat source that is to be cooled.

As can be seen from this analysis, both heat pipe configurations are adequate to transport heat from the evaporator to the condenser. So why choose one over the other? From a mechanical perspective it may simply come down to heat sink stack height at the evaporator, i.e. the 8 mm configuration has a lower profile than does the 6mm configuration. Conversely, condenser efficiency may be improved by having heat input in three locations versus

two locations, necessitating the use of the 6 mm configuration.

| Parameter | Configuration | |
|---------------------------------------|--|-----------------------------|
| | 6 mm circular | 8 mm flat |
| Heat pipe geometry | | |
| Required heat pipe bend | One 90° | One 90° |
| Number of heat pipes | Three round 6 mm | Two 8 mm flattened to 2.5mm |
| Heat pipe width as configured | 20mm = 18 mm + 2 x 1 mm gap in baseplate | 22.3 mm = 2 x 11.14 mm |
| Q_{max} per heat pipe as configured | 38 W | 52 W |
| Q_{max} as configured | 114 W | 104 W |
| 25% Q_{max} safety margin | 85.5 W | 78 W |
| Less 5% Q_{max} for bend | 81 W | 74 W |

Table 2: Heat pipe configuration options for a 20 mm x 20 mm heat source dissipating 70 W.

4.0 HEAT SINKS

There are numerous choices from zipper pack fins to extruded fin stacks, each with their own cost and performance characteristics. While heat sink choice can markedly affect heat dissipation performance, the biggest performance boost for any type of heat exchanger comes with forced convection. *Table 3* compares the benefits and pitfalls for range of heat sinks, some of which are illustrated in *Figure 5*.

| Heat Sink | Cost | Typical Benefits | Potential Pitfalls |
|--------------------------|----------|--|--|
| Extruded | \$ | <ul style="list-style-type: none"> Readily available Easy to manufacture to custom specifications, including grooves for heat pipes | <ul style="list-style-type: none"> Dimensions are limited Fin height limited ~20x fin width Base and fins are same material, usually aluminum |
| Die Cast | \$ | <ul style="list-style-type: none"> Net shape Low weight Easily customizable | <ul style="list-style-type: none"> Lower thermal conductivity Potential for porosity Not generally used with heat pipes |
| Bonded | \$\$ | <ul style="list-style-type: none"> Large heat sink sizes Base and fins can be of different materials | <ul style="list-style-type: none"> If fins are epoxied in place, added thermal resistance |
| Skived | \$\$ | <ul style="list-style-type: none"> Fin and base from solid piece of metal, usually copper High density fins possible More design flexibility than extrusion | <ul style="list-style-type: none"> Base may be thicker than needed, thus higher weight Fins damage easily |
| Fin Pack and Zipper Fins | \$\$ | <ul style="list-style-type: none"> Low-high fin density Low weight High design options, including center mounted heat pipes | <ul style="list-style-type: none"> Generally, for fins less than 1mm thick |
| Forged | \$\$\$ | <ul style="list-style-type: none"> Fin design in many shapes (pin, square, oval, etc.) | <ul style="list-style-type: none"> Usually reserved for higher volume products as tooling is expensive |
| Machined | \$\$\$\$ | <ul style="list-style-type: none"> High thermal conductivity Complicated designs OK | <ul style="list-style-type: none"> None, other can cost. Not good for high volume due to production time |

Table 3: Heat pipe selection considerations for a condenser heat sink.

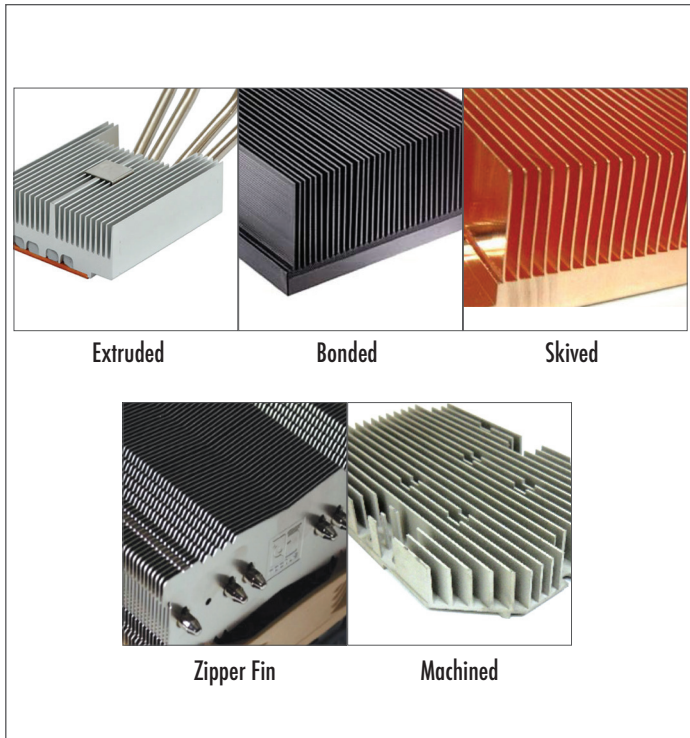


Figure 5: Heat sink designs whose characteristics are summarized in Table 3.

As a starting point for determining heat sink selection, Equation (2) can be used to estimate the required heat sink volume for a given application:

$$V = Q R_v / \Delta T \quad (2)$$

where: V = heat sink volume [cm^3], Q = heat to be dissipated [W], R_v = volumetric thermal resistance [$\text{cm}^3\text{-}^\circ\text{C}/\text{W}$], ΔT = maximum allowable temperature difference [$^\circ\text{C}$].

Table 4 provides guidance on the range of heat sink volumetric thermal resistances as a function of air flow conditions.

| Air Flow (m/s) | Volumetric Thermal Resistance ($\text{cm}^3\text{-}^\circ\text{C}/\text{W}$) |
|-----------------------------|--|
| Natural Convection | 500-800 |
| 1 m/s (gentle air flow) | 150-250 |
| 2.5 m/s (moderate air flow) | 80-150 |
| 5 m/s (high air flow) | 50-80 |

Table 4: Typical heat sink volumetric thermal resistance range as function of air flow conditions [6].

Whether dealing with a heat exchanger that is local or remote to the heat source, the options for mating heat pipes to them are identical and include grooved base, grooved mounting block, and direct contact methods as illustrated in Figure 6.

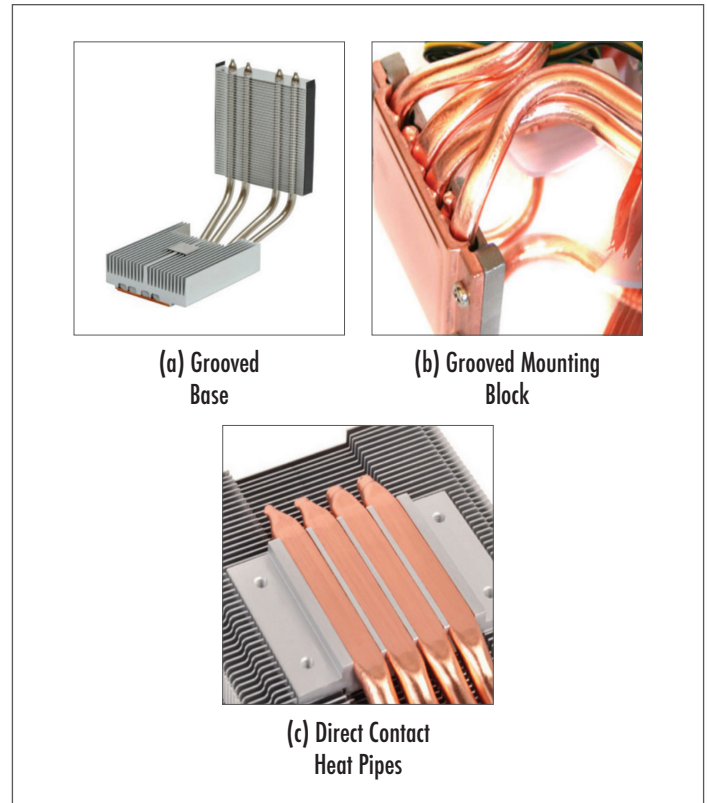


Figure 6: Heat pipe condenser mating.

It should go without saying that simply soldering a round pipe to a flat surface is far from optimal. Circular or semi-circular grooves should be extruded or machined into the heat sink. It's advisable to size the grooves about 0.1 mm larger than the diameter of the heat pipe in order to allow enough room for the solder.

The heat sink shown in Figure 6(a) uses both a local and remote heat sink. The extruded heat exchanger is designed to accommodate slightly flattened heat pipes, helping to maximize the contact between the copper mounting plate and the heat source. A remote stamped fin pack is used to further increase thermal performance. These types of heat exchanger are particularly useful because the pipes can run directly through the center of the stack, decreasing conduction loss across the fin length. Because no base plate is required with this fin type, weight and cost can be reduced. Again the holes through which the heat pipes are mounted should be 0.1 mm larger than the pipe diameter. Had the pipe been completely round at the heat source, a thicker grooved mounting plate would have been required as seen in Figure 6(b).

If conduction losses due to the base plate and extra TIM layer are still unacceptable, further flattening and machining of the heat pipes allows direct contact with the heat source as seen in Figure 6(c). Performance gains from this configuration usually lead to between a 2-8 $^\circ\text{C}$ reduction in temperature rise. In cases where direct contact of the heat source to the heat pipes is required a vapor chamber, which can also be mounted directly, should be considered due to its improved heat spreading capacity.

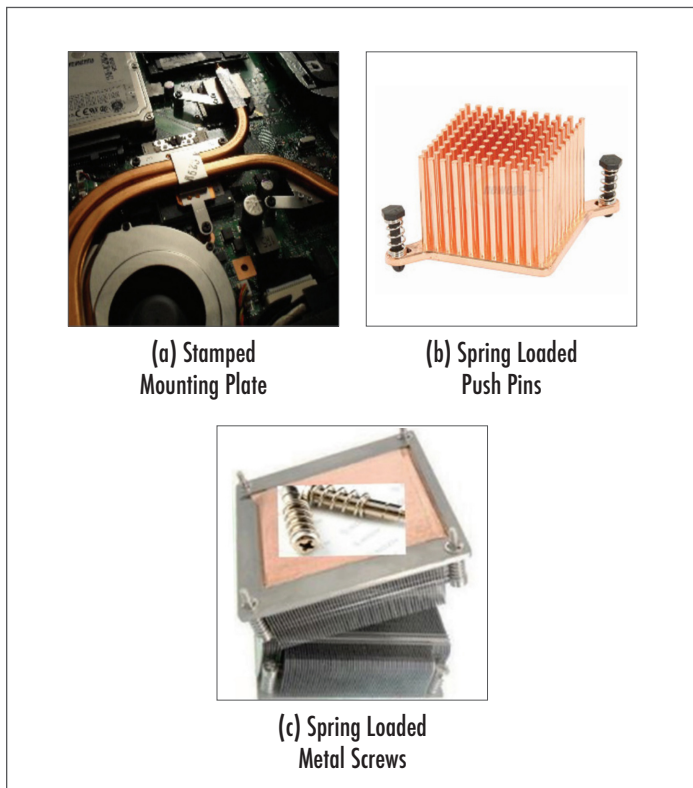


Figure 7. Heat pipe attachment methods for small (low mass) heat sinks.

The primary reason for considering a heat pipe solution is improved performance. As such, the use of thermal tape or epoxy as the primary means of attaching the heat sink to the die is not suitable. Instead three types of mechanical attachments are often used with heat pipes; all of which can meet MIL-810 and NEBS Level 3 shock and vibration requirements.

Finally, typical heat pipe attachment methods for small (low mass) heat sinks are shown in Figure 7. In Figure 7(a) a stamped

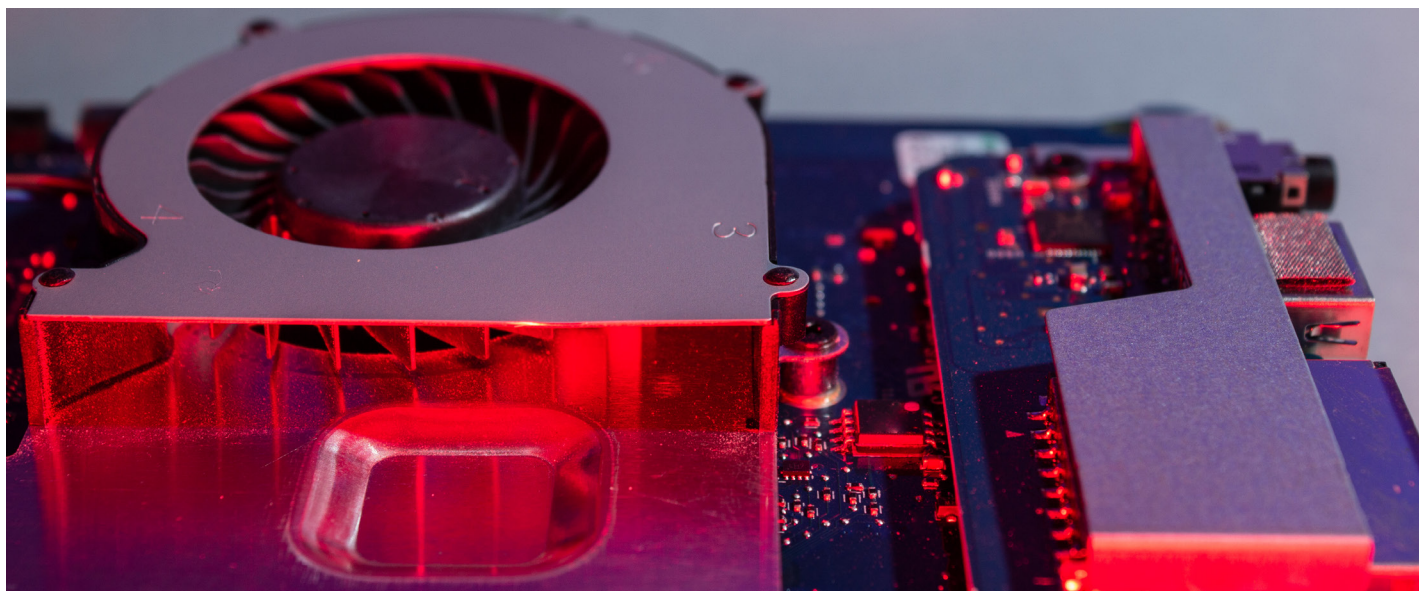
mounting plate is shown. Although it requires two PCB holes, this method offers better shock and vibration protection relative to thermal tape or epoxy, and some TIM compressions—with up to 35 Pa compression required. Figure 7(b) shows spring loaded plastic or steel push pins further increase TIM compression up to around 70 Pa. Installation is fast and simple but removal requires access to the back of the PCB. Push pins should not be considered for anything more than light duty shock and vibrate requirements. Spring loaded metal screws, Figure 7(c), offer the highest degree of shock and vibration protection as they are the most secure method of attaching a heat sink to the die and PCB. They offer the highest TIM preload at approximately (520 Pa).

SUMMARY

Design guidance was provided on the use copper tube heat pipes with sintered copper wick using water as the working fluid. As outlined, heat pipe selection needs to consider a range of factors including effective thermal conductivity, internal structure and physical characteristics, in addition to the heat sink characteristics.

REFERENCES

1. Garner, S.D., “Heat Pipes for Electronics Cooling Applications,” ElectronicsCooling, September 1996, <http://www.electronics-cooling.com/1996/09/heat-pipes-for-electronics-cooling-applications/>, accessed August 15, 2016.
2. Graebner, J.E., “Heat Pipe Fundamentals,” ElectronicsCooling, June 1999, <http://www.electronics-cooling.com/1999/05/heat-pipe-fundamentals/>, accessed August 15, 2016.
3. Zaghdoudi, M.C., “Use of Heat Pipe Cooling Systems in the Electronics Industry,” ElectronicsCooling, December 2004, <http://www.electronics-cooling.com/2004/11/use-of-heat-pipe-cooling-systems-in-the-electronics-industry/>, accessed August 15, 2016.
4. Peterson, G.P., An Introduction to Heat Pipes: Modeling, Testing and Applications, John Wiley & Sons, New York, US, (1994).

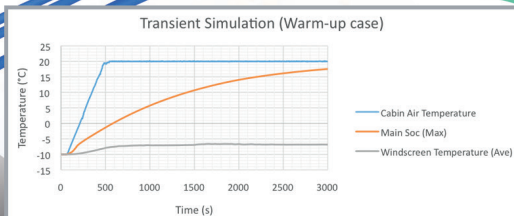


SIEMENS

Ingenuity for life

Simcenter Flotherm™ XT

- Discover a CAD-centric thermal simulation approach
- Compress the design process by bridging EDA & MCAD workflows
- Accurately model complex shaped geometry with robust automated meshing
- Automatically calibrate package thermal models for highest accuracy



Headset Comfort Assessment Through Thermal Analysis and IR Imaging

Rachel McAfee, Matt Harrison, Joshua Gess
Oregon State U.

| Nomenclature | |
|-----------------|---|
| q | heat loss (W) |
| h | heat transfer coefficient (W/(m ² ·K)) |
| A | area (m ²) |
| T | temperature (°C) |
| R _{ja} | junction-to-ambient resistance (K/W) |
| k | thermal conductivity (W/(m·K)) |
| L | characteristic length |
| μ | dynamic viscosity (kg/(m·s)) |
| g | gravity (m/s ²) |
| ν | kinematic viscosity (m ² /s) |
| β | volume of expansion coefficient (1/K) |

| Subscripts | |
|------------|-------------------|
| conv | convective |
| s | surface |
| i | region identifier |
| amb | ambient |

INTRODUCTION

Wearable technology is a growing market, projected to reach \$2.78 billion in revenue by 2024 [1], and comfort is a major factor driving sales for these devices. Ergonomics and ease of use were cited as major factors in the decision to purchase a virtual reality (VR) headset in a recent consumer survey [2]. While weight and form factor are certainly ergonomic factors to



Rachel McAfee

Rachel McAfee is an undergraduate Mechanical Engineering student at Oregon State University. She has completed internships with Intel’s development lab for High-Performance Computing and U.S. Army Research Laboratory. Her research is focused on electronics thermal management including two-dye laser-induced fluorescence measurements of fluidic systems. Rachel is the Chair of OSU Overclocking and Event Coordinator for Out in STEM.



Matt Harrison

Matt Harrison is a Ph.D. student in Mechanical Engineering at Oregon State University. He received a Bachelor of Science from Oklahoma State University in Mechanical Engineering in 2015. His work experience includes two years as a project engineer at Koch Industries, a research fellowship at Instituto Superior Technico in Lisbon Portugal, and an internship at Google. His research interests include electronics thermal management utilizing multiphase heat transfer, supercritical CO₂ cooling applications, synthetic jet characterization, and liquid nitrogen applications for competitive overclocking. Matt is slated to graduate in the summer of 2020.



Joshua Gess

Joshua Gess received his Ph.D. from Auburn University in Mechanical Engineering in 2015 and his B.S. in Mechanical Engineering from Vanderbilt University in 2005. Prior to receiving his Ph.D., he spent six years in the defense industry at Northrop Grumman in Madison, AL designing mobile command centers for Army, Navy, Marines, and National Guard customers. His research is focused on energy-dense electronics thermal management and fundamental multiphase heat transfer. He has developed a two-phase Particle Image Velocimetry (PIV) technique to calculate net coolant flow rates to boiling surfaces and built the first supercritical CO₂ cold plate for processor-scale cooling.

be considered, this study focuses on perspiration mitigation during prolonged use of a commercially available VR headset. The junction-to-ambient resistance, R_{ja} , of a commercially available headset was found to be 29.1 K/W at steady-state. However, a first-law analysis showed that 28.6% of the heat generated was being directed to the user's forehead. Thermocouples placed around the periphery of the headset showed an immediate temperature spike of 2.8°C when the headset was removed from the user after 2 hours of use. A maximum local temperature increase of 5.6°C was seen at the top of the headset directly above the device's microcontroller unit (MCU) [3]. From this data, the team hypothesized that more effective spreading of the heat away from the MCU would increase the available convective surface area, redirect heat away from the user's forehead to periphery areas around the headset, and improve user comfort during prolonged operation. The integration of a copper sheet bent to match the contour of the headset, shown as FN 2 in *Figure 1*, was shown to increase the effective surface area for convection by 61% and decrease the temperature directly above the MCU by 6.5°C [3].

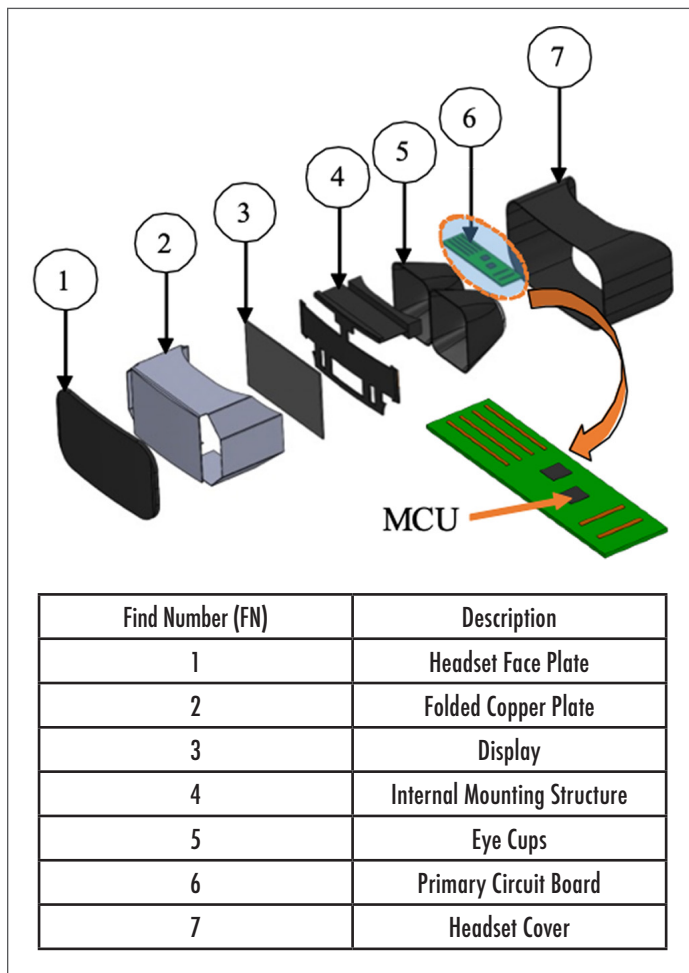


Figure 1: Exploded view of headset assembly with individual components identified as find numbers.

EXPERIMENTAL FACILITY, PROCEDURES, AND ANALYTICAL APPROACH

Six thermocouples were placed around the periphery of the head-

set as shown on *Figure 2*. These thermocouples were used to measure the surface temperature of the headset for subsequent convective heat loss analysis. It was assumed that each thermocouple temperature was reflective of the entire surface region upon which it was placed. For example, the measurement at thermocouple 5 on *Figure 2* was assumed to be the temperature of the entire faceplate, highlighted as yellow. The governing Nusselt number equations (*Equations 1-3*) corresponding to each region are shown in *Table 1*. Utilizing *Equation 4*, the corresponding heat transfer coefficient was used in Newton's Law of Cooling, *Equation 5*, to determine the convective heat loss from each region. The characteristic length, L_c , of each surface was found by dividing the surface area of each area of interest by its perimeter. The ambient temperature was measured with a thermocouple calibrated to a NIST-traceable thermistor accurate to within $\pm 0.2^\circ\text{C}$. All of the thermocouples used around the periphery of the headset were calibrated to the same thermistor.

In order to determine the heat loss from the headset, a first-law analysis was conducted, the individual losses calculated from *Equation 5* for each region were summed together. All relevant thermophysical properties used during calculations are shown in *Table 2*. The transient input power data was acquired from a USB-compatible measurement device [5]. The resulting power draw waveform can be described by a sinusoidal curve with a central tendency, or average power draw, of 3.52 W at a sampling frequency of 5 kHz with a standard deviation of 97 mW. The heat loss directed to the user is the difference between the convective heat transfer losses over Region 4, 5, and 6 (*Figure 2*), and the input power data. The OTS configuration had the heat leaving the MCU by natural convection only. When the spreader was added to the MCU a thin layer of thermal interface material epoxy ($k = 0.8 \sim 1.4 \text{ W/mK}$) was used to bond the spreader to the 400 micron thick copper spreader. From the spreader it was then allowed to naturally convect to the shell of the headset.

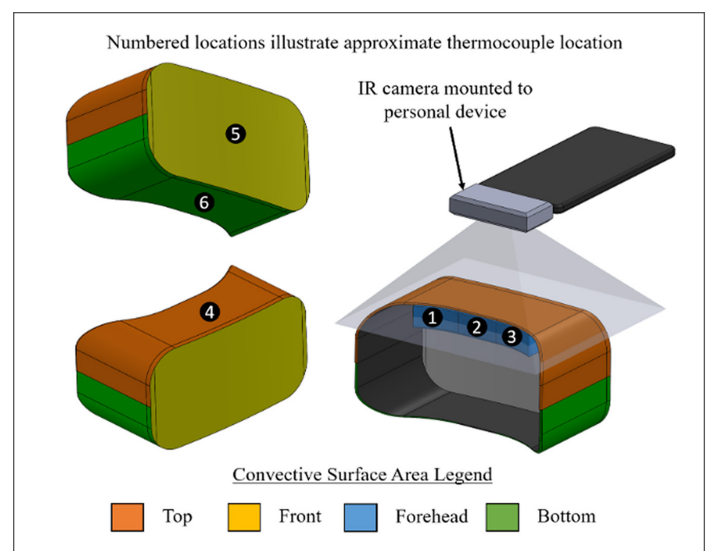


Figure 2: Data legend showing the area boundaries for convection heat transfer analysis and thermocouple placement for the results in this study

The test procedure was developed to simulate prolonged use at steady-state conditions. Eight participants were asked to play a game on the VR headset for 100 minutes. The system was removed and then powered off for a 20-minute cool down period. This test was conducted for two headset configurations: off-the-shelf (OTS) versus spreader integrated configuration. Tests were conducted in the same laboratory environment where the ambient temperature fluctuated by ± 0.3 °C. All users played the same game in an effort to control activity across participants to moderate levels. Users were then given a survey to ascertain the degree of perspiration, if any, was affected by the integration of the heat spreading thermal management approach. With this spreader in place, users reported a 25% reduction in perspiration during prolonged use [3].

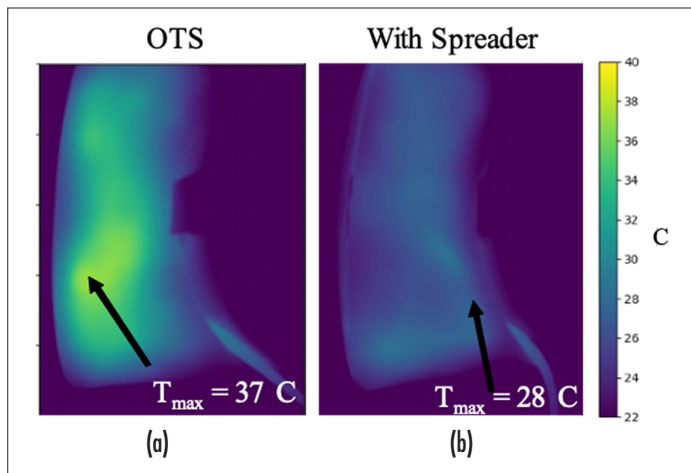


Figure 3 (a-b): Steady-state IR imaging of the headset in the OTS configuration (left: a) and with the internal heat spreader implemented (right: b). Central hot spot has been eliminated, maximum ΔT reduced by 9°C, and average surface temperature reduced by 6°C.

| Table 1: Governing equations for convective heat loss analysis.[4] | | | |
|--|--|-----------------|--|
| Figure 2 Region | Nusselt Relation Used | Equation Number | Description |
| Region 4 | $\overline{Nu}_L = 0.54Ra_L^{1/4}$ | (1) | Upward facing heated surface under laminar free convection |
| Region 5 | $\overline{Nu}_L = 0.68 + \frac{0.670Ra_L^{1/4}}{[1 + (\frac{0.492}{Pr})^{16}]^{4/9}}$ | (2) | Vertically oriented heated surface under laminar free convection |
| Region 6 | $\overline{Nu}_L = 0.52Ra_L^{1/5}$ | (3) | Downward facing heated surface under laminar free convection |
| All Regions | $h_i = \frac{\overline{Nu}_L k}{L_c}$ | (4) | Relation to get heat transfer coefficient from each regions Nusselt number |

$$q_{conv,i} = h_i A_{s,i} (T_{s,i} - T_{amb}) \quad (5)$$

Testing showed that the assumption of temperature uniformity on the top face, shown as Region 4 in Figure 2, needed to be corrected [3]. IR imaging was implemented using a cellular phone compatible camera oriented normal to the top face as shown in Figure 2 [6].

Figure 3a is an IR image of the headset with no internal heat spreading, while Figure 3b implements the copper spreader (FN 2, Figure 1). Figure 3a shows each headset at steady state with the VR on its home screen without attachment to a user. A central hot spot, which is approximately where the top thermocouple was placed (shown as thermocouple 4 on Figure 2), is visible on the OTS configuration IR image (Figure 3a). Implementation of the internal heat spreader shows a drastic reduction in surface temperature across the entire surface, as illustrated in Figure 3b. With the increased spatial resolution of the IR measurement approach, down to 70 microns for the field of view (FOV) used, these temperatures were used in an improved convective heat transfer analysis of losses through the top surface. The losses through the front and bottom faces were found to be relatively small [3]. Therefore, the improved IR temperature measurement method was only applied to the top surface where the largest in-plane temperature gradients were observed. The first law analysis used the average of all the temperatures measured in the FOV of the IR Imager as the top surface temperature. The thermocouple measurements at locations 5 and 6, illustrated on Figure 2, were used as the surface temperature for the faceplate and bottom surface, respectively. The transient power measurement device was still used for the total input power to the control volume.

| Table 2: Properties and Constants used during calculations | | |
|--|----------|-------------------|
| Property | Value | Units |
| μ | 1.85E-05 | kg/(m·s) |
| k | 0.026 | W/(m·K) |
| g | 9.81 | m/s ² |
| ν | 1.65E-05 | m ² /s |
| β | 3.18E-03 | 1/K |

RESULTS AND DISCUSSION

Transient temperature data and convective heat losses for the top surface are shown in Figure 4 and Figure 5, respectively.

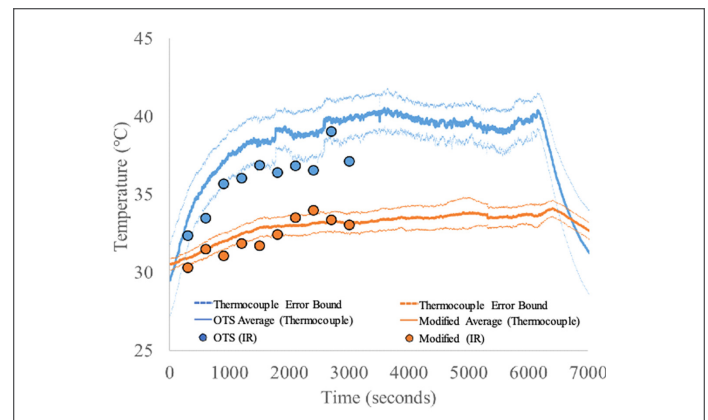


Figure 4: Transient temperature data for the OTS and modified head set configurations taken with a top surface thermocouple located centrally above the MCU and as an average of IR measurements spanning the entire top surface. Average Power 3.52 Watts.

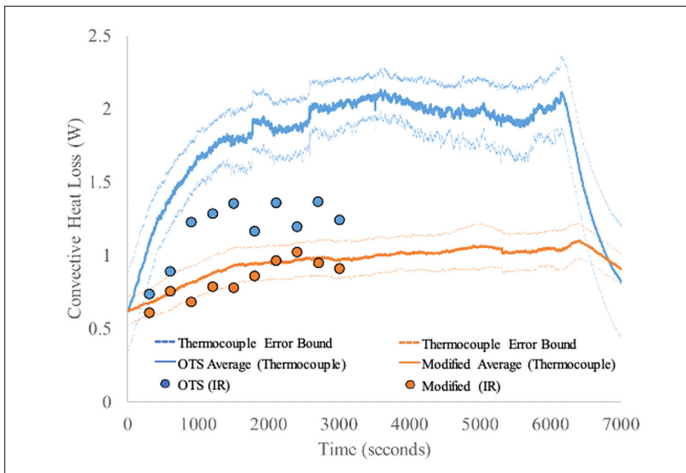


Figure 5: Transient convective heat loss data from the top surface for both headset configurations analyzed with thermocouple data and IR imaging. Average Power 3.52 Watts.

The solid lines of *Figure 4* and *Figure 5* are measurements and calculations made with the thermocouple placed on the top surface as shown in *Figure 2*. The dashed lines above and below the solid lines represent the range of values from measurement error, accounting for inherent instrument error and random error from the transient data of all eight participants. The solid dots of *Figure 4* and *Figure 5* are the results of measurements and calculations made with the IR camera positioned above the top face as shown in *Figure 2*. The color indicates the OTS versus integrated spreader headset, blue and orange respectively. Once steady state is reached, there is an approximate 6.5°C difference in the average top surface temperature recorded with the thermocouples between the OTS and modified configurations. Using IR measurements, this difference drops to approximately 3.3°C as the colder regions of the OTS headset are more accurately accounted for with this measurement technique.

In both instances, however, the top surface temperature drops dramatically with the integration of the internal heat spreader, a conclusion corroborated qualitatively with the difference in steady-state IR images provided in *Figure 3*. With the heat spreader integrated, the IR measurements fall within the error band for the thermocouple-based temperature measurements, while they do not for the OTS configuration. The accuracy of the thermocouple-based measurement for the integrated heat spreader solution is an artifact of the temperature being distributed more uniformly, which presents more isothermal conditions than the OTS configuration. The need for more spatially resolved IR measurements for the assessment of wearable technology is more evident in the convective heat loss data shown in *Figure 5*.

The measurement with the IR camera falls well outside the error band for the OTS configuration when assessed with locally placed thermocouples. To further corroborate the two measurement techniques, the temperatures measured with IR at the location of the top surface thermocouple were compared. The temperatures

recorded at the thermocouple location were within 0.05°C and 0.70°C when compared with the IR imaging for the modified and OTS configurations, respectively. Natural logarithmic analysis of the transient data leading up to steady state was used to determine the effective thermal time constant for both configurations. Introduction of the internal heat spreader increases the time constant by one order of magnitude from the OTS configuration value of 320 seconds.

The transient IR images shown in *Figure 6* for both the OTS and modified configurations illustrate how the heat spreads differently between the two designs. For the OTS configuration, there is a bottleneck to heat transfer located centrally around the MCU. However, the heat spreader serves to distribute the heat more uniformly, relieving much of the temperature rise above the MCU. This bottleneck creates an average four degree increase in the overall ΔT across the surface. Heat clearly reaches the top surface more effectively with the internal heat spreader integrated.

THERMAL MANAGEMENT SOLUTIONS

ThermaBridge™

Electrically Isolated A/CN Thermal Management Device

- ✓ High thermal conductivity
- ✓ Multiple sizes and thicknesses
- ✓ Electrically isolated thermal connection
- ✓ Optimal control over board temperature

- ✓ RoHS PtAg or solder coated
- ✓ PtAg terminals for easy attachment
- ✓ Protecting neighboring components
- ✓ Multiple sizes and thicknesses

With the ThermaBridge™

Without the ThermaBridge™

28%
Temperature
Reduction

Actual test of the ThermaBridge™ showing a heat generating component mounted on an FR4 board.

Contact IMS about our Custom Capabilities!

International Manufacturing Services, Inc.
www.ims-resistors.com | 401.683.9700

Without a more accurate representation of the temperature distribution around these side and bottom faces, it is currently impossible to accurately quantify the amount of heat loss being directed at the user's forehead. There are innovative solutions to measuring the amount of perspiration, motivated primarily by the exercise science/kinesiology community, which may be used to validate the analytical assessment of the heat transfer deficit being inflicted on the user during prolonged play [7].

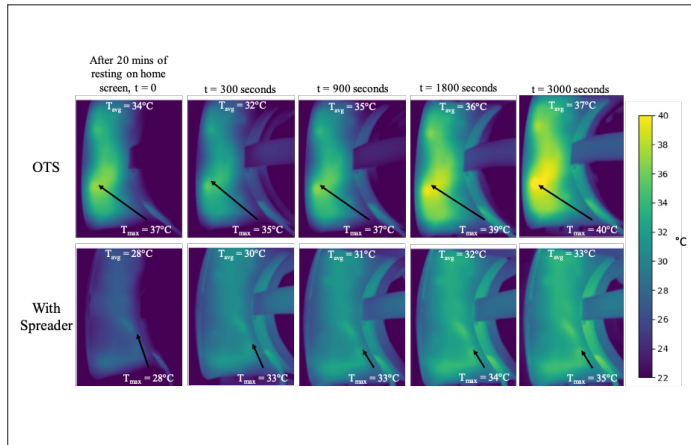


Figure 6: Progression of transient IR images taken during headset operation. Maximum temperature of the surface indicated by the arrow and average surface temperature reported on top of each image.

CONCLUSION

IR imaging showed that heat generated from the headset MCU can be more effectively spread throughout the headset with relatively simple modifications, resulting in an overall more comfortable user experience. Though in moderate use, approximated

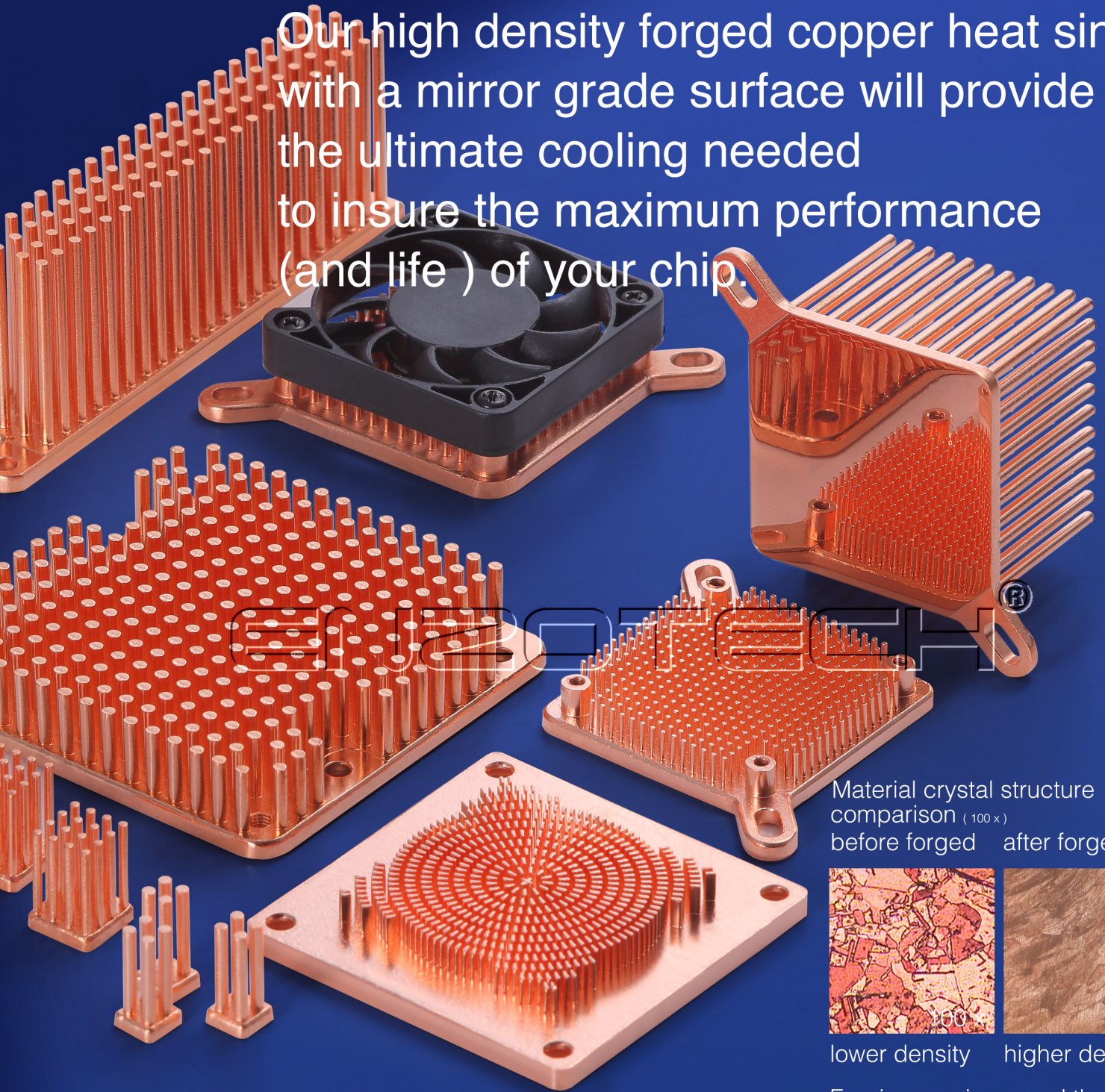
as 20 minutes or less by the data collected, a user may not feel an uncomfortable amount of perspiration/fatigue. However, for prolonged use in VR training for plant operators, military personnel, and athletic training, the addition of such a spreader would result in more comfortable training sessions for the user, enabling this technology to make inroads in low-risk virtual training/activity environments.

REFERENCES:

1. IMARC Group, 2019, "Industrial Wearable Devices Market: Global Industry Trends, Share, Size, Growth, Opportunity and Forecast." Available: <https://www.imarcgroup.com/industrial-wearable-devices-market>
2. International Data Corporation, 2018, "VR Headset Market Rebounds as Standalone Products Gain Traction while AR Headset Market also saw Positive Movement," Available: <https://www.idc.com/getdoc.jsp?containerId=prUS44509518>
3. R. McAfee, C. Haxton, M. Harrison, and J. Gess, 2020, "Thermal Characterization of a Virtual Reality Headset during Transient and Resting Operation" in Proc. of Semiconductor Thermal Measurement and Management Symposium (SEMI-THERM), San Jose, CA.
4. Bergman, T. L., Lavine, A. S., Incropera, F. P., & DeWitt, D. P. (2011). Fundamentals of heat and mass transfer. Hoboken, NJ: Wiley.
5. Monsoon Solutions High Voltage Power Monitor (Part Number: AAA10F)
6. Flir One Pro, <https://www.flir.com/products/flir-one-pro/>
7. Gao, W., Emaminejad, S., Nyein, H. et al. Fully integrated wearable sensor arrays for multiplexed in situ perspiration analysis. Nature 529, 509–514 (2016). <https://doi.org/10.1038/nature16521>

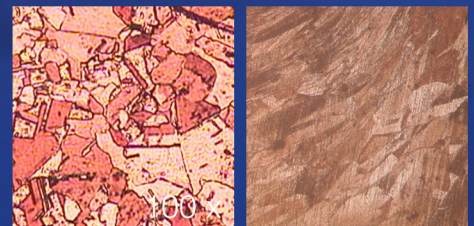


Our high density forged copper heat sink with a mirror grade surface will provide the ultimate cooling needed to insure the maximum performance (and life) of your chip.



ENZOTECH

Material crystal structure comparison (100 x)
 before forged after forged



lower density higher density

Forging can improved thermal conductivity 5-10% on average

ENZOTECHNOLOGY CORP.

Address : 14776 Yorba Ct. Chino, CA 91710 USA

Tel : 909-993-5140

Fax : 909-993-5141

E-mail : info@enzotechnology.com

Website : www.enzotechnology.com

Increased System Performance in Mobile Electronics Using High Performance Insulation-Graphite Composites

Due to the COVID-19 pandemic, several industry conferences and shows have been cancelled or postponed, therefore, Electronics Cooling is featuring this section to highlight research that has lost the ability to be presented.

Mitchell Warren¹, Julian Norley², John Allen¹, Jonathan Taylor², Lindsey Keen¹

¹ W. L. Gore & Associates
201 Airport Rd, Elkton MD, 21921 USA
mwarren@wlgore.com
jallen@wlgore.com
lkeen@wlgore.com

² NeoGraf Solutions, LLC
11709 Madison Ave.,
Lakewood, Ohio 44133 USA
jnorley@neograf.com
jtaylor@neograf.com

ABSTRACT

Graphite foils with ultra-high spreading capacity and insulation sheets with ultra-low thermal conductivity were combined in a thermally stressed Google Pixel 3XL (Pixel) to significantly increase steady-state system performance, while maintaining safe device touch (skin) temperatures (T_s), as compared to the out-of-the-box device configuration. Four unique thermal solutions of comparable thickness (~350 μm) were fabricated and subjected to thermal stress testing in the Pixel via *3DMark—Sling Shot Extreme*. Steady-state touch temperatures were reduced by up to 3.2°C with <1°C increase in max junction temperature (T_j) as compared to single-component thermal solutions of graphite, insulation, and air. The composite yielding the greatest T_s reduction was utilized to demonstrate an increase in steady-state system performance, while maintaining a surface temperature suitable for user safety. The steady-state *3DMark—Sling Shot Extreme* benchmark score increased from 3,401 to 3,823 resulting in a 12.4% increase in steady-state system performance.

The enhanced device performance was linked with material properties by means of steady-state heat flow and thickness testing for through-plane thermal conductivity of insulation, and thermal diffusivity testing for in-plane thermal conductivity of graphite.

KEYWORDS

Graphite, ultra-high spreading capacity, insulation, ultra-low thermal conductivity, composite, heat spreader, thermal conductivity, thickness, surface touch (skin) temperature, hot spot, junction temperature, ambient temperature, steady-state, Google Pixel 3XL (Pixel), system on chip (SoC), *3DMark—Sling Shot Extreme*, benchmark score, system performance, user safety.

NOMENCLATURE

| | |
|--------------------|--|
| k | thermal conductivity (W/m·K) |
| t | thickness (mm, μm) |
| TS | surface touch (skin) temperature (K, °C) |
| T_j | device junction temperature (K, °C) |
| ΔT | change in temperature (K, °C) |
| q'' | heat flux (W/m ²) |
| R'' | thermal resistance (K·m ² /W) |
| $t \cdot \Delta T$ | intrinsic heat spreading capacity ($\mu\text{m} \cdot \text{K}$) |

INTRODUCTION

Thermal spreaders (graphite) and insulators (air, polymers) have been widely and commonly used to address heat challenges in the mobile electronics industry. As the trends for higher power processing and thinner form devices become standard requirements, mobile electronics continue to face a more pressing issue of user safety by means of the surface touch (skin) temperature (T_s).

The Underwriters Laboratories (UL) guidance for T_s is based on direct skin contact for specific temperatures and durations, [1] and is accepted across the mobile electronics industry. Where passive thermal solutions have previously been able to reduce the TS below specification, many of the commonplace materials such as air and synthetic graphite are facing technical limitations [2]. In the absence of a thermal solution that maintains system performance, one widely practiced solution is power throttling of the processor, which may reduce system power by up to 50% [3].

In thin mobile electronics with relatively low temperatures (<100°C) and no active cooling, conduction is the primary mode of heat transfer inside the device [4]; internal convection and radiation are considered negligible in comparison and not discussed further in this work.

Fourier’s Law of One-Dimensional Conduction Heat Transfer, shown in Equation (1), states that the theoretical change in temperature (ΔT) is directly proportional to the thermal resistance (R'') of the heat transfer medium.

$$q'' = \frac{\Delta T}{R''} \left(\frac{W}{m^2} \right) \quad (1)$$

Assuming heat flux (q'') in a given system is constant, ΔT is driven by R'' , which is defined as the ratio of thickness (t) to conductivity (k).

$$R'' = \frac{t}{k} \left(\frac{K \cdot m^2}{W} \right) \quad (2)$$

Combining and rearranging Equations (1) and (2), TS can be viewed as a function of the junction temperature (T_j), t , k , and q'' , which is shown in Equation (3) and the accompanying one-dimensional resistance network (Figure 1). In a constrained system with constant q'' and t , T_s can be reduced by lowering k .

$$T_s = T_j - \frac{q'' \cdot t}{k} \quad (K, ^\circ C) \quad (3)$$

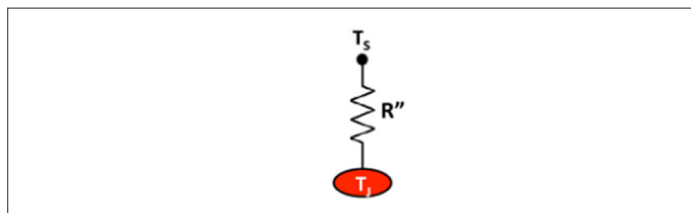


Figure 1: 1D thermal resistance network. Heat flows from T_j to T_s through R''

When a system is expanded into three dimensions of heat transfer (Figure 2), planar heat spreading can be an integral contributor to

the resulting TS. Both in-plane and through-plane conductivities deliver significant contributions to the resultant spreading of heat in a material of given thickness and area. Combining ultra-low (through-plane) conductivity insulation with ultra-high spreading capacity graphite yields a thermal composite solution with exceptional heat spreading performance compared to existing materials used for thermal management in thin mobile electronics.

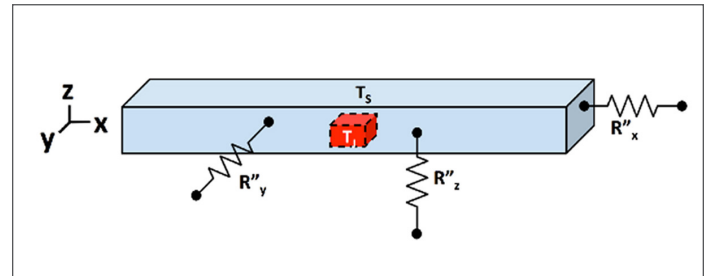


Figure 2: 3D thermal resistance network. Heat moves from T_j (center of device) in multiple directions including toward the surface of interest, T_s .

MATERIAL SELECTION

GORE® thermal insulation (W. L. Gore & Associates, Inc.) is an insulating material (“the insulation”) exhibiting ultra-low thermal conductivity, below that of air, in thin sheet form (100 μm and 250 μm). NeoNxGen™ thermal management solutions (NeoGraf Solutions, LLC) includes a thick foil graphite (70 μm to 270 μm) displaying ultra-high intrinsic heat spreading capacity (“high-performance thick graphite”).

Individual layers of insulation and graphite may separately provide a reduction in TS when placed between a heat source and the surface of interest. Insulation alone is an optimal solution when the ratio of available area to area of the surface hot spot is approximately one-to-one. While insulation is relatively isotropic, graphite exhibits highly anisotropic behavior, favoring thermal conduction in the plane of the material. This utility becomes impactful for TS reduction when the ratio of available area to area of the surface hot spot approaches two-to-one or greater; in these system architectures,

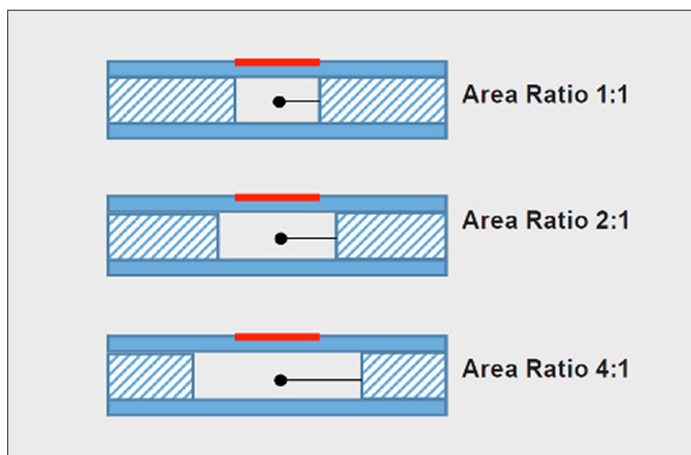
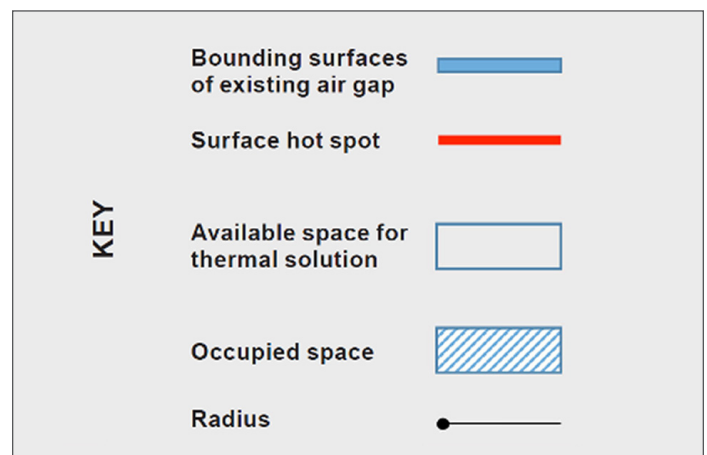


Figure 3: Schematic showing a cross section view of the ratio of available area to area of the surface hot spot. Area is proportional to radius squared.



insulation can be combined with graphite to enhance its effective heat spreading capacity. A schematic of the ratio of available area to area of the surface hot spot is illustrated in *Figure 3*.

INSULATION THERMAL CONDUCTIVITY CHARACTERIZATION

The insulation is characterized by its distinctively low thermal conductivity, <0.020 W/m·K, due to a conduction heat transfer phenomenon known as the Knudsen Effect. The Knudsen Effect explains that when the pore diameter in a medium is smaller than the mean free path of air (approximately 70 nm), the path of heat transfer through this medium is disrupted, relative to the path of heat transfer through air in free space [5]. This principle is often applied through the use of aerogels due to their morphology of high porosity with small pore diameters. The uniqueness of this insulation appears in the form of a homogeneous aerogel structure with ultra-low (and consistent) thermal conductivity and precise thickness resulting in a reliably high thermal resistance. Comparatively, the thermal conductivity of free air at room temperature is 0.026 W/m·K and it increases non-linearly with temperature (0.028 W/m·K at 50 °C), [6] which can result in variable and insufficient thermal resistance at elevated temperatures (>50 °C) in mobile electronics.

The through-plane thermal conductivity of this insulation is determined by measuring thermal resistance using a heat flow method (TA-Fox 50) and material thickness method (Instron-5565), following guidance from ASTM C518-17 [7] and ASTM F36-15 [8, 9].

GRAPHITE THERMAL CONDUCTIVITY CHARACTERIZATION

Graphite is used for spreading heat due to its inherently high conductivity in the planar direction and relatively low conductivity in the through-plane direction. Synthetic graphite thickness ranges from less than 25 μm ($\sim 1,500$ W/m·K) up to 100 μm (~ 600 W/m·K), with in-plane thermal conductivity trending inversely to thickness. Layering thin sheets of high conductivity graphite is a potential way to improve heat spreading capacity at higher thicknesses, though this often leads to inconsistencies in thermal performance as well as challenges in manufacturing. High-performance thick graphite foils prove to have the thermal conductivity benefits of thin synthetic graphite, up to $1,100$ W/m·K in-plane, at single-layer thicknesses similar to that of natural graphite. The through-plane conductivity is comparably ~ 3.5 W/m·K for each grade of graphite.

The in-plane thermal conductivity of this graphite is determined by measuring thermal diffusivity using one of two methods: an Angstrom instrument [10] or a Thermowave Analyzer (Bethel TA-33) [11].

EXPERIMENTAL METHOD: GOOGLE PIXEL 3XL—3DMARK STRESS TEST

An off-the-shelf Google Pixel 3XL (“Pixel”) was purchased and modified to allow for constant power stressing without thermal throttling. UL’s *3DMark—Sling Shot Extreme* was chosen for test-

ing as it is a widely-accepted benchmark used to score the physics (CPU) and graphics (GPU) of high-end smartphones [12]. In order to achieve steady-state test results, the professional version of *3DMark* was purchased and installed on the Pixel to enable infinite looping of the 90-second *Sling Shot Extreme* benchmark test. All testing was conducted in a still air environment with tightly controlled ambient temperature and humidity. Parameters available for measuring include: surface point temperatures via thermocouples, images via IR camera (Fluke, Model Ti55), internal component temperatures (CPU, GPU, etc.) via built-in thermistors, CPU and GPU clock frequencies, and system performance via *Sling Shot Extreme* benchmark score. An initial stress test was run in the out-of-box condition with IR imaging (*Figure 4*). Hot spot locations were identified and chosen for placement of thermocouples via TIMs (*Figure 5*).

The Pixel back cover was removed by means of heating and breaking adhesive. A conformable polymer was placed inside the back cover at seven different locations near the SoC (*Figure 6*) to determine the space available for a thermal solution; the back cover was then replaced to compress the polymer into the existing air gap at each location. The back cover was removed again and thickness at all locations was measured via snap gauge on the compressed polymer. This process was repeated twice more and all thickness measurements per location averaged. Thickness means are detailed in *Table 1*.

| Location | Mean Gap Measurement (mm) |
|----------|---------------------------|
| 1 | 0.900 |
| 2 | 0.625 |
| 3 | 0.520 |
| 4 | 0.520 |
| 5 | 0.440 |
| 6 | 0.450 |
| 7 | 0.640 |

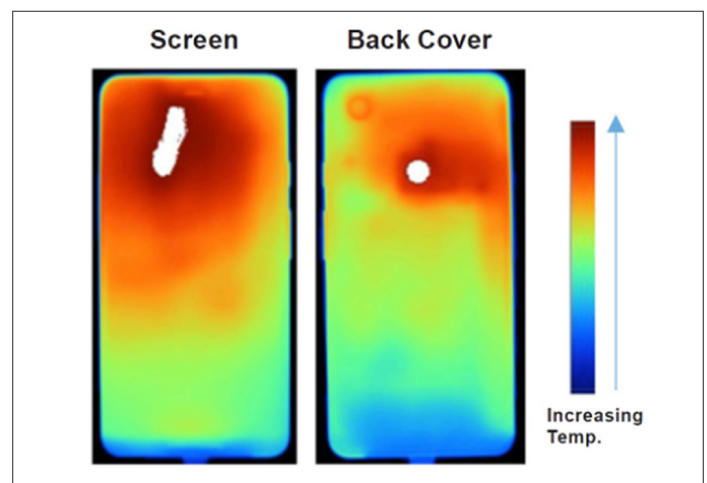


Figure 4: IR images of screen (left) and back cover (right) on the Google Pixel 3XL. A numberless temperature scale is shown to indicate directional trends between color and temperature. Surface hot spots are represented by the white areas.

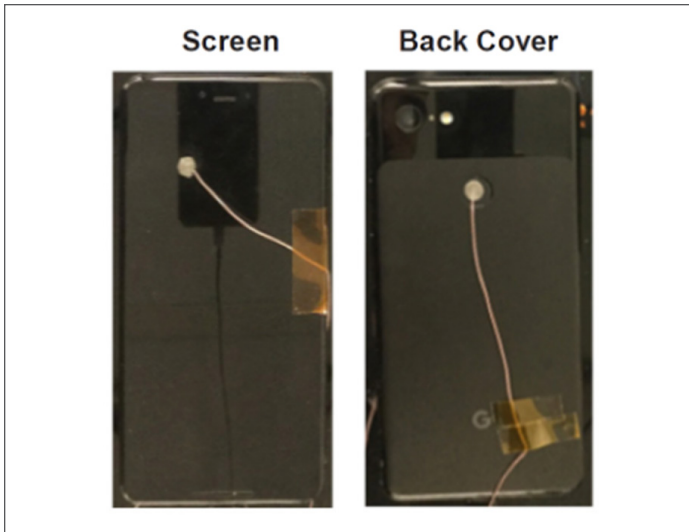


Figure 5: Screen (left) and back cover (right) with thermocouples attached via TIMs on the Google Pixel 3XL. Thermocouples were placed precisely to measure temperatures at the surface hot spot locations.



Figure 6: Google Pixel 3XL with back cover removed. Existing air gap thickness measured by conformable polymer at seven locations shown.

In order to avoid mechanical compression in Locations 5 and 6, a nominal thickness of $350\ \mu\text{m}$ was chosen for all thermal solutions. Physical materials for testing include $110\ \mu\text{m}$ insulation sheets, $110\ \mu\text{m}$ graphite foils, and $5\ \mu\text{m}$ acrylic double-sided tape. Materials and example configurations are illustrated in Figure 7.

The part geometry, shown in Figure 8, was chosen to maximize area with no or minimal disruption to internal components. For simplicity, only configurations with uniform thickness and layers with identical shape and area were considered. Further optimization in layer thicknesses and sizes are possible to achieve form, fit, or functional goals. A cross section schematic through the thickness of the phone is depicted in Figure 9.

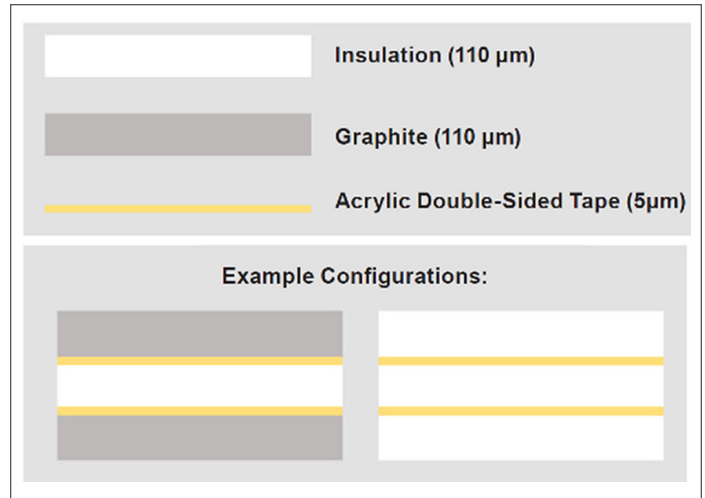


Figure 7: Depiction of physical materials for testing and example configurations of materials layered with adhesive.

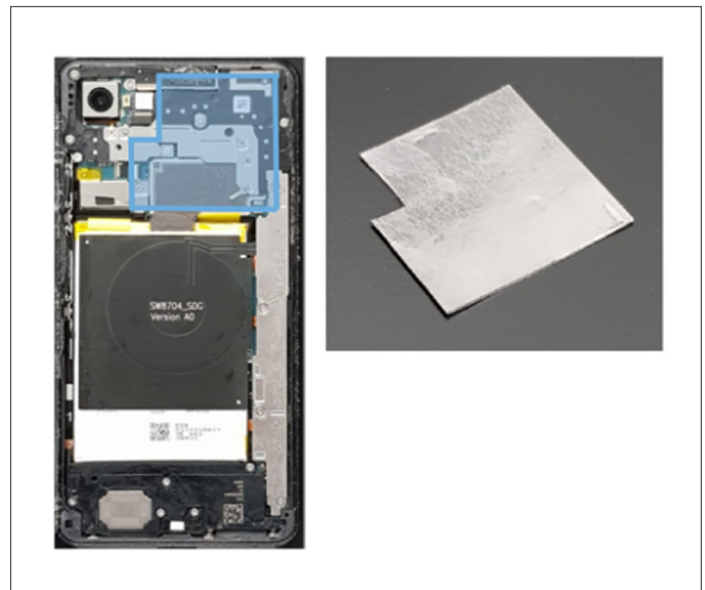


Figure 8 (a, b): 8a (left) shows placement of the part inside the back cover. 8b (right) shows a composite sample cut to fit the designated geometry. Part area measured to be $1825\ \text{mm}^2$.

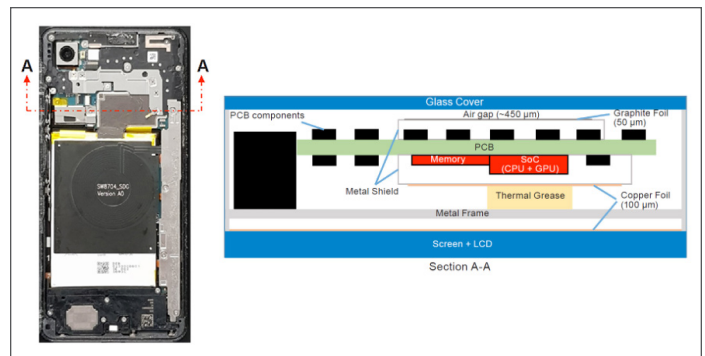


Figure 9 (a, b): 9a (left) denotes the location of cross section A-A in the Pixel. 9b (right) shows a schematic of section A-A through the thickness of the device.

Table 2: Pixel Device Results: Back Cover Touch Temperature Study

| Configuration | Cover Hot Spot Temp. (°C) | | Screen Hot Spot Temp. (°C) | | CPU Max Temp (°C) | | GPU Max Temp. (°C) | | Sling Shot Extreme Benchmark Score | |
|---------------|---------------------------|----------|----------------------------|----------|-------------------|----------|--------------------|----------|------------------------------------|----------|
| | Mean | St. Dev. | Mean | St. Dev. | Mean | St. Dev. | Mean | St. Dev. | Mean | St. Dev. |
| A (control) | 46.7 | 0.21 | 49.7 | 0.25 | 84.8 | 0.17 | 91.9 | 0.35 | 4374.3 | 1.15 |
| B (344 μm) | 45.4 | 0.12 | 50.5 | 0.10 | 86.1 | 0.51 | 93.0 | 0.51 | 4377.7 | 1.15 |
| C (339 μm) | 44.6 | 0.06 | 50.1 | 0.10 | 85.4 | 0.65 | 92.6 | 0.00 | 4375.7 | 1.53 |
| D (347 μm) | 43.5 | 0.15 | 49.9 | 0.26 | 85.6 | 0.17 | 92.5 | 0.35 | 4372.3 | 2.08 |
| E (357 μm) | 44.0 | 0.15 | 49.9 | 0.26 | 85.6 | 0.51 | 92.5 | 0.67 | 4375.0 | 1.00 |

EXPERIMENTAL RESULTS

Back Cover Touch Temperature Study

Device test configurations are titled A, B, C, D, and E with A as the control scenario. The CPU and GPU frequencies were set at 2,169.6 MHz and 675 MHz, respectively. Frequencies were recorded and verified at the end of each test run. Benchmark scores were recorded to show performance consistency across all test runs. Ambient temperatures in the still-air environment were held between 21.6°C and 21.8°C for all testing. All configurations were tested three times to steady-state (>90 minutes) in a randomized experiment.

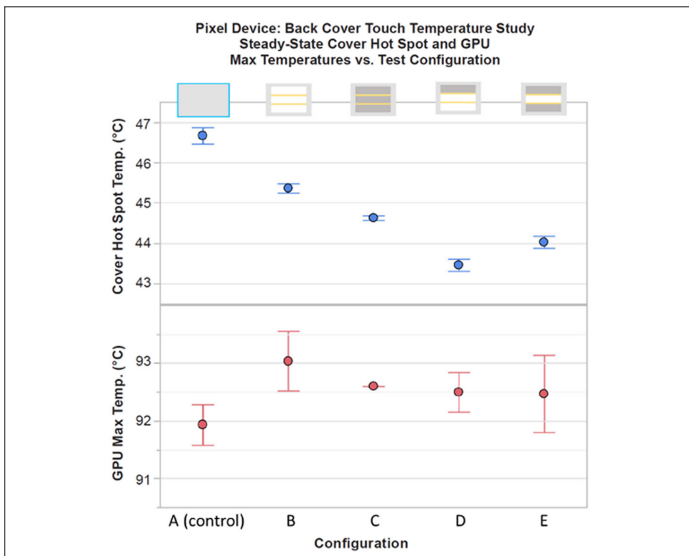


Figure 10: Steady-state graph (means and standard deviations) of back cover hot spot temperature (top) and GPU max temperature (bottom) for all configurations tested in Pixel device, n=3 per configuration.

After each test run, the Pixel was cooled down to idle operating temperature and opened up to setup the next test run. The steady-state back cover hot spot touch temperatures and GPU max temperatures are shown in Figure 10. IR images of the back cover are shown in Figure 11. Depictions, thicknesses, and measured outputs (means and standard deviations) for all tested configurations are detailed in Table 2.

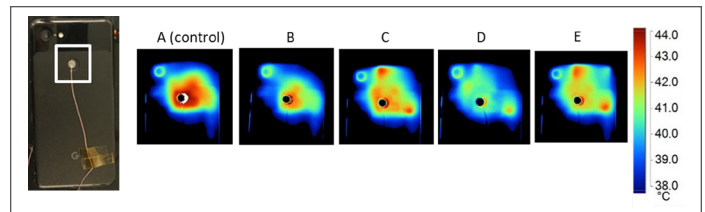


Figure 11: Zoomed in IR images over back cover hot spot for all configurations tested in Pixel device.

All test configurations produced unique back cover touch temperatures with high precision, and all were distinctly lower than the control (Configuration A). Configuration D presented the greatest back cover touch temperature reduction at 3.2°C below the control. Configurations E, C, and B reduced the back cover touch temperature by 2.7°C, 2.1°C, and 1.3°C, respectively. Screen temperatures increased from the control by <1°C for all configurations tested and <0.5°C for composite configurations. CPU and GPU temperatures increased from the control by <1.5°C for all configurations tested and <1°C for composite configurations.

System Performance and Safe Touch Temperature Study

A continuation study was created to determine the allowable system performance increase when enabled by insulation-graphite composites; Configuration D was selected for this study. Out-of-box throttling conditions were restored to the Pixel and all thermal solutions were removed, leaving air only. The back cover touch temperature was measured during steady-state power throttling and recorded for three test runs. Configuration D was installed and frequencies were set to match the steady-state cover temperature from the throttled control runs. The appropriate frequencies for testing were determined to be 1,996.8 MHz and 596 MHz for the CPU and GPU, respectively. Frequencies, cover hot spot temperature, benchmark score, and frames per second were measured and compared between the two test scenarios. A smoothed plot of benchmark score, CPU frequency, and GPU frequency vs. run time for all six test runs is displayed in Figure 12. Mean steady-state cover temperature, benchmark score, and frames per second are shown in Figure 13. Details are summarized in Table 3.

Table 3: Pixel Device Results: System Performance and Safe Touch Temperature Study

| Test Scenario | Cover Hot Spot Temp. (°C) | | Sling Shot Extreme Benchmark Score | | Frames per Second | |
|-------------------------------------|---------------------------|----------|------------------------------------|----------|-------------------|----------|
| | Mean | St. Dev. | Mean | St. Dev. | Mean | St. Dev. |
| Air (out-of-box throttling) | 38.7 | 0.15 | 3401.0 | 8.19 | 19.5 | 0.06 |
| Configuration D (fixed frequencies) | 38.7 | 0.15 | 3822.7 | 3.06 | 21.3 | 0.00 |

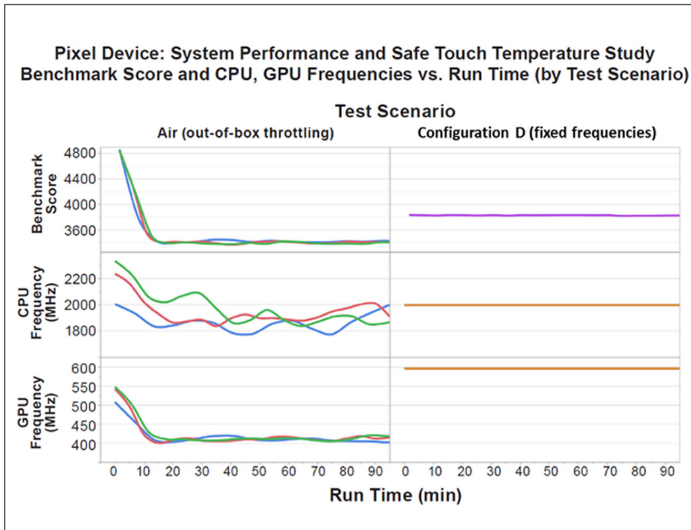


Figure 12: Transient graph (smoothed) of benchmark score (top), CPU frequency (middle), and GPU frequency (bottom) for air only, out-of-box throttling (left) and Configuration D, fixed frequencies (right) in Pixel device, n = 3 per test.

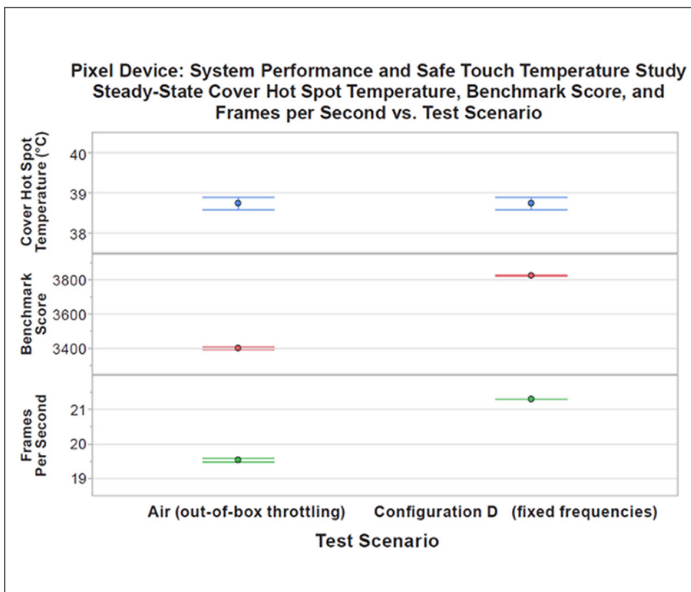


Figure 13: Steady-state graph (means and standard deviations) of back cover hot spot temperature (top), Sling Shot Extreme benchmark score (middle), and Frames per Second (bottom) for air only, out-of-box throttling and Configuration D, fixed frequencies in Pixel device, n=3 per configuration.

The mean steady-state cover touch temperature achieved during out-of-box throttling is 38.7°C in the controlled test environment at 21.7°C; this temperature is related to UL 62368-1 mobile electronics touch (skin) temperatures at prolonged durations. In this scenario, the mean steady-state benchmark score and fFrames per sSecond are 3,401 and 19.5, respectively. When Configuration D is placed inside the back cover, the benchmark score is increased to 3,823 and frames per second increased to 21.3, marking a ~12% increase in system performance, while maintaining the safe surface temperature limit set for the out-of-box throttling condition.

SUMMARY/CONCLUSION

Graphite foils with ultra-high spreading capacity and insulation sheets with ultra-low thermal conductivity were combined in a modified Google Pixel 3XL to reduce surface touch (skin) temperatures, while minimally impacting the device junction temperature, compared to solutions of air, insulation alone, and graphite alone. One insulation-graphite composite configuration was further tested in comparison to an out-of-box condition, and was found to improve system performance in a UL benchmark test by ~12% while maintaining the out-of-box cover surface temperature limits.

The results demonstrated by insulation-graphite composites in Pixel device testing can be explained by the exceptional thermal properties exhibited by these two materials. Through-plane thermal conductivity for the insulation was measured and calculated using a heat flow method on a TA-FOX 50, and a thickness method on an Instron-5565. In-plane thermal conductivity for high-performance thick graphite was measured and calculated using a thermal diffusivity method on a Bethel TA-33.

High-performance insulation-graphite composites may have vast utility in the high-powered, thin architectures of mobile electronics. It is important to note that each mobile electronic system may exhibit unique thermal challenges given system power, available space, and/ or other constraints. For this reason, the optimal design configuration (area, thickness, orientation) should be determined by virtue of device-specific simulation and testing. The case study presented in this paper demonstrates the enhancement of thermal management in mobile electronics; two leading-edge materials, when combined, yield a thermal solution with performance greater than the sum of its parts.

REFERENCES

1. UL, UL. "62368-1: 2017 Audio/video, information and communication technology equipment - Part 1: Safety requirements." (2017).
2. Wagner, Guy, and William Maltz. "Thermal management challenges in the passive cooling of handheld devices." 19th International Workshop on Thermal Investigations of ICs and Systems (THERMINIC). IEEE, 2013.
3. Wagner, Guy R. "A study of the maximum theoretical power dissipation of tablets under natural convection conditions." 20th International Workshop on Thermal Investigations of ICs and Systems. IEEE, 2014.
4. Luo, Zhaoxia, et al. "System thermal analysis for mobile phone." Applied Thermal Engineering 28.14-15 (2008): 1889-1895.
5. Bi, C., G. H. Tang, and W. Q. Tao. "Prediction of the gaseous thermal conductivity in aerogels with non-uniform pore-size distribution." Journal of Non-Crystalline Solids 358.23 (2012): 3124-3128.
6. Kannuliuk, W. G., and E. H. Carman. "The temperature dependence of the thermal conductivity of air." Australian Journal of Chemistry 4.3 (1951): 305-314.
7. ASTM C518 - 17 Standard Test Method for Steady-State Thermal Transmission Properties by Means of the Heat Flow Meter Apparatus
8. ASTM F36 - 15 Standard Test Method for Compressibility and Recovery of Gasket Materials
9. LaserComp, Inc.. "Tests of thin samples stacked (using FOX50 instrument)" Application Note AN-TSS © 2008 (October 23).
10. Wagoner, G., Skokova, K.A. and Levan, C.D., "Angstrom's Method for Thermal Property Measurements of Carbon Fibers and Composites", The American Carbon Society, CARBON Conference, 1999.
11. Beyerle, R., Smalc, M., Kantharaj, R., Taylor, J., Norley, J., "Thermal Diffusivity Characterization of Thick Graphite Foils", 35th Semi-Therm Symposium, 2019.
12. 3DMARK® Technical Guide, Underwriters Laboratories, Fremont, CA, 2020.

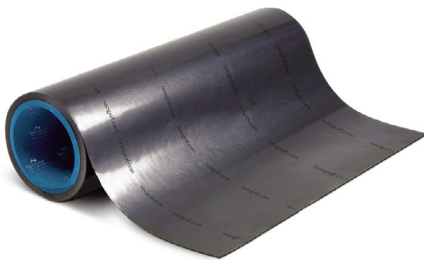




Are you looking for a thinner, more effective material to achieve better heat spreading?



NeoNxGen™ high performance graphite is the best thermal management solution for advanced electronics



NeoNxGen™ Thermal Management Solutions eliminate the cost, complexity, and reliability concerns of multi-layered synthetic graphite by providing:

- ▶ A simple single layer graphite (≥ 70 microns thick)
- ▶ Heat spreading to eliminate hot spots ($>1,000$ W/mK thermal conductivity)
- ▶ Shield temperature sensitive components

Increase the thermal performance, not the layers!

Please call **+1 216-529-3754**
or go to neograf.com/neonxgen for more information on
NeoNxGen™ Thermal Management Solutions

Duocel® Metal Foam Heat Exchangers

Burhan Ozmat, Metodi Zlatinov, and Denver Schaffarzick

*ERG, Materials and Aerospace Corporation
964 Stanford Avenue, Oakland, CA 94608*

As power-component technology advances and smaller packaging is required, thermal-management issues threaten to limit the performance of devices. As power dissipation rises, the inability to cool them may force designers to de-rate the devices' performance by reducing current or switching speed and/or employing higher-voltage devices that are less efficient and more expensive. These compromises in design may increase the size, weight, or cost of the application.

A proven approach is to transfer higher heat fluxes to ambient by improving the performance of the heat sink and reducing or elim-

inating soft thermal interfaces. One technology capable of accomplishing these goals employs a class of materials known as metal foams. One specific type of high-performance metal foam is Duocel®, a solid ligament, open celled metal foam manufactured by ERG Aerospace. The material was developed more than 50 years ago for structural applications, and is being applied effectively to thermal-management problems in electronic systems.

Unlike conventional finned heatsinks, Duocel®-based heatsinks consist of blocks that are either brazed or soldered to a substrate material. When compared with finned heat sinks, these heatsinks



Burhan Ozmat

Burhan Ozmat received his Ph.D. degree from Massachusetts Institute of Technology as DOE and NATO Science fellow, MSc and BSc degrees from Technical University of Istanbul. Currently he works at the OZER Advanced Technologies that he established, as an R&D consultant. Previously he is engaged in designing, modeling, prototyping, and testing of metallic foam based advanced thermal technology products. He worked at GE Corporate Research center at Niskayuna NY, Harris Power R&D center in Albany NY, Texas Instruments Defense Electronics Center Group in Dallas TX, and IBM Advanced Packaging Laboratory at East Fishkill, NY. His main field is the Mechanical and Thermal behavior of engineering materials where he has several patents and publications.



Metodi Zlatinov

Metodi Zlatinov earned his M.S. in Aeronautics and Astronautics from Massachusetts Institute of Technology, and a B.S.E. in Mechanical Engineering from Princeton University. Currently he is the technical lead for ERG Aerospace's in-house R&D efforts, with a specific focus on heat transfer applications. Prior to joining ERG, Mr. Zlatinov advanced the state of the art in CFD-based optimization while developing cooling technologies for gas turbines at GE Aviation, and later led the fluid design and hydraulic testing efforts for novel hydroelectric turbines at Natel Energy.



Denver Schaffarzick | ds@ergaerospace.com

Denver Schaffarzick earned his B.S. in Mechanical Engineering at Cal Poly, San Luis Obispo, and is a member of their Industry Advisory Board. He is currently the Director of Engineering at ERG Aerospace Corporation. Denver thrives on finding new solutions to solve old problems focusing on heat transfer application engineering design and manufacturing "know how". Denver has participated in specialty parts for Pratt Whitney Geared Turbo Fan Engine, many aerospace components, and thermal capacitors for the European Space Agency ExoMars. Prior to joining ERG, Denver worked at KARCO Engineering conducting vehicle research and specializing in full scale dynamic crash testing.

offer improved thermal performance, smaller size, lighter weight, lower cost versus performance among other advantages.

Duocel® is a proven, cost-effective and ultra-high-performance thermal management material that can be integrated with electronic devices and modules. It is also compatible with traditional coolants used in heat exchanger for electronic devices, making it an ideal candidate for cold plates and liquid cooled applications.

STRUCTURE OF DUOCEL®

There are several types of metal foams. This paper focuses on solid ligament, open celled metal foams, known as Duocel® manufactured by ERG Aerospace. Solid ligament, open cell metal foams offer significant structural and thermal properties compared to 3D printed or sintered foam structures, which often have weak or hollow ligaments. In the as-fabricated state, the isotropic structure consists of randomly oriented polygon shaped cells that can be approximated as dodecahedron, *Figure 1* [2,3,4]. Notice that the cross sections of roughly 2 mm long solid ligaments are mostly triangular. The geometry of the cell structure and the high purity and ductility of its solid ligament metal produce the most desirable characteristics for heat exchanger (HX) applications. The physical dimensions of its structure, as shown below, does not allow boundary layers to grow and introduce enhanced mixing through eddies and turbulence. These features result in a high local film coefficient.

Open cell, solid ligament metal foams are commonly produced in aluminum and copper, and have controllable pore size (5, 10, 20 and 40 pores per inch (PPI)) and customizable relative density of 4-13% (a.k.a. volume fraction). Due to the solid ligament's high ductility, they can be compressed to 50% relative density through mechanical compression, further enhancing the thermal performance per unit volume. The important parameters of Duocel® are thermal conductivity, heat transfer surface area, high mechanical ductility and compliance.

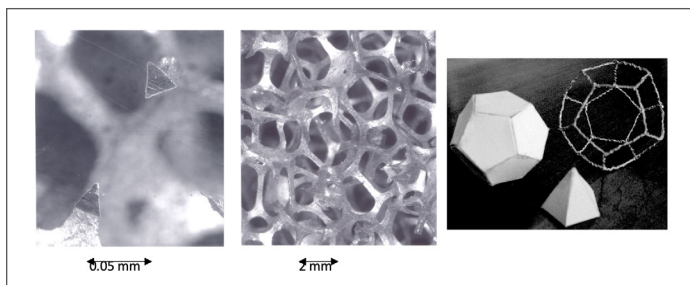


Figure 1: 40 pores per inch (PPI) 6101 Al based metal foam consisting of nodes and ligaments forming a space filling network of dodecahedrons with 12 pentagon shaped facets.

THERMAL CONDUCTIVITY

The foam manufacturing process preserves the high purity of the material in the structure. The thermal conductivity of 6101 Al and C10100 Cu, most common base materials, are about 215 W/m-K and 390 W/m-K, respectively. The effective bulk ther-

mal conductivity, however, depends on the porosity of the foam RMF's effective bulk conductivity (k_c) and may be estimated by *Equation (1)* [2].

$$k_c = \lambda k_b \rho_e \quad (1)$$

Where:

λ , the proportionality constant $\lambda = 0.346$

k_b , the thermal conductivity of the base material

ρ_e , the relative density (metal volume fraction) of as-foamed structure

The effective bulk conductivity of an 8% relative density 6101 Al Duocel® is about 6 W/m-K. Due to their high ductility, it can undergo significant inelastic and elastic buckling deformations without failure of the solid ligaments, resulting in an increase in the relative density of the foam structure up to 50%. Since the thermal conductivity is a vector quantity, its value will be a function of not just the amount of compression (as it is for the effective surface area), but also of the direction of compression. The effective thermal conductivity of 6101 Al based foams biaxially increases to ~ 40 W/m-K, when unidirectionally compressed in X direction to 50% relative density in the (YZ) plane where ligaments are aligned in Y and Z directions. The amount and direction of compression, as well as the initial pore size and relative density, are the variables that allow the properties of Duocel® to be tailored to a given application, creating a heat sink with performance optimized for the application.

SURFACE AREA DENSITY

One of the most important features of the metal foams is their extremely high and scalable surface area density (ρ_s) compare to those of brazed or extruded fins and fin pins. ρ_s is directly related to the extended surface area for improved convective heat transfer. The ρ_s of Duocel® was characterized using experimental measurements, by multipoint Brunauer, Emmett, and Teller (BET) method by adsorption of krypton gas at 77.4 K, and the modelling studies by authors.

The results of these studies showed that ρ_s of 40 PPI metal foam at as fabricated 6% and compressed 50% state are about 15.5 cm²/cm³ (40 in²/in³) and 138 cm²/cm³ (350 in²/in³), respectively [2,3].

CONVECTIVE FILM COEFFICIENTS

The mostly triangular cross section and only a couple of millimeter long ligament geometry of Duocel® offers significant advantages in convective cooling. It scales down the thickness of boundary layers, generates vortices, and induces turbulence. In two-phase flow applications, it also delays or eliminates the transition from nucleate boiling to film boiling. The net outcome is enhanced heat transfer due to high local film coefficients.

THERMAL INTERFACES

A metal foam based compact HX can be integrated to the sources of heat generation via solder bonding. Integration eliminates the highly resistive thermal interfaces of soft materials such as ther-

mal pads, pastes, or thermal epoxies commonly used to couple discrete devices, hybrid multi-chip modules (HMCM) of photonic and electronic devices. Duocel® may be brazed to low expansion skin layers and function as a constraining double-sided core heat exchanger (HX) for printed wiring boards (PWBs).

The metal foam structure has a very high effective compliance, [2] that allows metallurgical bonding to the foam by soldering or brazing to low CTE materials (metalized ceramic plates, low expansion composites, Mo, and CuMoCu, among others). Since the CTE mismatch related thermal stresses and deformations are limited, the reliability of the integral heat exchanger and the thermal base is not compromised, as verified by several hundreds of thermal cycles [5].

FABRICATION OF METAL FOAM HEAT EXCHANGERS

Method of manufacturing of Duocel® based heat exchangers depends on the material and the design. Aluminum RMF based HXs can be fabricated with vacuum or dip brazing. Fully enclosed HX/cold plate (CP) configurations require vacuum brazing using solid braze preforms. HXs with exposed metal foam can be fabricated by either dip brazing or vacuum brazing. The open cell structure of RMF allows cleaning of any residual salt left over from the dip brazing bath. The advantage of vacuum brazing however becomes

apparent for manufacturing in larger quantities. Use of a vacuum furnace may accommodate hundreds of units in a single batch operation at a lower cost per unit.

The fabrication of Cu foam-based heat exchangers where Cu foam is bonded to a Cu plate of enclosed housing are fabricated with inert-atmosphere, high-temperature brazing or vacuum brazing furnaces with suitable Cu-Ag solid braze preforms. Solder pastes may be used to fabricate CPs in inert-atmosphere furnaces where the structure is exposed. Figure 2 shows a variety of 6101 aluminum foam-based articles made by vacuum brazing [6].

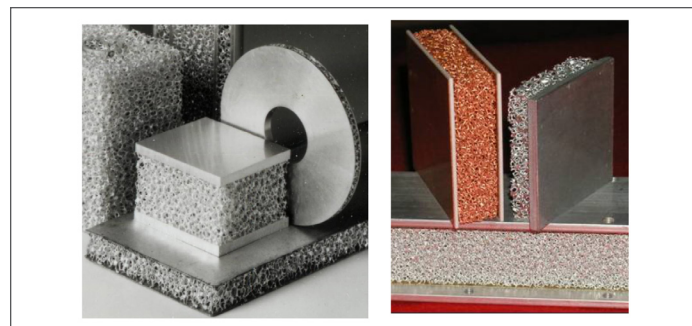



Figure 2: Precursors of Al and Cu Duocel® vacuum brazed HXs and CPs



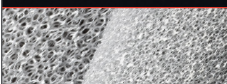
Duocel® Metal Foam Heat Exchangers

- High Thermal Conductivity
- High Surface Area to Volume Ratio
- Air and Liquid Cooled Options
- Ideal for Phase Change HX's

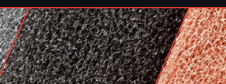
COLD PLATE COMPARISON CHART

| Company | Hx Type | Size (in ³) | Weight (lb) | R _{th} (°C/W/in ²) |
|--------------|------------|-------------------------|-------------|---|
| ERG | Duocel® Al | 1.5 | 0.05 | 0.04 |
| Competitor A | Al Pin-Fin | 41.0 | 3.50 | 0.28 |
| Competitor B | Al Pin-Fin | 103.0 | 2.70 | 0.39 |

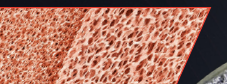
Duocel® allows for compact, high performance solutions to transform your electronics



ALUMINUM




CARBON



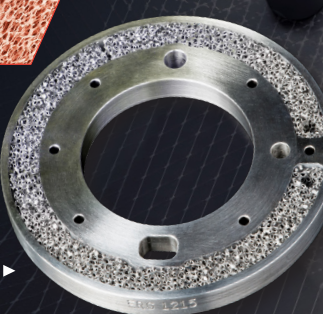
COPPER

Talk with our design team to make the impossible, possible.

www.ergaerospace.com | sales@ergaerospace.com



Liquid cooled heat exchanger for an electronics system ▶



ANALYTICAL STUDY OF THERMAL PERFORMANCE

The major factors scaling the thermal performance of Duocel® HX are:

- Thermal conductivity of the base material (Al, Cu, Ag, or others).
- Pore size measured as PPI, the linear density of pores per inch (5-40 ppi).
- Relative density (5% to ~50%)
- Physical thickness (impacts fin efficiency similar to fin length)
- Thermo-physical properties of the coolant

Improved heat transfer performance due to RMF can be analyzed in a similar fashion to conventional HX and can be quantified in terms of an equivalent flat plate effective heat transfer coefficient ($Heff$) based on the footprint area of the cooling unit. *Figure 3* [2] illustrates the trends and magnitudes of $Heff$ for forced convection using distilled water as the coolant with an estimated local film coefficient of $1 \text{ W/cm}^2\text{-}^\circ\text{C}$ (determined empirically). Effective film coefficient is a strong function of relative density, while asymptotically approaching a saturation value with increased thickness in a manner analogous to fin efficiency. This parametric analysis assumed idealized 1D conduction, but more complex scenarios can readily be tackled using conjugate heat transfer CFD modeling and appropriately defined porous media properties.

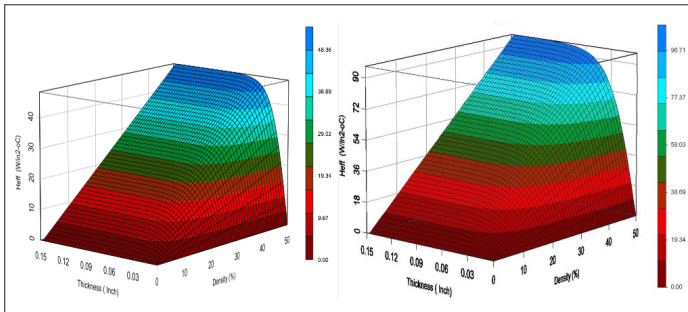


Figure 3: Effective Heat Transfer Coefficient of 40 PPI 6061 Al (left) and Cu (right) Duocel® HXs with DI water as the coolant with an estimated local film coefficient of $1 \text{ W/cm}^2\text{-}^\circ\text{C}$ (determined empirically). The thickness range for both the Al and Cu foams is 0-38 mm.

EXPERIMENTAL STUDY OF THERMAL PERFORMANCE

To demonstrate the cooling capability of Duocel®, a test module was fabricated by inert atmosphere brazing a $1.00'' \times 1.00'' \times 0.250''$ block of Duocel® copper foam to the center of a $2.00'' \times 2.00'' \times 0.125''$ thick Cu plate. A Plexiglas housing of the same cavity depth was fabricated out of a $0.25''$ thick Plexiglas sheet and screwed to the Cu plate with cork gasket. A $1.00'' \times 1.00''$ resistor was eutectic Sn/Pb soldered on the center of the Cu plate in inert gas environment. The cold plate test unit is depicted in *Figures 4* and *5*.

The flow rate and the inlet temperature of the inlet DI water were kept constant using a recirculating chiller. The heater power, volume flow rate, inlet, and exit temperature of the coolant were monitored via multimeter current and voltage measurements, flow meter, and thermocouples, respectively. The surface tem-

perature of the cold plate was estimated by the temperature measurements with thermocouples on the resistor. This experimental setup is shown in *Figure 6*.

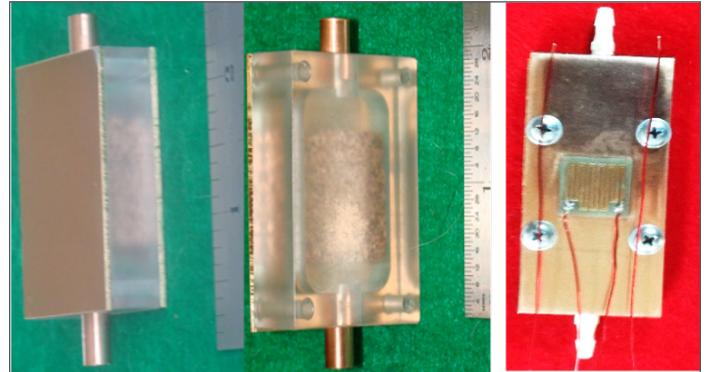


Figure 4: Double and single sided see through functional cold plates (left), top view of the single sided test unit (right).

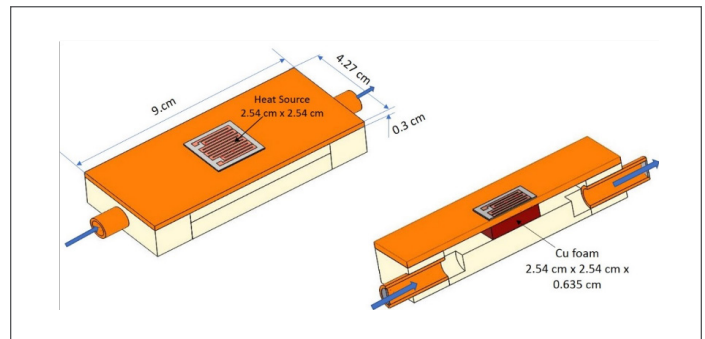


Figure 5: Cu Duocel® Cold Plate test unit

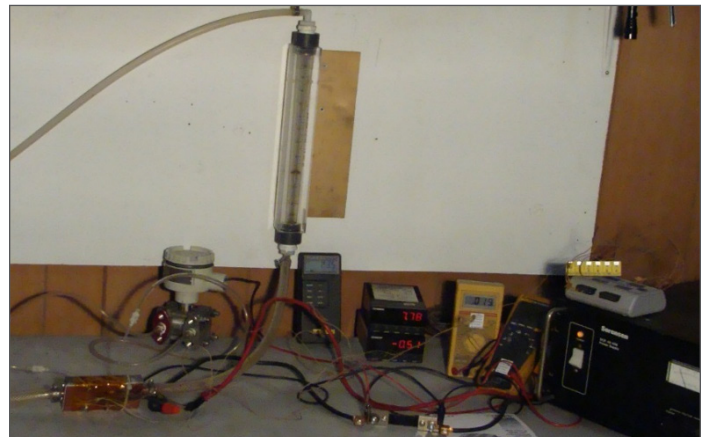


Figure 6: Unit under flow and thermal resistance tests

The results are presented in *Figure (7)* in terms of thermal resistance, which is commonly defined by *Equation (2)*:

$$R_{th} = \frac{\Delta T}{Q} \quad (2)$$

$$\Delta T = T_{Max} - [T_{in} + \frac{1}{2} Q / (\dot{m} C_p)] \quad (3)$$

where

Q: Power dissipated by the heater/device (W)

ΔT : Temperature difference between the maximum surface temperature of the CP and the average temperature of the coolant, as calculated by Equation (3)

C_p : Heat capacity of coolant (J/kg-°C)

(\dot{m}): Mass flow rate of coolant (kg/sec)

The experimental results in Figure (7) show excellent agreement with the CFD analysis, validating the modeling approach. The subsequent case study will give more context for the measured and predicted performance numbers.

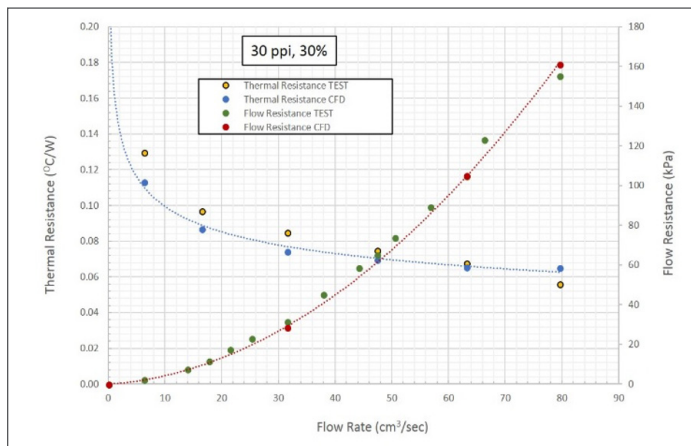


Figure 7: Flow and the thermal resistances of Cu foam based Cold plates [6].

CASE STUDY ON HIGH POWER ELECTRONICS DEVICE COLD PLATE

In the early stages of design, the feasibility of a given cold plate technology for a high-power electronics device may be assessed by its thermal resistance (R_{th}). Consider the application of cooling a 1" x 1" device that dissipates 1 kW of heat. Assume the max allowable temperature of $T_{Max}=60^{\circ}C$, and the available cooling flow is DI water ($\rho_w=1,000 \text{ kg/m}^3$, $CP=4,184 \text{ J/kg}\cdot^{\circ}C$) at a volume flow rate of $\dot{V}=1.0 \text{ GPM}$ ($6.3\cdot 10^{-5} \text{ m}^3/\text{sec}$) and $T_{in}=21^{\circ}C$. Using Equations (2) and (3), the required thermal resistance is $0.037 \text{ }^{\circ}C/W$.

High performance micro channel type Cu cold plates are only able to deliver $0.05^{\circ}C/W$ under these conditions, which would be insufficient for the present application. Meanwhile a Duocel® based cold plate can be tailored to achieve the goal with a healthy margin using a 40 PPI, 45% dense copper foam cold plate, as demonstrated by the CFD results in Figure 8.

SUMMARY AND DISCUSSIONS

Studies show that open cell, solid ligament Duocel® based CP and HXs offer high thermal performance due to their extremely high specific surface area, local film coefficients, and thermal conductivity particularly for lower volume and weight applications. The structure can be customized to meet a wide range of thermal requirements making them a versatile solution.

Metal foams demonstrate compatibility with a wide range of liquids and gaseous coolants, which makes the technology advantageously suitable for a wide range of commercial and military applications. The structural and thermal characteristics of RMF foams also offers similar advantages in passive phase change and two-phase flow applications.

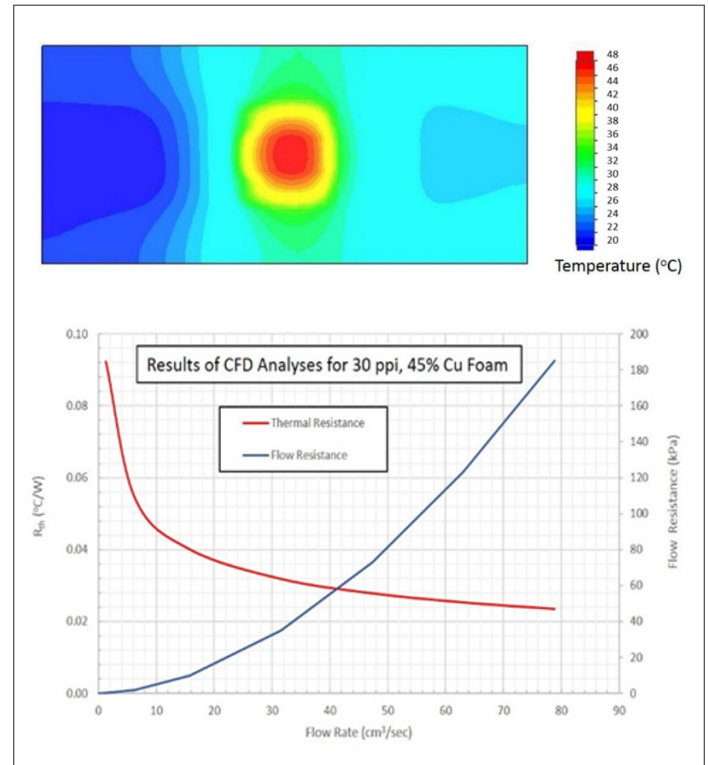


Figure 8: CFD results for 30 PPI and 45% Cu foam at 1 GPM flow rate, showing the surface temperature of the cold plate (top) and corresponding thermal and flow resistances (bottom)

ACKNOWLEDGEMENTS

Authors would like to take this opportunity to express their gratitude to Mitchell Hall, the CEO of ERG Aerospace, for his support, encouragement, and directions in the research and the publication of this work.

REFERENCES

1. Ashby, M. F. et al. "Metal Foams - A Design Guide", Butterworth Heinemann, pp. 6-20, 2000.
2. B. Ozmat et al., "Thermal Applications of Open Cell Metal Foams" Materials and Manufacturing Processes, Special Edition, Vol.19, No. 5, pp. 839-862, 2004
3. Brunauer, Emmet, Teller, Journal of the American Chemical Society, Volume 60, 1938, p 309.
4. Sorgo M., "Thermal Interface Materials," Electronics Cooling, Vol. 2, No. 3, pp. 12 -16., Sept. 1996.
5. Final Program Report, COMNAVSEASYS COM contract N00024-94-NR58001.
6. The metal foam used in the fabrication of these cold plates is marketed under the trade name Duocel®, ergaerospace.com

From the Creators of *Electronics Cooling*

INTRODUCING

LECTRIX

THERE'S ONLY ONE SPOTLIGHT

ARE YOU IN IT?

Positioning Ambitious B2B Electronics Companies
for Aggressive Growth

www.lectrixgroup.com

PHILADELPHIA, PA | HONG KONG


2020 Company Products & Services Directory

In this section, we provide a quick guide to some of the top suppliers in each EMC category—in heat sinks, thermal testing, design services, and more. To find a product that meets your needs for applications, frequencies, standards requirements, etc., please search these individual supplier websites for the latest information and availability. If you have trouble finding a particular product or solution, email info@lectrixgroup.com for further supplier contacts.

| COMPANY | | CONTACT INFORMATION | PRODUCTS & SERVICES | |
|--------------------------|---|--|---|---|
| MEDIA PROVIDER SPOTLIGHT |  | LECTRIX 1000 Germantown Pike Plymouth Meeting, PA 19462 t: (484) 688-0300 w: www.lectrixgroup.com | - Strategy Firm - Full-Service Marketing - Publishing | - Events and Webinars - Custom Solutions - Training and Consultation |
| |  | Thermal Live™ 2020 Online Event October 20 th - 21 st 2020 t: (484) 688-0300 e: info@electronics-cooling.com w: www.thermal.live | - Training Seminars & Workshops | |
| COMPANY | | WEBSITE | PRODUCTS & SERVICES | |
| A |  | www.alphanovatech.com | - Coolers - Heat Sinks - Thermal Design Services | - Thermal Tapes - Thermal Testing |
| | Ansys, Inc. | www.ansys.com | - Software | |
| B | Boyd Corporation | www.boydcorp.com | - Blowers/Fan Accessories - Blowers - Chillers - Cold Plates - Fans - Gap Pads & Fillers | - Heat Pipes - Heat Sinks - Interface Materials - Liquid Cooling - Thermal Design Services - Thermal Testing |
| C | Cadence | www.cadence.com/en_US/home.html | - Software | |
| | CEJN USA | www.cejn.us | - Couplings | |
| | Celsia Inc. | www.celsiainc.com | - Heat Pipes - Heat Sinks - Heat Spreaders | - Thermal Design Services - Vapor Chambers |

| COMPANY | | WEBSITE | PRODUCTS & SERVICES | |
|---------|---|--|---|--|
| C | CP Cases | www.cpcasesusa.com | - Air-Conditioned Transit Cases | |
| |  | www.cpcworldwide.com | - Connectors | |
| | COFAN U.S.A. | www.cofan-usa.com | - Blowers - Coolers - Fans | - Heat Sinks - Heat Pipes - TIM's |
| D |  | www.deltabreez.com | - Blowers - Fan Trays | - Fans - Heat Exchangers |
| E | ElectronicsCooling® | www.electronics-cooling.com | - Media | - Training Seminars & Workshops |
| |  | www.ergaerospace.com | - Heat Exchangers | - Thermal Management Materials |
| F | Fujipoly® America Corp. | www.fujipoly.com | - Connectors - Gap Pads & Fillers | - Interface Materials - Thermal Design Services |
| H | Heilind Electronics, Inc. | www.heilind.com | - Liquid Cold Plates | |
| | Henkel | www.henkel.com | - Gap Pads & Fillers - Interface Materials - Phase Change Materials | - Substrates - Thermal Tapes |
| | High Tech Institute | www.hightechinstitute.nl | - Training Seminars and Workshops | |
| I | Indium | www.indium.com | - Interface materials | - Thin-Film Materials |
| | Institution of MECHANICAL ENGINEERS | www.imeche.org | - Training Seminars & Workshops | |
| |  | www.ims-resistors.com | - Heat Spreaders | - Thermal Management Devices |
| J | JARO Thermal | www.jarothermal.com | - Blowers | - Fans |

| COMPANY | | WEBSITE | PRODUCTS & SERVICES | |
|---------|---|--|---|-----------------------------|
| L | Laird Technologies | www.lairdtech.com | - Phase Change Materials | - Thermoelectric Coolers |
| M |  | www.malico.com | - Cold Plates - Heat Sinks | - Liquid Cooling |
| |  | www.masterbond.com | - Interface Materials | |
| | Materion | www.materion.com | - Thermal Management Materials | - Phase Change Materials |
| |  | www.mentor.com | - Software - Thermal Design Services | - Thermal Testing |
| | Mersen | www.mersen.us | - Heat Pipes - Heat Sinks | - Liquid Cold Plates |
| | Momentive | www.momentive.com | - Interface Materials | - Silicone Adhesives |
| N | Nanoramic | www.nanoramic.com | - Interface Materials | |
| |  | www.neograf.com | - Expandable Graphite - Flexible Graphite | - Heat Spreaders - TIM's |
| O | ORION Fans | www.orionfans.com | - Blowers/Fan Accessories - Fan Controllers - Fan Filters | - Fan Trays - Fans |
| P | Panasonic | na.industrial.panasonic.com | - Interface Materials | |
| | PCBWay | www.PCBWay.com | - Prototyping, PCB Design to Assembly | |

| COMPANY | | WEBSITE | PRODUCTS & SERVICES | |
|---------|---|--|---|---|
| P | Polymer Science Inc. | www.polymerscience.com | - Gap Fillers - Heat Spreaders | - Interface Materials - Phase Change Materials |
| | Polyonics | www.polyonics.com | - Advanced Coating Technologies | |
| R | Rittal | www.rittal.us | - Electrical Enclosures - Liquid Cooling | - Chillers and Filter Fans |
| | Rosenberg USA, Inc. | www.rosenbergusa.com | - Blowers - Fan Filters | - Fans |
| S |  | www.semi-therm.org | - Training Seminars & Workshops | |
| | Shin-Etsu MicroSi | www.microsi.com | - Interface Materials | |
| | Shiu Li Technology Co., LTD | www.shiuli.com.tw | - Interface Materials | - Thermal Tapes |
| | Siemens | www.siemens.com/mdx | - Education Courses/Seminars | - Software |
| | Staubli Corporation | www.staubli.com | - Connectors - Couplings | - Software |
| T | T-global Technology Co. Ltd | www.tglobal.com.tw | - Gap Pads & Fillers - Interface Materials | - Thermal Tapes |
| | Thermal Engineering Associates Inc. | www.thermengr.com | - Thermal Test Chips | |
| | TECA ThermoElectric Cooling America Corporation | www.thermoelectric.com | - Air Conditioners - Cold Plates | - Coolers - Thermoelectric Coolers |
| W | Wavelength | www.teamwavelength.com | - Temperature Controllers | |

Index of ADVERTISERS



Alpha Novatech, Inc.
473 Sapena Ct. #12,
Santa Clara, CA 95054

t: +1 (408) 567-8082
e: sales@alphanovatech.com
w: www.alphanovatech.com
page: Back Cover



CPC Worldwide
1001 Westgate Drive
St. Paul, MN 55114

t: (651) 645-0091
w: www.cpcworldwide.com
page: 14



Delta Electronics Ltd.
46101 Fremont Blvd.
Fremont, CA 94538 U.S.A.

t: (866) 407-4278
e: dcfansales.us@deltaww.com
w: www.delta-fan.com
page: 3



ERG Materials & Aerospace
964 Stanford Avenue
Oakland, CA 94608

t: (510) 658-9785
e: sales@ergaerospace.com
w: www.ergaerospace.com
page: 44



International Manufacturing Services, Inc.
50 Schoolhouse Lane
Portsmouth, RI 02871

t: (401) 683-9700
e: customerservice@ims-resistors.com
w: www.ims-resistors.com
page: 31



LECTRIX
1000 Germantown Pike,
Plymouth Meeting, PA 19462

t: (484) 688-0300
e: info@lectrixgroup.com
w: www.lectrixgroup.com
page: 47



Malico Inc.
No. 5, Ming Lung Road,
Yangmei 32663, Taiwan

t: 886-3-4728155
e: inquiry@malico.com
w: www.malico.com
page: 33



Master Bond, Inc
154 Hobart Street
Hackensack, NJ 07601

t: +1 (201) 343-8983
e: main@masterbond.com
w: www.masterbond.com
page: 21



Mentor Graphics
8005 SW Boeckman Road
Wilsonville, OR 97070

t: (800) 592-2210
e: sales_info@mentor.com
w: www.mentor.com
page: 27



Neograf Solutions, LLC
11709 Madison Avenue
Lakewood, Ohio USA 44107

t: (216)529-3754
w: www.neograf.com
page: 41



SEMI-THERM 37
Double Tree by Hilton
San Jone, CA USA
March 22 – 26, 2021

t: +1 (408) 840-2354
e: mvalle@infinera.com
w: www.semi-therm.org
page: 15



THERMAL LIVE 2020
Online Event
October 20-21, 2020

t: (484) 688-0300
e: info@electronics-cooling.com
w: www.thermal.live
page: Inside Front Cover